Photometric Properties of Galaxy Populations in Group and Cluster Environments

by

I-hui Li

A thesis submitted in conformity with the requirements
for the degree of Doctor of Philosophy
Graduate Department of Astronomy and Astrophysics
University of Toronto

Abstract

Photometric Properties of Galaxy Populations in Group and Cluster Environments

I-hui Li

Doctor of Philosophy

Graduate Department of Astronomy and Astrophysics

University of Toronto

2007

Using four-band photometric redshifts we explore photometric properties of galaxy populations in group and cluster environments at $0.20 \leq z < 0.60$. We probe red galaxy fractions (f_{red}) using samples of 76 galaxy clusters and $\sim 1,200$ galaxy groups from CNOC1 and RCS follow-up observations. Within all environments where both local galaxy density and cluster-centric radius are controlled, we observe galaxy down-sizing in star formation, as evidenced by the larger f_{red} possessed by bright galaxies than that by the faint ones. We find that the Butcher-Oemler effect is stronger within the cluster virial radius, where star formation is truncated more rapidly compared with the outskirts. Both bright and faint galaxies exhibit weak dependence of their f_{red} on local galaxy density beyond the cluster virial radius, indicating accelerated evolution driven by galaxy clusters. The gradients between f_{red} and local galaxy densities are larger for the bright galaxies at $z \sim 0.50$, but become similar for the bright and faint galaxies at $z \sim 0.30$. The cluster environmental influence is effective within ~ 1.5 virial radii and is stronger in high galaxy density regions, indicating that mechanisms such as harassment and tidal interactions are operating in high galaxy density locations, while ram-pressure is likely the main mechanism in regions of low galaxy density. For environments of similar local galaxy densities and at a fixed cluster-centric radius, galaxies in groups possess larger f_{red} than non-group galaxies, which is usually referred to as 'pre-processing'. We find that the pre-processing is independent of local galaxy density and global cluster environmental impact. Instead, the group environmental influence depends on group richness. We observe a 'group down-sizing' effect such that galaxies in rich groups (of more massive haloes) have their f_{red} evolving with redshift more rapidly than those in poor groups (of less massive haloes). This thesis concludes that the observed properties of galaxy populations result from the combination of their natural characteristics and surrounding environments. Galaxy intrinsic luminosity (mass) determines the efficiency in forming stars, and extrinsic environmental influence accelerates the truncation of star formation.

Acknowledgements

First and foremost, I would like to thank my supervisor Professor Howard K.C. Yee for his support and guidance. It has been an honor to be his student. I appreciate his dedicated and patient supervision to make my Ph.D. experience stimulating and prepare me for future challanges. I thank my committee members, Professors Roberto Abraham and Ray Carlberg, for their helpful suggestions and comments during my study, and Professor Michael De Robertis for his presence on the final examination committee. I grately acknowledge Dr. David Gilbank for the invaluable tutoring to improve my research skills.

I thank Dr. Michael Cooper and Dr. Darren Croton for providing me the Mellinnenium mock cones, which made an enssential step in the group-findng algorithm for this thesis. I appreciate the RCS CFHT photometric catalogs generated by Paul B.C. Hsieh.

Lastly, I am deeply indebted to my friends who added laughs and colors to my time in Toronto, especially Grantland, Hugh, Siow-wang, Emily, April and Violet. I also thank Brian Lee for his warmth and kindness, especially the sweet treats that he made and the thesis template. Life of a graduate student is not easy sometimes, being frustrating and stressful. I am grateful for the time spent with my friends. The getting-together dinners, pictures shooting, and all the silly stories made the Toronto life more enjoyable. Life is a journey. It is time to say good-bye to Toronto and the student life. No matter how this Toronto story begins, I know I have many treasured memories here. The Toronto sky is not so gloomy anymore, but I have to leave and move onto my next career step. I don't know how the life in the future will be, but I know there are always friends whom I can chat and share tears with. Thank you.

Contents

List of Tables

List of Figures

Chapter 1

Introduction

In standard galaxy formation models, galaxies condense at the centers of dark haloes (e.g., White & Rees 1978; Cooray & Sheth 2002). Haloes in high density regions form at earlier time, statistically, than haloes of the same mass but in less dense locations (e.g., Gao et al. 2005; Maulbetsch et al. 2007). The initial properties of the haloes accordingly are naturally imprinted on galaxies therein.

Hierarchically, galaxies join more and more systems as structure grows. Therefore, galaxies may experience different environments during their life-time. Observationally, properties of galaxies have been known to correlate with their environment. For example, most galaxies in high galaxy density regions have early-type morphologies, while those in locations of lower galaxy density tend to be late-type galaxies (the morphology-density relation; e.g., Dressler 1980; Hogg et al. 2006; Cassata et al. 2007). With an attempt to assess the role of environment on galaxy evolution, theoretical and observational studies historically have focused mainly on galaxy clusters. This is primarily because of the practical advantage of having a large number of galaxies in relatively small regions on the sky, and these galaxies are at a similar distance.

Galaxies evolve with time passively, and the environment complicates their evolution. It is believed that both 'Nature' and 'Nurture' have effects on galaxy formation and evolution, yet their relative roles are still not clear. To search for the consequences of natural evolution, galaxy properties should be probed in the same environment. On the other hand, to investigate the results nurtured by environment, the study should be conducted using galaxies of similar intrinsic properties. The topic of environmental influence on galaxy observational properties forms the main content of this thesis.

The most dense environment is associated with galaxy clusters. However, galaxy clusters offer biased environments for evolutionary studies. Theoretically, clusters originate

from the gravitational collapse of the highest peaks of primordial density perturbations, and evolutionary processes in these regions occur at an accelerated pace compared to regions of the Universe with average density. Galaxy clusters are thought to grow through the accretion of galaxies from surrounding filamentary structures (e.g., Fuller et al. 1999; Colberg et al. 2005). At the present time, only about 10% of galaxies are located in galaxy clusters, but the majority ($\geq$ 60%) of galaxies are sited in galaxy groups (e.g., Huchra & Geller 1982; Eke et al. 2004). The properties of galaxies in groups falling into clusters are therefore anticipated to be affected by both group and cluster environments. The environment where galaxies reside complicates galaxy evolution, and the investigation of environmental influence between smaller (groups) or larger (clusters) scales becomes essential.

Much recent work has focused on galaxy groups to probe such environmental dependence of galaxy properties on the basis of 'pre-processing' operating in galaxy groups (e.g., Mercurio et al. 2004; Cortese et al. 2006; Blanton et al. 2006). The term 'pre-processing' refers to the fact that star formation rate in galaxies of an infalling group has been truncated or ceased before the whole system falls into a more massive one, usually a galaxy cluster (Fujita 2004). Most of these works address galaxy groups in the nearby Universe. The exploration of galaxy groups at higher redshift ($z > 0.3$), however, still requires much effort. Galaxy groups are not easily observed at such redshift due to the small number of their members within high background counts, and low or nonexistent X-ray luminosity. Although there is no clear distinction between rich galaxy groups and poor galaxy clusters, most aspects of environmental influence in the current literature are explored either outside galaxy clusters or within the central regions of them. Owing to the large-scale gravitational potential field, galaxy clusters can transform the characteristics of galaxy populations, such as morphology and star forming activities, in infalling galaxies and perhaps groups.

Overall, *epoch*, *mass*, and *environment* (*local* and *global*) are the main factors in governing galaxy evolution. In an attempt to understand the environment-driven evolution of galaxy populations, studies should be conducted using samples of sufficient size extending over a range in redshift, and covering the regions associated with galaxy clusters, so that the dependence of galaxy properties on any of those factors can be investigated with the others controlled. This aim is the subject of this thesis.

In this introduction we first focus on the photometric properties of galaxies in different environments (§ 1.1). We then discuss the possible mechanisms active in galaxy clusters in affecting galaxy properties (§ 1.2). We follow with descriptions of local environmental

influence and the role of galaxy groups (§ 1.3). We also present an overview of techniques to estimate galaxy photometric redshift in § 1.4 and structure finding in § 1.5. Finally we present the goal and the structure of the thesis in § 1.6.

1.1 Photometric Properties of Galaxies

The first use of the terms 'early-' and 'late-' type galaxies has been forgotten long enough to recall its origin. Early-type galaxies generally refer to galaxies of morphological type from E to Sa. This type of galaxy has a wide range in mass. The most massive galaxies of this type are believed to be the oldest galaxies. Star formation either has stopped or is very weak in these galaxies; hence, early-type galaxies are red in color. In contrast, late-type galaxies are galaxies of morphological types from Sb to Irr. They have active star formation and some of them are intense enough to be called as star bursts. Therefore late-type galaxies are bluer in color.

In other words, galaxies can be roughly divided into red and blue classes by their colors, approximately corresponding to early and late types. Based on data from the Sloan Digital Sky Survey (SDSS; York et al. 2000), the distribution of galaxy colors in a sample can be described by a bimodal function approximated by the combination of two Gaussian functions (e.g., Strateva et al. 2001; Baldry et al. 2004; Ball et al. 2006). Balogh et al. (2004) separate galaxies into various luminosities and local galaxy density environments, and are able to show that galaxy bimodal colors are affected more by galaxy luminosity (mass) than local galaxy density. Bell et al. (2004) reveal that galaxy color bimodality exists up to $z \sim 1$. Yee et al. (2005) further consider the evolution of such galaxy color bimodality in different environments in two different redshift bins out to $z \sim 0.6$. Their study shows that the luminous blue population has the most dramatic change in the mean color distribution from $z \sim 0.5$ to $z \sim 0.1$ (combined with the studies of Balogh et al. (2004) using SDSS). The theoretical approach posits that galaxy color bimodality can be explained by the interplay between the merging history and star forming processes in the hierarchical clustering framework (Menci et al. 2005). A reasonable picture of the galaxy bimodal color distribution is that luminous galaxies are redder than faint galaxies, and the peak of the color for the blue star-forming galaxies has become redder toward the present day for a given magnitude and local environment.

This bimodal galaxy color distribution is reflected in the galaxy color-magnitude diagram, where red galaxies exhibit a tight correlation between galaxy color and magnitude as the 'red sequence', but blue galaxies populate a wide range in color and magnitude as

the 'blue cloud'. The formation of the red sequence is related to galaxy age and metallicity (e.g., Kodama & Arimoto 1997). The bright end of this sequence is believed to have been built up before $z \sim 0.8$, and faint red galaxies keep constructing the faint end of the sequence toward the recent Universe (e.g., Tanaka et al. 2005; de Lucia et al. 2007).

1.2 Clusters of Galaxies

Clusters of galaxies, collections of galaxies held together by mutual gravity, display a wide variety of richness containing from ~ 50 to $\sim 10,000$ galaxies. The richest ones are considered as the largest dynamically relaxed systems in the Universe. It has been known since early 1970 that cluster central regions are occupied by red early-type galaxies (Oemler 1974). The lack of blue star-forming galaxies brought to attention the relationship between galaxy properties and cluster environment. A milestone in the study of galaxy populations within galaxy clusters is the 'Butcher-Oemler' effect, arising from a series of photometric studies about galaxy evolution in clusters carried out by Butcher & Oemler (1978). With 33 clusters to $z \sim 0.5$, Butcher & Oemler (1984) conclude that clusters at higher redshift contain a larger fraction of blue galaxies compared to those at the present epoch. This 'excess of blue galaxies' in distant clusters compared with nearby clusters is commonly referred to as the 'Butcher-Oemler effect'.

The Butcher-Oemler effect is not a simple reflection of galaxy evolution in time, but more related to the correlation between star formation activities of galaxies and cluster environment. Considering the fact that cluster central regions are dominated by red galaxy populations, there must be mechanisms associated with galaxy clusters to stop star formation in infalling galaxies and make them become redder. For example, Ellingson et al. (2001) find that the Butcher-Oemler effect primarily exists for cluster galaxies beyond half of the virial radius and is not a strong function of galaxy luminosity. They suggest that the Butch-Oemler effect can be explained by a straightforward picture using infalling galaxies with truncated star formation; the reason that clusters at higher redshift containing more blue galaxies is because there are more galaxies dragged into clusters at higher redshift. On the other hand, Poggianti et al. (1999) conclude that intense star formation is induced in the infalling galaxies, depleting the gas contents in these galaxies.

Owing to the large gravitational field possessed by a rich galaxy cluster, where the velocity dispersion for the galaxies therein is about 800-1000 km/s, galaxy harassment is believed to be one of the active mechanisms in galaxy clusters (e.g., Moore et al.

1996, 1999). For a cluster like Coma, a typical galaxy can experience several close interactions with other cluster members over the course of its lifetime in the cluster, since the frequency of encountering other cluster galaxies can be approximated as

$$N \sim 4\frac{n}{250Mpc^{-3}}\left(\frac{r_p}{20kpc}\right)^2\left(\frac{\sigma_v}{1000km/s}\right)\left(\frac{t}{10Gyr}\right),$$

where n is the number density of galaxies in a cluster, r_p is the impact parameter, σ_v is galaxy velocity dispersion, and t is the age of the cluster (Mihos 2003).

Another possible physical mechanism in driving galaxy evolution in clusters of galaxies is the interaction with the intra-cluster medium (ICM) via ram-pressure stripping. X-ray studies have revealed that galaxy clusters present a large amount of intergalactic gas with temperature between $10^7 \sim 10^8$K. As proposed by Gunn & Gott (1972), the gas disk of a spiral galaxy orbiting around a cluster can be blown away if a wind can overcome the gravitational attraction between the stellar and gas disk:

$$P_{ram} = \rho_{ICM} v_g^2 > 2\pi G \sigma_* \sigma_{gas},$$

where P_{ram} is the ram pressure, ρ_{ICM} is the ICM density, v_g is the relative velocity of the galaxy with respect to ICM, G is the gravitational constant, and σ_* and σ_{gas} are the surface density of stars and cold gas within the galaxy disk. Bekki et al. (2002) show such ram-pressure stripping can be powerful, as $\sim 80\%$ of halo gas of a spiral galaxy can be stripped with a few Gyr when the galaxy orbits a cluster with a pericenter distance ~ 3 time larger than the cluster core radius.

In addition to ram-pressure stripping caused by the interaction with ICM, galaxy clusters may affect infalling galaxies by their tidal field (e.g., Richstone 1976; Merritt 1984; Gnedin 2003). As a galaxy moves through the cluster, it is subject to the gravitational force of their neighbors, as well as the cluster as a whole. Some stars and gas within a galaxy, especially those located in outer galactic regions, may be accelerated to velocities larger than the local escape velocity, hence being tidally stripped from the parent galaxy. When both ram-pressure and tidal stripping take place at the same time, such removal process can be much more effective than just either one of them alone (Mayer et al. 2006).

All these physical mechanisms have been raised to explain cluster environmental influence on galaxy population properties. Note that if the blue color in high-redshift cluster galaxies is caused by star formation, the main issue about the evolution of cluster galaxies would be what processes in galaxy clusters to trigger or suppress star formation activities in addition to the natural evolution sequence due to time.

1.3 Local Galaxy Environment

In addition to the environmental influence due to galaxy clusters, galaxy properties can also be affected by their local environment. Dressler (1980) find that the fractions of galaxy populations strongly depend on galaxy local environment. The fraction of spiral galaxies is about $80\% - 90\%$ in low galaxy density regions, and about $80\% - 90\%$ of ellipical and S0 galaxies populate high density sites. This increasing trend of late-type galaxies toward low galaxy density regions but more early-type galaxies in high galaxy density locations is common known as the 'morphology-density' relation.

Within the past decade the 'morphology-density' relation has generally been also interpreted as 'color-density' or 'SFR-density' relations, because galaxies of late-type morphology tend to be blue in color and active in star formation. Regions of low galaxy density are favored by blue, star-forming, late-type galaxies, and locations of high galaxy density are occupied mostly by red, passive, early-type galaxies. Kodama et al. (2001) demonstrate that color transition between galaxies is governed by a critical galaxy density, above which galaxies have their color shifted from blue to red. They suggest that such critical galaxy density corresponds to regions of sub-clumps within the filaments surrounding the clusters. Gómez et al. (2003) also present evidence of a critical galaxy density above which the star formation rate decreases. Despite the role of critical galaxy density in transforming galaxy properties being still controversial, it illustrates that local galaxy environment can significantly affect galaxy properties.

Galaxy groups are sites of relatively high galaxy density compared with the field, but not as dense as cluster environment. Thanks to the smaller gravitational potential and hence lower velocity dispersion among group galaxies, some physical mechanisms in clusters such as ram-pressure stripping or harassment may not be active in galaxy groups. However, the environment within galaxy groups hosts most galaxy mergers. For example, the merger rate for equal mass galaxies is related to the velocity and merger cross-section (Mamon 2000):

$$k = \frac{1}{n^2}\frac{d^2N}{dtdV} =< vs(v) >= \int_0^\infty dv f(v) vs(v),$$

where $s(v) = \pi[p_{crit}(v)]^2$ is the merger cross-section and $f(v)$ is the distribution of relative velocities. Within a virialized system with 1D velocity dispersion v, the velocity distribution is a Gaussian with standard deviation $\sqrt{2}v$. Integrating over the volume of the system, $nk = dN/dt$ is hence the rate at which a galaxy suffers merging. Given that the velocity dispersion within a galaxy group is typically $3 \sim 5$ times smaller than that

in galaxy clusters, the merger rate is $\sim 50-100$ times higher in galaxy groups than in clusters for fixed galaxy parameters.

Studies of comparing galaxy properties in groups and the field have suggested the processes that transform galaxies from active, star-forming, late-type galaxies to quiescent early-type galaxies is more effective in galaxy groups (e.g., Martínez et al. 2006; Balogh et al. 2007). Such galaxy evolution driven by group galaxy environment has an important role in building the structures in a hierarchical Universe, since galaxy clusters grow, instead of accreting individual galaxies randomly from the field environment, but through the infall of less massive groups falling in along the filaments (Mihos 2003). The most marked difference found between cluster cores and normal galaxy groups is the build-up of the red sequence, as cluster galaxies exhibit a tight correlation in galaxy color and magnitude, but galaxies in groups are still in the phase of moving toward the red sequence (Romeo et al. 2006; Tanaka et al. 2005; de Lucia et al. 2007). Therefore, infalling groups provide sites to study galaxy properties between low and high density regions.

1.4 Photometric Redshift Estimation

Galaxy redshift is one of the fundamental measurements in extragalactic astronomy. Traditionally, galaxy redshift is measured using line features in galaxy spectra. To obtain a spectrum, it requires observing over long integration time. Redshifts derived in this way can be as accurate to $\Delta v = 50-100$km/s.

An alternative way to estimate galaxy redshifts is to use broad-band photometry. Instead of observing narrow spectral features of galaxy spectra, the photometric redshift technique concentrates on broad features such as the 4000 Å break and the overall shape of galaxy spectral energy distribution (SED). The main advantage of this photometric redshift technique is its capability to estimate many galaxy redshifts simultaneously using images. The accuracy of redshifts derived using this technique is typically $\Delta z = 0.05-0.10$. For the purpose of studying individual galaxies, this redshift uncertainty is beyond the useful level. However, such uncertainty is tolerable for determining properties, statistically speaking, of samples with large numbers of galaxies.

There are two major approaches in the photometric redshift technique. One is to construct galaxy SEDs from their multi-passband photometry and then compare to those in an observed or synthetic library (e.g., Lanzetta et al. 1996; Fernández-Soto et al. 1999; Mobasher et al. 2006). This SED fitting method requires the knowledge of the evolution

of various galaxy SEDs with time, and is sensitive to the matching of the synthetic spectra to the actual SEDs. The other method is to obtain a relation between galaxy spectroscopic redshift and their magnitudes and colors, and then apply the same relation to galaxies with the same passband photometry. This empirical fitting method requires a set of galaxies, the training set, with accurate redshift and photometry in order to derive the solutions (e.g., Connolly et al. 1995; Brunner et al. 1997; Hsieh et al. 2005; Blake et al. 2007). This method is sensitive to any systematic differences between the training set and the input data. In both the SED and training set fitting methods, the redshift estimation is more secure if the filter sets are chosen to bracket some SED continuum features such as the 4000 Å break or the Lyman break at 912 Å.

Up to now, the photometric redshift technique has been used in numerous works. For example, the studies of galaxy evolution and star formation rate in the Hubble Deep Field (e.g., Sawicki et al. 1997; Volonteri et al. 2000; Thompson et al. 2001; Conti et al. 2003) and Chandra Deep Field-South (e.g., Sawicki & Mallén-Ornelas 2003; Mobasher et al. 2004; Franceschini et al. 2006). The technique is also widely applied in studies such as galaxy properties in various environments (e.g., Yee et al. 2005; Roche et al. 2006; Fritze-v. Alvensleben & Bicker 2006; van Dokkum et al. 2006).

1.5 Structure Finding

Structures are common in the hierarchical Universe, from empty voids to dense clusters. In the extreme over-dense regions, where galaxy clusters are located, structures are usually identified in either the X-ray or optical/IR regimes. The former relies on the detection of thermal bremsstrahlung emission from the intra-cluster medium, and can be effective up to $z \sim 0.75$ (e.g., Rosati et al. 1998). The latter is the direct detection of the cluster galaxies using imaging data in one or more passbands (e.g., Postman et al. 1996; Gladders & Yee 2005)

However, structures in less dense regions are not easy to detect, owing to little hot gas content or small number of galaxies. Most structures in these regions are galaxy groups. A way to identify galaxy groups is to search for local over-dense regions above a density threshold, adopted by Huchra & Geller (1982) using the Center for Astrophysics (CfA) redshift survey. This group identification, known as the 'friends-of-friends' (FOF) algorithm, depends on a set of linking parameters to define the maximum spatial separation in any galaxy pairs. Because of its simplicity in looking for neighboring galaxies, this group-finding technique has been extensively applied to spectroscopic redshift surveys

(e.g., Merchán et al. 2000; Tucker et al. 2000; Ramella et al. 2002; Carlberg et al. 2001; Berlind et al. 2006) or N-body simulations (e.g., Valageas et al. 2000; Warren et al. 2006; Bett et al. 2007).

As described in § 1.4, the photometric redshift technique offers an alternative in estimating redshift for large numbers of galaxies but it also gives large uncertainties in the estimation. In any application of the friends-of-friends method to identify structures in a photometric redshift sample, the standard friends-of-friends must be modified to consider the fuzzy information in redshift space. Finding structures using photometric redshifts has become an issue nowadays (e.g., Botzler et al. 2004; Trevese et al. 2007), so that studies of galaxy properties in various environments can be extended using large survey data and to high redshift. As this thesis focuses on environmental dependence of galaxy properties and their evolution from $z \sim 0.60$ to $z \sim 0.20$ using photometric redshift samples, one of the efforts of this thesis is to develop a modified friends-of-friends algorithm to identify galaxy groups, and obtain sizable catalogs of galaxy groups at $0.2 \leq z < 0.6$.

1.6 The Thesis

The thesis investigates the dependences of galaxy photometric properties on various environmental influences along the time sequence. Galaxies evolve with time. Galaxies of different luminosity may reflect the differences in their intrinsic characteristics, such as mass. It is believed that environment affects galaxy properties. The various environmental impacts include the influences related to local galaxy density, galaxy groups, and galaxy clusters. It is possible for several environmental influences to be active at the same time in affecting galaxy properties. The main aim of this thesis is to investigate how galaxy properties correlate with various environments at different redshifts. Specifically, the thesis focuses on which environmental influence is more dominant at a fixed location, whether it gives a similar effect on galaxies of different luminosities, and how such environmental influence evolves with redshift. The thesis emphasizes the trends of red galaxy fractions as a function of only one environmental variable with others controlled.

The thesis consists of seven chapters in total, each of which addresses an aspect of environmental influence on galaxy properties of the samples over the redshift range of 0.2 to 0.6. The samples are obtained from the follow-up data sets of the Canadian Network for Observational Cosmology Survey (CNOC; Yee et al. 1996) and the Red-Sequence Survey (RCS; Gladders & Yee 2005). The remaining chapters of the thesis, apart from

the Introduction (this chapter), are outlined below.

1.6.1 Chapter 2: Finding Galaxy Groups In Photometric Redshift Space: the Probability Friends-of-Friends Algorithm

This chapter describes a group finding algorithm developed to identify galaxy groups using photometric redshift. The photometric redshift technique is presented in this chapter as well. In short, the group finding algorithm relies on the conditional photometric redshift probability density of a galaxy group. The estimation of the group redshift will be improved when there are more galaxies linked to form a group. The algorithm is tested using Virgo Consortium Millennium Simulations (Springel et al. 2005) and also applied to the CNOC2 redshift survey data, showing that the algorithm works excellently. In subsequent chapters, we apply the photometric redshift and group finding techniques to data from the CNOC1 and RCS follow-up multi-color imaging.

1.6.2 Chapter 3: Environment Measures and Computation of Galaxy Population Fraction

This chapter defines the parameters for quantifying different environments that will be used in subsequent chapters. These parameters include local projected galaxy density, cluster- and group-centric radii, and group richness. In a given location, different environmental influences may be effective at the same time. Hence, galaxy properties should be probed as a function of only one environmental variable at a time with others controlled. In this chapter we also present the computation method for the red fraction of galaxies, which is used as a proxy for galaxy population and star formation properties.

1.6.3 Chapter 4: The Individual and Group Galaxies in X-ray Selected Clusters: the CNOC1 Sample

This chapter presents the dependence of red galaxy fractions on environment using the Canadian Network for Observational Cosmology Survey (CNOC1; Yee et al. 1996) sample. The cluster samples are X-ray selected and hence well virialized. The Butcher-Oemler effect is explored using cluster galaxies in the identified cluster main groups, within 1 R_{200} and 1-1.5R_{200} (R_{200} is the virial radius within which density is 200 times the critical density). Dividing individual cluster galaxies into bins by their cluster-centric

radii, local projected galaxy density, and luminosity, the red galaxy fraction is explored in different environments. The cluster galaxies are also classified into two subsamples as group and non-group galaxies based on their group membership. The analyses focus on the differences in red galaxy fractions between these two subsamples. This chapter gives preliminary results of environmental influence on galaxy properties.

1.6.4 Chapter 5: Individual Galaxies in Optically Selected Clusters: the RCS Sample

This chapter presents the results of environmental influence using individual cluster galaxies in the RCS sample, whose sample size is larger than the CNOC1 sample by a factor of $\sim$4. We focus on the properties of individual cluster galaxies in environments related to local projected galaxy density and global cluster-centric radii. The galaxies are classified into two luminosity subsamples. Within a fixed environment at a redshift interval, any differences in red galaxy fractions among different luminosity subsamples reflect their differentiated intrinsic properties. For galaxies of similar luminosities but located in different environments, the differences in the red galaxy fractions are the outcomes of environmental influence. The local environmental effect is investigated at different cluster-centric radii, and the global cluster environmental influence is probed within various fixed local projected galaxy density regions.

1.6.5 Chapter 6: Galaxy Groups in the RCS Sample

This chapter focuses on galaxy groups in the RCS sample in two main topics. They are (1) properties of galaxy groups in general, and (2) galaxy groups in the same redshift space as the clusters. The first topic addresses the differences in red galaxy fractions within galaxy groups of different richness and luminosities, and also on properties of group members at different group-centric radii. The second topic concentrates on the differentiations between group and non-group galaxies in cluster environment, and also on infalling galaxy groups to probe whether the cluster environment causes any changes in the properties of galaxy groups. The differences between galaxy groups and clusters are compared and presented in this chapter as well.

We summary the results of each chapter in Chapter 7. Several projects and follow-up observations targeting galaxy groups can be developed based on the thesis. We outline the future plans in Chapter 7 as well.

Lastly, the level of the participation by various collaborators to the technical work in this thesis are presented as below. The observations and reduction of the classical observed CNOC1 follow-up images were done by collaborators in Colorado, while the calibration and photometric catalogs were created as my own contribution. The RCS is a long-term massive project, carried out in the R_c and z' passbands. The data reductions and cluster catalogs were created by Michael Gladders, as the main context of his Ph.D. thesis. The RCS follow-up observations where carried out in B and V passbands at CFHT and CTIO for the Northern and Southern sky, respectively. The photometric catalogs of the CFHT set were generated by Bau-Ching Hsieh as part of his Ph.D. project, while the CTIO follow-up is done entirely as part of this thesis. In particular, I was involved directly in collecting multi-band photometry over 7 deg^2 in the RCS follow-up observation using CTIO MOSAIC II. I reduced this RCS-CTIO dataset, performed object finding and photometry, and created both photometrically and astrometrically calibrated catalogs. More descriptions of each follow-up data set can be found in Chapter 4 and Chapter 5.

References

Baldry, I. K., Glazebrook, K., Brinkmann, J., Ivezić, Ž., Lupton, R. H., Nichol, R. C., & Szalay, A. S. 2004, ApJ, 600, 681

Ball, N. M., Loveday, J., Brunner, R. J., Baldry, I. K., & Brinkmann, J. 2006, MNRAS, 373, 845

Balogh, M. L., Baldry, I. K., Nichol, R., Miller, C., Bower, R., & Glazebrook, K. 2004, ApJ, 615, L101

Balogh, M. L., et al. 2007, MNRAS, 374, 1169

Bekki, K., Couch, W. J., & Shioya, Y. 2002, ApJ, 577, 651

Bell et al. 2004, ApJ, 608, 752

Berlind, A. A., et al. 2006, ApJS, 167, 1

Bett, P., Eke, V., Frenk, C. S., Jenkins, A., Helly, J., & Navarro, J. 2007, MNRAS, 60

Blake, C., Collister, A., Bridle, S., & Lahav, O. 2007, MNRAS, 374, 1527

Blanton, M. R., Berlind, A. A., & Hogg, D. W. 2006, ArXiv Astrophysics e-prints

Botzler, C. S., Snigula, J., Bender, R., & Hopp, U. 2004, MNRAS, 349, 425

Brunner, R. J., Connolly, A. J., Szalay, A. S., & Bershady, M. A. 1997, ApJ, 482, L21+

Butcher, H. & Oemler, Jr., A. 1978, ApJ, 219, 18

—. 1984, ApJ, 285, 426

Cassata, P., et al. 2007, ArXiv Astrophysics e-prints

Cattaneo, A., Dekel, A., Devriendt, J., Guiderdoni, B., & Blaizot, J. 2006, MNRAS, 370, 1651

Colberg, J. M., Krughoff, K. S., & Connolly, A. J. 2005, MNRAS, 359, 272

Connolly, A. J., Csabai, I., Szalay, A. S., Koo, D. C., Kron, R. G., & Munn, J. A. 1995, AJ, 110, 2655

Conti, A., et al. 2003, AJ, 126, 2330

Cooray, A. & Sheth, R. 2002, Phys. Rep., 372, 1

Cortese, L., Gavazzi, G., Boselli, A., Franzetti, P., Kennicutt, R. C., O'Neil, K., & Sakai, S. 2006, A&A, 453, 847

Cowie, L. L., Songaila, A., Hu, E. M., & Cohen, J. G. 1996, AJ, 112, 839

De Lucia, G., et al. 2007, MNRAS, 374, 809

Dressler, A. 1980, ApJ, 236, 351

Eke, V. R., et al. 2004, MNRAS, 348, 866

Ellingson, E., Lin, H., Yee, H. K. C., & Carlberg, R. G. 2001, ApJ, 547, 609

Faber, S. M., Trager, S. C., Gonzalez, J. J., & Worthey, G. 1995, in IAU Symp. 164: Stellar Populations, ed. P. C. van der Kruit & G. Gilmore, 249–+

Fernández-Soto, A., Lanzetta, K. M., & Yahil, A. 1999, ApJ, 513, 34

Finlator, K., Davé, R., Papovich, C., & Hernquist, L. 2006, ApJ, 639, 672

Franceschini, A., et al. 2006, A&A, 453, 397

Fritze-v. Alvensleben, U. & Bicker, J. 2006, A&A, 454, 67

Fujita, Y. 2004, PASJ, 56, 29

Fuller, T. M., West, M. J., & Bridges, T. J. 1999, ApJ, 519, 22

Gladders, M. D. & Yee, H. K. C. 2005, ApJS, 157, 1

Gnedin, O. Y. 2003, ApJ, 582, 141

Gómez, P. L., et al. 2003, ApJ, 584, 210

Gunn, J. E. & Gott, J. R. I. 1972, ApJ, 176, 1

Hogg, D. W., Masjedi, M., Berlind, A. A., Blanton, M. R., Quintero, A. D., & Brinkmann, J. 2006, ApJ, 650, 763

Gao, L., Springel, V., & White, S. D. M. 2005, MNRAS, 363, L66

Hsieh, B. C., Yee, H. K. C., Lin, H., & Gladders, M. D. 2005, ApJS, 158, 161

Huchra, J. P. & Geller, M. J. 1982, ApJ, 257, 423

Kodama, T. & Arimoto, N. 1997, A&A, 320, 41

Kodama, T., Smail, I., Nakata, F., Okamura, S., & Bower, R. G. 2001, ApJ, 562, L9

Lanzetta, K. M., Yahil, A., & Fernández-Soto, A. 1996, Nature, 381, 759

Mamon, G. A. 2000, in Astronomical Society of the Pacific Conference Series, Vol. 197, Dynamics of Galaxies: from the Early Universe to the Present, ed. F. Combes, G. A. Mamon, & V. Charmandaris, 377–+

Martínez, H. J., O'Mill, A. L., & Lambas, D. G. 2006, MNRAS, 372, 253

Maulbetsch, C., Avila-Reese, V., Colín, P., Gottlöber, S., Khalatyan, A., & Steinmetz, M. 2007, ApJ, 654, 53

Mayer, L., Mastropietro, C., Wadsley, J., Stadel, J., & Moore, B. 2006, MNRAS, 369, 1021

Menci, N., Fontana, A., Giallongo, E., & Salimbeni, S. 2005, ApJ, 632, 49

Merchán, M. E., Maia, M. A. G., & Lambas, D. G. 2000, ApJ, 545, 26

Mercurio, A., Busarello, G., Merluzzi, P., La Barbera, F., Girardi, M., & Haines, C. P. 2004, A&A, 424, 79

Merritt, D. 1984, ApJ, 276, 26

Mihos, C. 2003, ArXiv Astrophysics e-prints

Mobasher, B., et al. 2006, ArXiv Astrophysics e-prints

Mobasher, B., et al. 2004, ApJ, 600, L167

Moore, B., Katz, N., Lake, G., Dressler, A., & Oemler, A. 1996, Nature, 379, 613

Moore, B., Lake, G., Quinn, T., & Stadel, J. 1999, MNRAS, 304, 465

Oemler, A. J. 1974, ApJ, 194, 1

Ostriker, J. P., Bode, P., & Babul, A. 2005, ApJ, 634, 964

Poggianti, B. M., Smail, I., Dressler, A., Couch, W. J., Barger, A. J., Butcher, H., Ellis, R. S., & Oemler, A. J. 1999, ApJ, 518, 576

Postman, M., Lubin, L. M., Gunn, J. E., Oke, J. B., Hoessel, J. G., Schneider, D. P., & Christensen, J. A. 1996, AJ, 111, 615

Ramella, M., Geller, M. J., Pisani, A., & da Costa, L. N. 2002, AJ, 123, 2976

Richstone, D. O. 1976, ApJ, 204, 642

Roche, N. D., Dunlop, J., Caputi, K. I., McLure, R., Willott, C. J., & Crampton, D. 2006, MNRAS, 370, 74

Romeo, A. D., Napolitano, N. R., Covone, G., & Sommer-Larsen, J. 2006, ArXiv Astrophysics e-prints

Rosati, P., della Ceca, R., Norman, C., & Giacconi, R. 1998, ApJ, 492, L21+

Sawicki, M. J., Lin, H., & Yee, H. K. C. 1997, AJ, 113, 1

Sawicki, M. & Mallén-Ornelas, G. 2003, AJ, 126, 1208

Springel et al. 2005, Nature, 435, 629

Strateva et al. 2001, AJ, 122, 1861

Tanaka, M., Kodama, T., Arimoto, N., Okamura, S., Umetsu, K., Shimasaku, K., Tanaka, I., & Yamada, T. 2005, MNRAS, 362, 268

Thompson, R. I., Weymann, R. J., & Storrie-Lombardi, L. J. 2001, ApJ, 546, 694

Trevese, D., Castellano, M., Fontana, A., & Giallongo, E. 2007, A&A, 463, 853

Tucker, D. L., et al. 2000, ApJS, 130, 237

Valageas, P., Lacey, C., & Schaeffer, R. 2000, MNRAS, 311, 234

van Dokkum, P. G., et al. 2006, ApJ, 638, L59

Volonteri, M., Saracco, P., Chincarini, G., & Bolzonella, M. 2000, A&A, 362, 487

Warren, M. S., Abazajian, K., Holz, D. E., & Teodoro, L. 2006, ApJ, 646, 881

White, S. D. M. & Rees, M. J. 1978, MNRAS, 183, 341

Yee, H. K. C., Ellingson, E., & Carlberg, R. G. 1996, ApJS, 102, 269

Yee, H. K. C., Hsieh, B. C., Lin, H., & Gladders, M. D. 2005, ApJ, 629, L77

York, D. G., et al. 2000, AJ, 120, 1579

Chapter 2

Finding Galaxy Groups In Photometric Redshift Space: the Probability Friends-of-Friends Algorithm

2.1 Introduction

Galaxy groups are the sites where local galaxy number density is relatively higher than the field. The majority ($\sim 60\%$) of galaxies lies in groups (e.g., Eke et al. 2004; Berlind et al. 2006; Tago et al. 2006), so that galaxy groups provide excellent locations to study the effect of local environment on galaxy formation and evolution. However, galaxy groups, especially at high redshift, are not easy to detect because of their smaller size of galaxy aggregation and the significantly lower hot gas density. The current published galaxy group catalogs are constructed based on ambitious large-structure galaxy redshift surveys using automated group finding schemes. The techniques include the popular friends-of-friends algorithm (e.g., Geller & Huchra 1983; Eke et al. 2004; Merchán & Zandivarez 2005) and the Voronoi partition technique (e.g., Gerke et al. 2005). Most of these catalogs list galaxy groups either in the nearby Universe ($z < 0.1$) or over a small sky area. Galaxy groups in intermediate and higher redshift space of large sample sizes still remain largely unexplored.

Up to now, most structure finding techniques use spectroscopic redshift or simulated catalogs, both containing accurate three-dimensional position information. With the

development of the photometric redshift method, the approximate redshifts of all galaxies in a photometric multi-band survey can be obtained without the time-consuming spectroscopic measurements. The photometric redshift method involves the SED fitting technique (e.g., Bolzonella et al. 2000; Chen et al. 2003; Mobasher et al. 2004; Weinstein et al. 2004; Budavári et al. 2005; Brodwin et al. 2006) or using spectral 'training set' to calibrate the photometric redshift via an empirical polynomial of galaxy color and magnitude (e.g., Connolly et al. 1995; Hsieh et al. 2005). As the redshifts are derived from broadband galaxy colors rather than from spectra, the photometric redshift method can estimate the redshifts of objects which are too faint for spectroscopy. In comparison with spectroscopic measurements, redshifts estimated using photometric redshift technique have larger uncertainties by a factor of $50-100$. Due to the less accurate distance information in photometric redshift catalogs, the main problem of structure finding is the blurring of configurations in redshift space, producing unrealistic or elongated structures caused by the large photometric redshift uncertainties (Botzler et al. 2004). Even with excellent photometric redshift estimation ($\sigma_z \sim 0.03$), the structures on the small scale will still be greatly smeared out. Furthermore, projection effects make the subtraction of foreground and background galaxy contamination important in analyzing the structure found using photometric redshift.

In order to overcome these problems, we propose here a method of finding galaxy groups in photometric redshift catalogs. The knowledge of each galaxy's photometric redshift uncertainty or probability density is required for this method. This group finding methodology rests on the idea of the standard friends-of-friends algorithm in the transverse direction, but considers the photometric redshift probability density to determine the friendship in the radial direction. We describe the photometric redshift technique and the error estimation for individual galaxies in §2.2, and present sample selection in §2.3. The group-finding algorithm is detailed in §2.4. The basic properties of galaxy groups are quantified in §2.6. This algorithm is tested in §2.7 using the mock catalogs constructed from Virgo Consortium Millennium Simulation (Springel et al. 2005), and applied to the real observed groups in the *Canadian Network for Observational Cosmology Survey* in §2.8 (CNOC2; Yee et al. 2000). Finally, we present the summary in §2.9. The analysis of galaxy group samples will be presented in subsequent chapters. We adopt the standard cosmological parameters, H_0=70 km/s/Mpc, $\Omega_m = 0.3$, and $\Omega_\Lambda = 0.7$.

2.2 Empirical Photometric Redshift

2.2.1 Training set

Our photometric redshift method is based on the empirical fitting technique (e.g., Connolly et al. 1995; Hsieh et al. 2005). We express the galaxy redshift as a quadratic polynomial in magnitudes and colors:

$$z_i = a_0 + \sum a_i m_i + \sum a_{ij}(m_i - m_j)^2, \tag{2.1}$$

where m_i and m_j are the passband photometry and a_0, a_i and a_{ij} are the constant term and coefficients associated with photometry and color, respectively. The coefficients in the above equation can be derived by conducting the fitting using a training set, a catalog which contains both galaxy redshift and photometry information.

Our training set is constructed using data from the *Red-Sequence Cluster Survey* (RCS; Gladders & Yee 2005) in four CNOC2 survey patches (Yee et al. 2000) and the GOODS/HDF-N field (Giavalisco et al. 2004).

The RCS was designed to find galaxy clusters at $0.4 < z < 1.4$ using the cluster red-sequence method with R_c and z' filters. It covers 22 widely separated patches with a total of 90 deg^2, observed with the CFHT 12K camera in the Northern Hemisphere and the CTIO 4m MOSAIC II camera for the Southern Sky. The RCS follow-up covers 33.6 deg^2 (corresponding to about 75 % of the CFHT RCS fields) observed with the 12k camera in B and V. The photometry has been carried out using **ppp** (Yee 1991; Yee et al. 1996) and internally calibrated using star colors and galaxy counts. Moreover, it has been cross checked with star color and counts from *Sloan Digital Sky Survey (SDSS)* Data Release 3 (DR3; Abazajian et al. 2005). The RCS follow-up sample is 100% complete to $R_c \sim 24.2$. Further details on the data and on the photometric technique can be found in Hsieh et al. (2005). The CNOC2 survey covers over 1.5 deg^2 of sky with a total sample of $\sim$ 6200 redshifts (up to $z \sim 0.55$) with $R_c \leq 22.0$ available, 1727 of these galaxies overlap with the RCS sample.

The GOODS HDF-N field allowed us to extend our training set sample to larger redshifts. The GOODS is a survey based on multi-band imaging data obtained with the Advanced Camera for Surveys (ACS) on Hubble Space Telescope (HST). It covers two fields, HDF-N and CDF-S, with a total area of about 320 arcmin^2, a 5σ limiting magnitude in R passband (on the AB system) of 26.6, and a redshift range from 0.5 to 1.5. We have used publicly available $BVRz'$ photometry (Capak et al. 2004) and spectroscopic redshift (Wirth et al. 2004; Cowie et al. 2004) for 2661 galaxies in the

HDF-N field. To match the RCS zero point, GOODS magnitudes have been corrected following Hsieh et al. (2005). As a whole, our training set contains 3,988 galaxies. Further details on the properties of this training sample can be found in Hsieh et al. (2005).

2.2.2 Photometric Redshift Estimation and Associated Error

Because galaxies at high redshift tend to be fainter and redder, we separate the training set galaxies into 19 color-magnitude cells in the observed frame (Fig. 2.1) to differentiate roughly different types of galaxies. To create these cells, we first sort the training set galaxies by magnitude and color, so that any cell is created starting from the region where bright and red galaxies are on the observed color-magnitude diagram. We use slopes of -0.084 and -0.60 for the two sets of parallel lines to create the cells. The slope of -0.084 is chosen based on the red sequence slope at $z \sim 0.4$ in $B - R_c$, and the other slope is determined according to the galaxy distribution for different redshift bins on the color-magnitude diagram. We let a cell grow by $\Delta(B - R_c) = 0.1$ and $\Delta R_c = 0.1$ in every step until the cell contains at least 160 training set galaxies. Galaxies with unknown redshift are then classified into these cells according to their colors and magnitudes. The coefficients of equation 2.1 are obtained by means of a linear regression method in each color-magnitude cell using the training set galaxies. These coefficients are then applied to those galaxies in the same color-magnitude cell to estimate their redshift.

The photometric redshift uncertainties are estimated by bootstrapping the training set galaxies and applying a Monte-Carlo method on galaxy photometry. To estimate the photometric redshift uncertainties due to fitting, we bootstrap the training set galaxies in each color-magnitude cell 300 times with the assumption of perfect photometry in each galaxy. On the other hand, to evaluate the contribution from photometric uncertainties, we use a Monte-Carlo method to simulate galaxy magnitudes in each passband for 300 draws with Gaussian photometry uncertainties assumed. With these 300×300 realizations, we build the photometric redshift probability density of each galaxy and take the r.m.s. dispersion as the photometric redshift uncertainty for the galaxy. The photometric redshift of each galaxy is the median value of these 300×300 executions.

To investigate how the empirical photometric redshift uncertainties resemble the true ones, we define the empirical photometric redshift uncertainty σ_{emp} in a color-magnitude cell as the median empirical photometric redshift uncertainties of the training set galaxies in that cell. We also compute the dispersion between photometric and spectroscopic redshifts in the same color-magnitude cell and take it as the true uncertainty, denoted

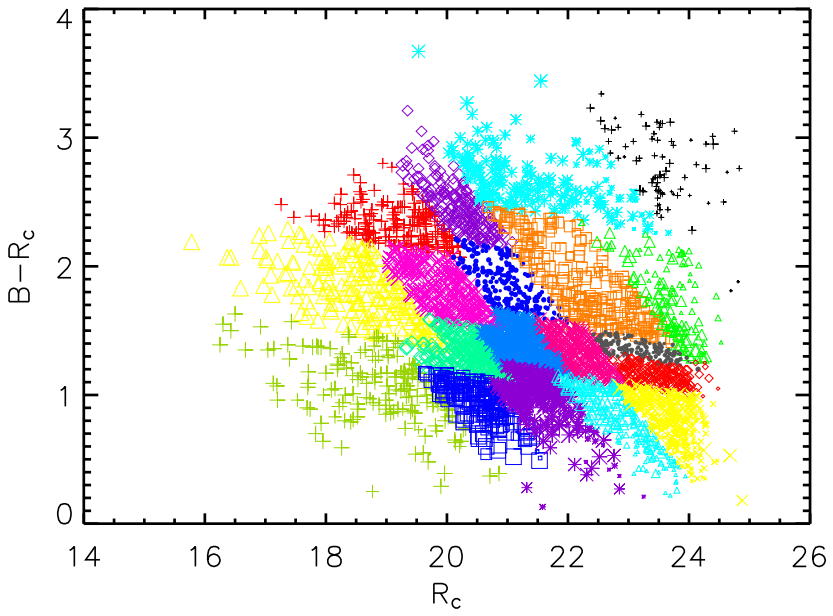

Figure 2.1: The training set galaxies are classified into 19 color-magnitude cells in our empirical photometric fitting method. The different symbols with different shading indicate the training set galaxies in different color-magnitude cells, with smaller sizes for higher redshift galaxies. The slopes for the two sets of parallel lines are -0.084 and -0.60 for the purpose of mimicking the rough differentiation of different types of galaxies at various redshift.

as σ_{true}. We find that there is a linear correlation between σ_{emp} and σ_{true}, but not of unity slope. Therefore, we scale the empirical photometric redshift uncertainties and the probability densities by a factor of $\sigma_{true}/\sigma_{emp}$ in each color-magnitude cell.

To test whether there is any systematic offset between the photometry of the training set and galaxies requiring photometric redshift, we drop every tenth galaxies in our training set (398 galaxies in number) as galaxies whose redshifts are to be estimated by the remaining training set galaxies (3590 galaxies in total), so that these two sets are independent, ensuring an unbiased estimation of the performance of our photometric redshift technique. The comparison of photometric redshift and spectroscopic redshift is illustrated by Fig. 2.2. The dispersion of $\Delta z = z_{phot} - z_{spec}$ is ~ 0.060 for these 398 galaxies using $BVRz'$ photometry at $0 \leq z_{spec} < 1$.

Fig. 2.3 plots the estimated photometric redshift uncertainties as a function of galaxy magnitude and color. We observe that the photometric redshift uncertainties become larger toward the faint and blue ends. This is encouraging for our technique of photo-

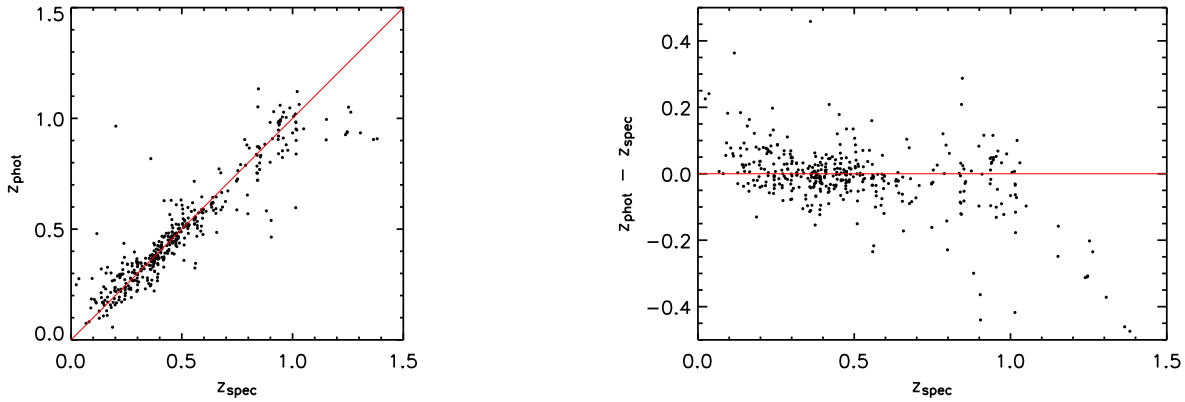

Figure 2.2: The comparison between spectroscopic and photometric redshifts for 398 galaxies in $BVRz'$ trained by 3590 training set galaxies quadratically. The dispersion in redshift difference is ~ 0.060 at $0 \leq z < 1$.

metric redshift uncertainty estimation, because bright and red galaxies usually have more accurate estimated photometric redshift measurements, owing to the better photometry measurements and the dominant features in their SEDs.

2.3 Sample Completeness Weight

Even though the photometric redshift technique can estimate a redshift for numerous galaxies economically, some galaxies, especially the extremely faint ones or those with unreliable photometry, may fail in the photometric redshift measurement. Moreover, some galaxies may have huge uncertainties in their photometric redshift measurements. These galaxies with improper photometric redshift measurements should be excluded in actual use. However, corrections in the galaxy counts are necessary to account for such rejection. The selection of galaxies in a photometric redshift catalog can be based on (1) photometric redshift ranges which the 4000Å break in SED is within the used passband ranges, and (2) the total probability within a desired redshift range to ensure the quality of photometric redshift measurement.

We set the redshift range as $0.02 \leq z < 1.4$ where the upper photometric redshift limit is due to the passband wavelength coverage for the 4000Å break in our training set. We also select galaxies whose total probability within $3\sigma_{z_c ut}$ of its central photometric redshift is greater than 99.7%, where $\sigma_{z_c ut}$ is set as $\sigma_{z_c ut} = 0.2(1+z)$.

As we select whether an object is in the sample or not, a completeness correction

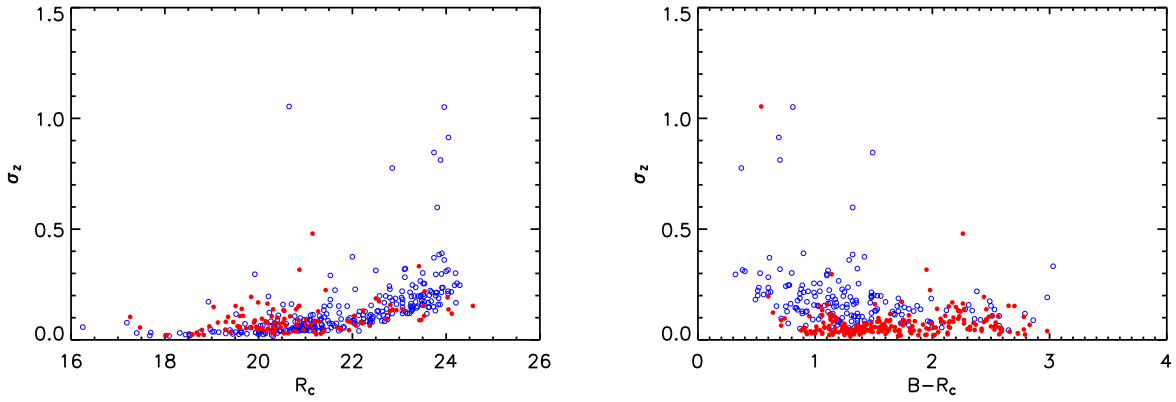

Figure 2.3: (a) The empirical photometric redshift uncertainties as a function of magnitude for the 398 control test galaxies. The open circles represents blue galaxies ($B - R_c < 1.8$) and filled ones symbolize red galaxies ($B - R_c \geq 1.8$). (b) Similar to (a) but as a function of $B - R_c$ color. Filled circles are for bright galaxies ($R_c < 21.5$) and open circles represent faint galaxies ($R_c \geq 21.5$).

weight w_i is assigned to each galaxy. The completeness factor is estimated using the ratio of the total galaxy number within $\Delta m_{R_c} = 0.1$ magnitude bin to the total galaxy number satisfying our selection in the same magnitude bin, because we find that both red and blue galaxies have similar completeness correction weights. In general, this completeness weight becomes larger for fainter galaxies. Therefore, a nominal apparent magnitude cutoff can be set based on where $w_i = 2$ to avoid galaxies of high weights. This magnitude is $m_{R_c} \sim 23.0$ for our training set. The median and averaged completeness correction factor is ~ 1.030 and ~ 1.092 for our training set galaxies applied with the same sample selection criteria.

2.4 Parameters for the Friendship

We wish to find galaxy groups using only photometric redshift instead of spectroscopic redshift, therefore, we develop a group-finding algorithm using photometric redshift. We follow the idea of the well-known friends-of-friends algorithm in angular separation; however, we consider the conditional photometric redshift probability in the redshift direction.

2.4.1 The 2D Linking Length, D0

The standard friends-of-friends algorithm (FOF; Geller & Huchra 1983) identifies over-dense regions by looking for galaxies closer to one another than a given cutoff separation. A group forms from a seed galaxy. Galaxies satisfying the linking criterion to this seed galaxy are linked together. A galaxy group is defined by the chains of such finding procedures using every linked galaxy as a new seed. We adopt this linking idea in our algorithm to search for group members in the transverse direction. Given a fixed 2D reference linking length $D0_{xy}$ at z=0, the linking length used to unite galaxies should be scaled as $D0_{xy}/(1+z)$ for the sake of forming groups of similar over-density. However, in an apparent-magnitude limited survey, criteria based on the distance between galaxies have to consider the variation of the mean galaxy separation with redshift (Marinoni et al. 2002; Eke et al. 2004). The apparent magnitude cutoff of a survey causes sparser galaxy number density at higher redshift. In order to form galaxy groups of similar over-density regions throughout the survey, the linking length should take account of the varying absolute magnitude cutoffs at different redshifts where the galaxy number density becomes incomplete. The linking length is scaled as:

$$D0 \propto R_w^{1/2},$$

where

$$R_w = \left(\frac{\int_{-\infty}^{M_{cut}} \Phi(M) dM}{\int_{-\infty}^{M_{lim}} \Phi(M) dM} \right). \tag{2.2}$$

In Equation 2.2, M_{cut} is the desired absolute magnitude depth, M_{lim} is the magnitude limit of a survey in absolute magnitude, and $\phi(M)$ is the galaxy luminosity function. We take $\phi(M)$ to be the standard Schechter's luminosity function, and the luminosity evolution is approximated as $M(z) = M(0) - zQ$ where Q=1.24 for red galaxies and Q=0.11 for blue galaxies (Lin et al. 1999). We adopt $M^*_{R_c}$=-21.41 and the faint end slope $\alpha = -1.20$ (Kodama & Arimoto 1997). This scaling factor R_w is unity if $M_{cut} < M_{lim}$.

In addition, only galaxies in the sample with reasonable photometric redshift uncertainties are passed through the group finding procedure. We increase the linking length by $\sqrt{\frac{\sum_i^N w_i}{N}}$ to conserve the local galaxy number density due to the removal of bad-quality galaxies, where N is the total galaxy number joined into a group and w_i is the completeness weight (described in § 2.3) of each linked galaxy.

In practice, our linking length used to search for connected galaxies in the transverse

direction is expressed as:

$$D0 = \sqrt{\frac{R_w \sum_i^N w_i}{N}} \frac{D0_{xy}}{1+z}, \tag{2.3}$$

taking into considerations of the completeness weight and the variation of galaxy number density with redshift.

2.4.2 The Redshift Friendship Criterion, $P_{ratio,crit}$

In the ideal situation where there is no uncertainty in the redshift, the occurrence of a galaxy or group at its redshift is a δ function. From a statistical viewpoint, the occurrence of an event in photometric redshift space for each galaxy is independent in the sense that the photometric redshift of each galaxy is estimated by applying a set of solutions in an empirical method. Given that galaxy A, galaxy B, ... , and galaxy n with photometric redshift density $P_A(z), P_B(z)$, ... , and $P_n(z)$ form a group in redshift, the group redshift density is the likelihood for all these n members to occur at the same redshift:

$$P_{group}(z) = P_A(z)P_B(z)...P_n(z).$$

Therefore, the main idea of our group-finding algorithm is to narrow down the photometric redshift uncertainty of a group by way of joining new galaxy members, because the group redshift is where all members in the same group should occur.

Whether a galaxy is in the same redshift space as another galaxy is determined by the overlapping probability based on their photometric redshift probability density. We use a probability ratio, P_{ratio}, as the criterion to set the membership in redshift. Given two galaxies with Gaussian photometric redshift probability density $P_{z_1,\sigma_1}(z)$ and $P_{z_2,\sigma_2}(z)$, respectively, where z_1 and z_2 are the photometric redshifts for these two galaxies, and σ_1 and σ_2 are the uncertainties, the total probability for these two galaxies to occur at the same redshift is

$$P(z) = \int_0^\infty P_{z_1,\sigma_1}(z')P_{z_2,\sigma_2}(z')dz'.$$

The maximum total probability, $maxP$, occurs when $z_1 = z_2$.

We limit these two galaxies so that they must have z_1 and z_2 separated by less than $(\sigma_1 + \sigma_2)$. Based on this qualification of friendship, the extreme case is when z_2 is $\sigma_1 + \sigma_2$ apart from z_1. It is worth noting that the total probability is immaterial as the friendship guideline, for the reason that this total probability depends on the standard deviation of the photometric redshift probability density. Here, we give an example. Assuming that the photometric redshift probability density for galaxy A, B, C are $P_A(z_A, \sigma_A) =$

$P_A(0.40, 0.06)$, $P_B(z_B, \sigma_B) = P_B(0.56, 0.10)$, and $P_C(z_C, \sigma_C) = P_C(0.30, 0.04)$. Galaxy B and galaxy C have their photometric redshift separated from galaxy A's by $\sigma_A + \sigma_B$ and $\sigma_A + \sigma_C$, respectively. The total probability for galaxy B and C to have the identical redshift as galaxy A is $P(P_A, P_B) = 0.13$ and $P(P_A, P_C) = 0.21$. Therefore, to decide whether two galaxies have the potential to be in a group, instead of using a single total probability criterion, we normalize it by $maxP$ as

$$P_{ratio} = \frac{\int P_A P_B dz}{maxP},$$

where $maxP$ is the total probability when $z_2 = z_1$. This P_{ratio} ranges from ~ 0.37 for two Gaussian probability densities of $\sigma_1 = \sigma_2$ and $|z_2 - z_1| = \sigma_1 + \sigma_2$, to ~ 0.50 when one of the σ is small relative to the other. Accordingly, the P_{ratio} between galaxy A and galaxy B is $P_{ratio}(P_A, P_B) = 0.39$ and $P_{ratio}(P_A, P_C) = 0.40$ for galaxy A and galaxy C in our demonstration. We set a criterion, $P_{ratio,crit}$, as the friendship criterion in redshift. For any galaxies to be joined together, they must have their $P_{ratio} \geq P_{ratio,crit}$.

2.5 The Probability Friends-of-Friends Algorithm

2.5.1 The Algorithm

The main idea of our group-finding algorithm is to narrow down the photometric redshift uncertainty of a group by way of joining new galaxy members, because the group redshift is the common redshift shared by all the members in the same group. The algorithm starts with a seed galaxy, and treats every galaxy in the sample as a seed. Steps to form a groups are as follows.

Step 1: The seed galaxy

- A 2D co-moving linking length is calculated based on this seed galaxy's photometric redshift and completeness weight (Equation 2.3).
- The seed galaxy executes a transverse search for any other galaxies closer than this linking length.
- Among those galaxies encircled by the linking length, a galaxy is chosen as the seed's companion which have the maximum P_{ratio} relative to the seed galaxy and satisfies the condition $P_{ratio} \geq P_{ratio,crit}$.

Step 2: The proto-group

- The seed and its companion form a proto-group.
- calculate the normalized photometric redshift probability density for the proto-

group as $P_{group}(z) = P_{seed}(z)P_{companion}(z)/\int P_{seed}(z')P_{companion}(z')dz'$.

• assign the peak of $P_{group}(z)$ as the redshift of this proto-group.

• Re-calculate the linking length and absolute magnitudes for these two galaxies based on the assigned proto-group redshift.

• Re-verify the membership of the companion:

(1) using the updated linking length to check whether the companion is still enclosed by the linking length;

(2) the companion still has the maximum P_{ratio} with respect to the seed; and

(3) the revised absolute magnitudes for both the seed and the companion should satisfy the sample $M^{k,e}_{R_c,cut}$ criterion.

• A proto-group is confirmed when the fellowship is established.

Step 3: The primary group

• examine other galaxies located within the linking length to the seed galaxy using the redshift and linking length based on the proto-group.

• From these remaining galaxies, a new member is chosen which satisfy the $P_{ratio} \geq P_{ratio,crit}$ condition, and also have the highest P_{ratio} to the group photometric redshift probability density.

• Re-calculate the group photometric redshift probability density and the linking length with the new member included.

• Re-compute the absolute magnitude of each linked galaxy using the updated group redshift.

• Re-check the membership of all connected galaxies by the $D0$ and $M^{k,e}_{R_c,cut}$ criteria.

• Repeat the procedure until all galaxies enclosed by the seed galaxy's linking length have been examined. A primary group is formed.

Step 4: The friends-of-friends

• A new member is chosen using a procedure similar to Step 1 in choosing the companion, but applied to galaxies within the linking length of any members in this primary group.

• Iterate the process until there is no more additional galaxies linked or rejected.

• A 'mini-group' is formed. The prefix 'mini-' refers to the group associated with each seed galaxy.

Step 5: The mini-groups

• Move to the next seed galaxy and carry out Step 1-4.

• Each galaxy in our sample is considered as a seed galaxy, hence each galaxy has its

own mini-group.

Step 6: Unifying mini-groups

The procedure of unifying mini-groups is necessary because a galaxy can belong to one group *only* . The unifying principles are similar to those used to form mini-groups; that is, mini-groups must have some common members and satisfy a $P_{ratio,crit}$ threshold in order for them to merge into a more massive group. We check this by examining the P_{ratio} criteria of a mini-group with respect to other mini-groups whose seeds are the members of the said mini-group. Terminologically, we refer to the mini-group formed using seed galaxy X as 'mini-group X'. We detail the unifying procedure below, assuming galaxy X is a member of mini-group A.

• If the P_{ratio} between mini-group A and mini-group X fails the $P_{ratio,crit}$ criterion, remove galaxy X from mini-group A. Since the removal of any member from mini-group A may fragment this mini-group, the following step is carried out after every member in mini-group A has been examined for the $P_{ratio,crit}$ criterion to mini-group A:

For any original mini-group A's member to still be a valid member in this merging procedure, it must satisfy all of the following criteria:

(1) the mini-group seeded by this member satisfies the $P_{ratio,crit}$ criterion to mini-group A;

(2) this member has at least one other mini-group A's members within the linking length;

(3) this member is still brighter than $M^{k,e}_{R_c,cut}$ at the group redshift.

• As the merging steps move on, mini-group A may start to have some of its members which have been flagged as members in other mini-groups. For instance, mini-group A has $n_1, n_2, n_3, ..., N$ galaxies, of which members n_1, n_2, n_3 have been flagged as 'grp#1' and members n_6, n_7 are already in 'grp#2'. For this situation, the P_{ratio} of each mini-group A's member (i.e., n_i) to every overlapping group (i.e., 'grp#1' and 'grp#2') is calculated. The subsequent classification of mini-group A's members may belong to one of the following cases:

(1) If all mini-group A's members have their P_{ratio} satisfying the $P_{ratio,crit}$ criterion to all overlapping groups, the member lists of mini-group A and the overlapping groups are merged together and all these groups share the same group ID. In other words, mini-group A has a role as being a 'bridge' in connecting these overlapping groups.

(2) If all mini-group A's members have their P_{ratio} satisfying the $P_{ratio,crit}$ criterion to some but not all overlapping groups, merge the member lists of mini-group A and those

successful ones, and remove any mini-group A's members from those failed overlapping groups. A subsequent examination in transverse space for the membership of those failed overlapping groups is performed, in case that the membership of some members in these failed overlapping groups become invalid due to the removal of the overlapping members.

(3) If all mini-group A's members have their P_{ratio} failed the $P_{ratio,crit}$ criterion to all overlapping groups, the member list of mini-group A is delisted and all its members are classified into other overlapping groups. This re-classification only takes place for those members which have not been associated with any overlapping groups. They are classified into the overlapping groups of the best P_{ratio}. If a mini-group A's member has been flagged as 'grp#1', this galaxy stays in 'grp#1', even though it may have a better P_{ratio} to 'grp#2'.

- After every mini-group has been examined, a final group catalog is established.

2.5.2 Discussion

We call our group-finding algorithm as *'Probability Friends-of-Friends' (pFOF)* for using the characteristics of group redshift probability density and FOF 2D linking. The main feature in our group finding procedure is the dynamic linking. The group redshift probability density and the linking length keep being refined through the entire process and used to re-check all connected galaxies in this group. Some interesting points are:

(a) the normalized group redshift probability density is reconstructed every time when a galaxy joins to or is rejected from this group as

$$P_{group}(z) = P_1(z)P_2(z)...P_n(z).$$

(b) The use of the above group redshift probability density in calculating P_{ratio} for a new galaxy can be interpreted as the probability for this new galaxy to be in this group given N members at the same redshift.

(c) The absolute magnitude of the connected members are re-computed, and the members are re-checked using the updated linking length every time when any galaxy is connected or rejected.

(d) A single galaxy is considered as a group as well. In subsequent analysis, we set a minimum of five galaxies in a group to exclude groups with too few galaxies, so that group redshift can be well confined by its members.

One different approach to applying this 'photometric redshift probability density' idea in group finding using photometric redshift in place of mini-groups and the unifying

procedure, is to continue Step 4 until no more new members are linked. However, we notice that this alternative group finding procedure may break a massive group (usually, a galaxy cluster) into several pieces in redshift space, especially in the region where galaxy numbers are extremely dense such as the core of a cluster. This happens because the formation of a massive galaxy aggregation has confined the group redshift within narrow probability density, and gives no flexibility for other galaxies of different photometric redshifts to join in. These 'other galaxies' are usually the outliers in the comparison of photometric redshift and spectroscopic redshift for individual galaxies. The idea of unifying mini-groups reduces the degrees of splitting massive galaxy aggregations but this still cannot be absolutely avoided unless higher accuracy photometric redshift measurements are available.

In carrying out the group finding, we sort the sample galaxies by their peak values of photometric redshift probability density, so that the group-finding algorithm starts with galaxies in the best photometric redshift measurements. The effect of sorting the catalog on the performance of the algorithm will be discussed in § 2.7.

2.6 The pFOF Group Properties

2.6.1 Group richness

We use N_{gz} to denote the number of linked galaxies. The group richness, N_{gal}, is indicated by the total weights of completeness w_i for galaxies in the group with background galaxy counts subtracted:

$$N_{gal} = R_w \sum_{i}^{N_{gz}} w_i - A_{grp}\Sigma_{grp,bg},$$

where A_{grp} is the group area and $\Sigma_{grp,bg}$ is the contaminating background galaxy surface density within the group. The estimations of A_{grp} and $\Sigma_{grp,bg}$ are presented in the following two subsections. In other words, N_{gal} is the net number of members in a pFOF group. We select pFOF groups which contain at least five physically linked galaxies (i.e., $N_{gz} \geq 5$) so that the group redshift can be well restricted by the members.

2.6.2 Background galaxy density in galaxy groups

The background galaxy density is estimated from the complete photometric redshift catalogs; in our case, the RCS1 CFHT patches (Hsieh et al. 2005). We apply the same cutoffs both in magnitude and photometric redshift as our galaxy sample selection. The

completeness weight for each galaxy is considered as well. We then calculate the number of background galaxies per Mpc^2 at each photometric redshift (in bins of 0.01), and express it as $\Sigma_{bg}(z)$. This $\Sigma_{bg}(z)$ has taken the scaling factor R_w (Equation 2.2) into consideration.

We note that a group redshift can be well confined to $\Delta z_{grp} < 0.02$ by its members, but the dispersion of these members' photometric redshifts may be as large as $\sigma_{z_{phot}} \sim 0.05$. Therefore, to estimate the background galaxy contamination for a galaxy group, we should consider the photometric redshift space within which all members of a group may occur, i.e., the likelihood. Accordingly, we sum the photometric redshift probability densities of all members and normalize the peak of this summed photometric redshift distribution to unity, denoted as $L(z)$. The background galaxy density for this group is estimated using this photometric redshift likelihood as

$$\Sigma_{grp,bg} = \int L(z)\Sigma_{bg}(z)dz.$$

This summed photometric redshift likelihood has broader wings and a wider width than the group redshift probability density. If the later one is used instead, the estimation of $\Sigma_{grp,bg}$ is underestimated. This is because the summed probability density signifies the redshift that a galaxy in a group could have if we drew it from that group.

2.6.3 Projected group area

Geometrically, the mean separation among N galaxies uniformly distributed over an area A is

$$< s >= \sqrt{A/N}.$$

If we assign each galaxy a circular area of radius r, we should expect the total area of these circles centered at individual galaxies to be the same as the total area A, i.e.:

$$N\pi(k < s >)^2 = A,$$

where $r = k < s >$. Consequently,

$$k = \frac{1}{< s >}\sqrt{A/N} = \frac{1}{\sqrt{\pi}}.$$

We calculate the projected group area using an empirical method. Each member in a group is assigned a radius $r =< s > /\sqrt{\pi}$, where $< s >$ is computed as $1/\sqrt{\Sigma_{grp,bg}}$. We then draw a rectangular box of the area A_{reg} with the length and width enclosing the

R.A. and Dec. range of the circles centered at each group member. N random uniformly distributed points are casted over this rectangular box. By counting the numbers (N_{in}) of these N points within the distance r to any group member, the projected group area is computed as

$$A'_{grp} = \frac{N_{in}}{N} A_{reg}.$$

Consequently, the estimated background galaxy number in a pFOF group is calculated as $N'_{bg} = A'_{grp}\Sigma_{grp,bg}$. However, since galaxies are not distributed uniformly, this background estimation must be considered as a lower limit. Tests performed on mock catalogs (see §2.7) allow us to cross-check the true and estimated contaminating background galaxy counts within a galaxy group. We find that the estimated background galaxy number in a pFOF group has a correlation with the actual contaminating mock galaxies but not of a unity slope. This is due to the fact that galaxies are clustered, and hence are not uniformly distributed; so we apply an empirical correction to the projected group area estimated from the above method. The projected group area A_{grp}, in practice, is computed as

$$A_{grp} = 1.634\frac{N_{in}}{N} A_{reg} - \frac{2.505}{\Sigma_{grp,bg}}. \tag{2.4}$$

We note that the empirical correction is similar (within 10%) for a variety of linking criteria and sample selections.

2.7 Testing pFOF Algorithm on Mock Catalogs

2.7.1 Mock Catalogs

We test our algorithm using mock catalogs so that we can establish the performance of our group finding algorithm. The mock catalogs are constructed from the Virgo Consortium Millennium Simulation Springel et al. (2005) using semi-analytical modeling of galaxy evolution by Croton et al. (2006), kindly provided by Darren Croton. Groups in the simulation are identified by a FOF group-finder with a linking length of 0.2 of the mean particle separation (Croton et al. 2006), and a central galaxy is identified within each FOF halo using the minimum in the gravitational potential in the group. We prune off those FOF haloes which contain only one or two galaxies, and define galaxies in these poor FOF haloes as field galaxies.

Our mock catalogs contain $\sim 800,000$ galaxies with BRI magnitudes with $R_{AB} < 26.0$ and redshifts extending from 0 to 1.4 in a total of 5.0 square degrees of sky area from

five cones. For the purpose of testing our algorithm, we convert the photometry in the mock catalogs to the Vega system, and set a cutoff in the R_c-filter apparent magnitude as $m_{R_c} < 22.5$ to mimic a flux limited sample. With this apparent magnitude cutoff, the sample become incomplete to $M^{k,e}_{R_c,cut} = M^*_{R_c} + 2.0$ at $z_{cut} = 0.412$. To simulate photometric redshift for the total of 177,344 galaxies in our mock sample, we take the following steps.

• We bin the training set galaxies based on their spectroscopic redshift using a bin size of 0.05. In each spectroscopic redshift bin, we make the photometric-redshift histogram of the training set galaxies using a bin size of 0.01. The photometric-redshift distribution function is accordingly the photometric-redshift histogram normalized with unity area underneath.

• This photometric-redshift distribution function is then used to draw a photometric redshift for each galaxy in the mock sample in the corresponding redshift bin, so that any offset between photometric and spectroscopic redshifts in the real observational samples can be mimicked. The use of the photometric-redshift distribution function derived from the real samples also ensures that the dispersion between the simulated photometric and true redshifts increases toward higher redshifts.

• Each galaxy in the mock sample is then tagged with a photometric redshift probability density centered at its simulated photometric redshift. The tagged photometric redshift probability density is based on that associated with a training set galaxy of similar color and magnitude. This enables us to obtain reasonable photometric redshift probability densities depending on galaxy color and magnitude, and the distributions of photometric redshift uncertainties for galaxies in the mock sample are similar to those of our training set galaxies.

The dispersion between the simulated photometric redshift and actual galaxy redshift for galaxies in the mock sample is ~ 0.061 at $0.3 \leq z_{mock} < 0.6$, and ~ 0.122 at $0.6 \leq z_{mock} < 0.9$ (compared to 0.060 and 0.134 in our real data set).

After the simulated photometric redshifts are obtained, we compute the completeness factor w_i for each galaxy satisfying the selection. We find that $w_i \sim 1.286$ at $m_{R_c} = 22.5$. We also select galaxies in the mock catalogs brighter than $M^*_{R_c} + 2$ after applying approximate proper k- and evolution corrections. A total of 72,954 galaxies are in our final selected mock sample, and the median w_i is ~ 1.091. We refer to this simulated photometric redshift sample resembling our real data from the RCS as the '$z_{simulated}$' sample.

2.7.2 Test Results

We apply our pFOF group-finding algorithm to the mock photometric redshift sample with fiducial $P_{ratio,crit} = 0.37$ and $D0_{xy} = 0.25$ Mpc. The properties of galaxy groups are quantified as described in § 2.6. We use the mock photometric redshift sample itself as the control field for background subtraction.

Contaminating Background Galaxies

Background galaxy contamination correction is essential for any work using photometric redshifts. The photometric redshift technique can be an effective tool in scientific analysis, if the estimated and true background galaxy contamination are comparable to each other. For each pFOF group, we have estimated the numbers of background galaxies as described in § 2.6, noted as $N'_{bg} = A'_{grp}\Sigma_{grp,bg}$. In the use of mock catalogs, we can count the actual contaminating galaxies; i.e., $N_{bg,actual}$, galaxies contributed by the field, or other haloes, or both. By comparing N'_{bg} and $N_{bg,actual}$ in each true pFOF group, we find that N'_{bg} tends to be underestimated when $N_{bg,actual}$ is large and the trend can be approximated using a linear relation as $N_{bg,actual} = 1.634 \times N'_{bg} - 2.505$ (Fig. 2.4). We therefore apply the linear relation to correct the N'_{bg} by adjusting the group area A'_{grp} (Eq. 2.4). We use N_{bg} to denote the number of the estimated background galaxies with the linear correction applied.

Test 1: the Recovery Rate

To test the performance of our pFOF algorithm, we investigate the group recovery rate of the mock sample. We apply our pFOF group-finding algorithm to the mock $z_{simulated}$ sample with $P_{ratio,crit} = 0.37$ and $D0_{xy} = 0.25$ Mpc. The mock groups which have at least three members brighter than our sample magnitude cutoffs (i.e., $m_{R_c} < 22.5$ and $M^{k,e}_{R_c} < M^*_{R_c} + 2.0$) are selected as the reference groups. We have a total of 705 reference groups at $z < z_{cut}$. We use the following matching procedure. Since every galaxy has a pFOF group ID in the output files of the pFOF algorithm, we classify each member of a mock reference group by its pFOF group ID. The members of a mock group may belong to different pFOF groups. We define the matched pFOF group as the one that contains the maximum number of mock group members and satisfy $N_{gal} \geq 3$ and $N_{gz} \geq 5$ (see § 2.6). Each pFOF group is allowed to match only one reference mock group. If there is more than one reference mock group recovered by the same pFOF group, only one of these reference mock groups is classified as 'recovered'. The recovery results of the mock

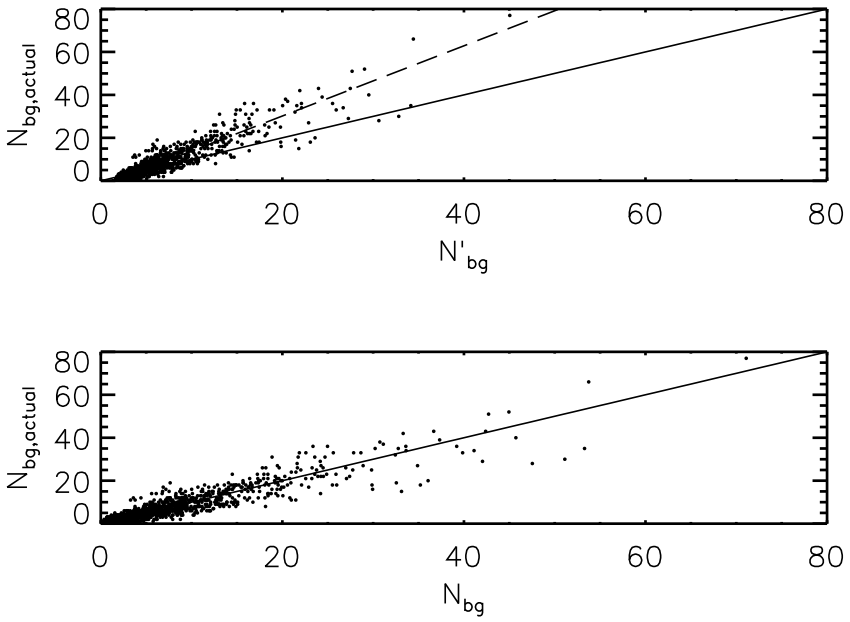

Figure 2.4: The *Top* plot is the comparison between the estimated (N'_{bg}) and the actual ($N_{bg,actual}$) contaminating background galaxy counts in each pFOF group. The N'_{bg} tends to be underestimated. The solid line is of unity slope and the dashed one is the linear correlation between N'_{bg} and $N_{bg,actual}$. The results after applying the linear solution to N'_{bg} is presented in the *Bottom* plot.

groups are presented in Fig. 2.5. The Y-axis in Fig. 2.5 is the fraction of the recovered to the total reference mock groups of halo mass greater than a cutoff (i.e., the X-axis). The recovery rate increases when the halo mass is larger. The pFOF algorithm recovers more than 80% reference mock groups of halo mass greater than $\sim 1.2 \times 10^{13} M_{\odot}$, and recovers all mock groups of halo mass greater than $\sim 3.4 \times 10^{13} M_{\odot}$. The r.m.s. dispersion in redshift between the recovered reference mock groups and the matched pFOF groups is ~ 0.052 and ~ 0.038 for the reference groups of halo mass greater than $\sim 1.2 \times 10^{13} M_{\odot}$ and $\sim 3.4 \times 10^{13} M_{\odot}$, respectively.

Test 2: the fraction of false detected pFOF groups

To investigate the fraction of falsely detected pFOF groups, we examine every member of a pFOF group to see in which mock haloes they are located. With $P_{ratio,crit} = 0.37$ and $D0_{xy} = 0.25$, we have 1,019 pFOF groups in total as the reference, selected with $N_{gal} \geq 3$, $N_{gz} \geq 5$, and $z_{pFOF} < z_{cut}$. A reference pFOF group is flagged as 'false detection' if either

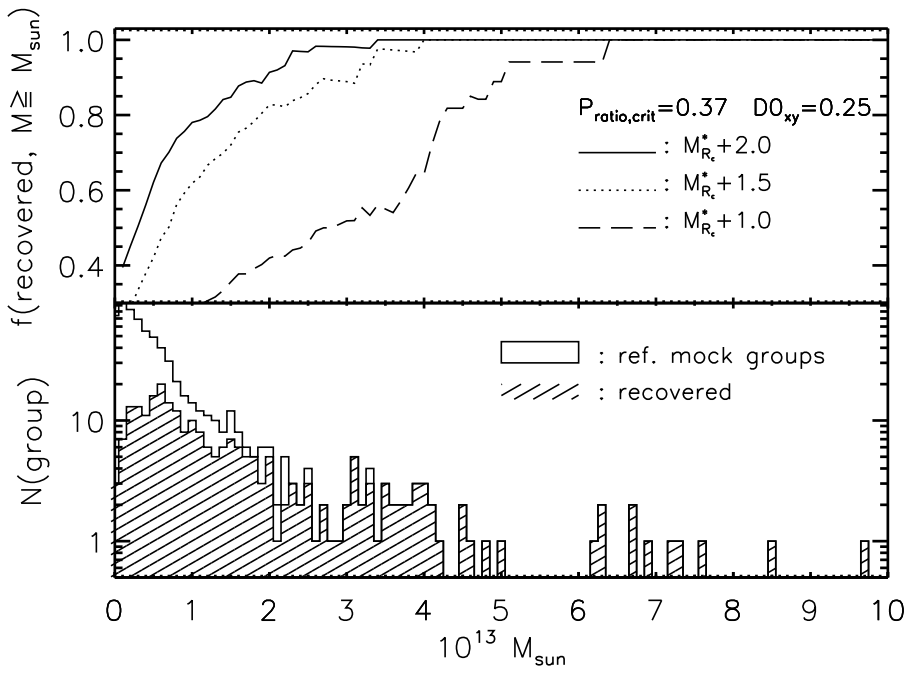

Figure 2.5: The results of Test 1 using pFOF groups formed with $P_{ratio,crit} = 0.37$ and $D0_{xy} = 0.25$ Mpc. The recovery rates as a function of mock group halo mass are shown in the top panel. The dashed, dotted, and solid curves are the results using sample with $M^*_{R_c} + 1.0$, $M^*_{R_c} + 1.5$, and $M^*_{R_c} + 2.0$ cutoffs, respectively. The distribution of reference mock group halo mass with the $M^*_{R_c} + 2.0$ cutoff are shown as the un-hatched histograms in the bottom panel, while the hatched histogram represents the richness distribution of the recovered reference groups.

(1) all its members are composed of field galaxies (the galaxies in poor FOF haloes containing fewer than three galaxies in the simulations), or

(2) it contains fewer than three members from a mock group.

We present the results in Fig. 2.6. The Y-axis is the fractions of false detected to the total pFOF groups with N_{gal} greater than a cutoff in X-axis. The fraction of false detected groups decreases when the reference pFOF groups are of larger N_{gal}. The false detection rate is $\sim 30\%$ for pFOF groups of $N_{gal} \geq 5.85$, and is $\sim 10\%$ when $N_{gal} \geq 7.91$. A pFOF group of $N_{gal} \sim 8$ corresponds to a halo mass $\sim 3.7 \times 10^{13} M_{\odot}$.

Test 3: the effect of magnitude limit

To test how sample depth affects the pFOF performance, we repeat Test 1 and Test 2 but with two additional different $M^{k,e}_{R_c,cut}$ cutoffs: $M^{k,e}_{R_c,cut} = M^*_{R_c}+1.0$ and $M^{k,e}_{R_c,cut} = M^*_{R_c}+1.5$.

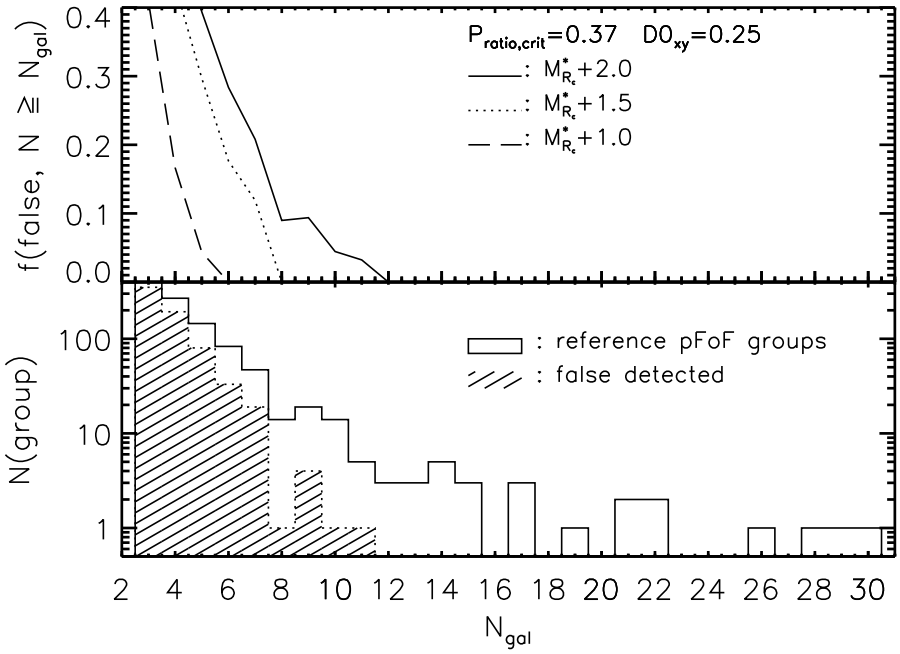

Figure 2.6: *Top:* The fractions of false detected pFOF groups as a function of group richness for the sample of depth to $M^*_{R_c}+1.0$ (dashed), $M^*_{R_c}+1.5$ (dotted), and $M^*_{R_c}+2.0$ (solid), respectively. *Bottom:* The unhatched histogram is the richness distribution for the reference pFOF groups with sample depth as $M^*_{R_c}+2.0$. The number of false detected pFOF groups are presented as the hatched histogram.

All the reference pFOF groups are selected at $z < z_{cut}$ where $z_{cut} = 0.412$ is the redshift when the sample becomes incomplete to $M^{k,e}_{R_c,cut} = M^*_{R_c} + 2.0$. The results are listed in Table 2.1 and overlaid in Fig. 2.5 and Fig. 2.6 as the dashed and dotted curves along with the results from Test 1 and Test 2.

We observe that there are more reference mock groups recovered when sample depth increases, but the fraction of false detected groups increases as well when $M^{k,e}_{R_c,cut}$ changes from $M^*_{R_c} + 1.0$ to $M^*_{R_c} + 2.0$. Therefore, we conclude that samples with shallow depth miss a large portion of true groups, especially the poorer ones. Going deeper into the luminosity function increases the identification of true galaxy groups with a higher but still acceptable false detection rate. Based on these tests using three $M^{k,e}_{R_c,cut}$ cutoffs, we suggest that a sample should have a depth of at least $M^*_{R_c} + 1.5$ in order to obtain the better group finding results.

Test 4: the linking criteria

One of the critical issues in any group-finding algorithm based on the friends-of-friends algorithm is the choice in the values of linking parameters. As described in § 2.4, $P_{ratio,crit}$ and $D0_{xy}$ are the main linking parameters used in the pFOF algorithm. The role of $P_{ratio,crit}$ is to determine group membership in photometric redshift space, while $D0_{xy}$ is to define the friendship criterion in the transverse direction. To probe how the linking criteria affect pFOF membership, we repeat Tests 1 and 2 but using pFOF groups formed with different $P_{ratio,crit}$ and $D0_{xy}$. The results are listed in Table 2.1 and presented in Fig. 2.7 and Fig. 2.8.

Generally speaking, more reference mock groups in Fig. 2.7 are recovered for a fixed $P_{ratio,crit}$ with a larger $D0_{xy}$, or for a fixed $D0_{xy}$ with a smaller $P_{ratio,crit}$. However, the recovery rate may decrease for some situations when smaller P_{ratio} and large $D0_{xy}$ are used. This is because galaxies are linked easily into pFOF groups for such sets of $P_{ratio,crit}$ and $D0_{xy}$, and large fractions of pFOF groups fail to satisfy the N_{gal} richness selection after the background subtraction.

To examine the fraction of pFOF groups which contain multiple mock groups, we flag pFOF groups as 'serious projection' if two or more mock groups contribute similar numbers of galaxies to the pFOF members. Using N_1 and N_2 to denote the numbers of galaxies in a pFOF group from mock group #1 and #2. Assuming $N_1 \geq N_2$, this pFOF will be flagged as 'serious projection' if $N_1/N_2 < 1.5$. The results, together with the false detection rates, are listed in Table 2.1 and presented in Fig. 2.8 and Fig. 2.9.

With a fixed $P_{ratio,crit}$ in Fig. 2.8, the false detection rates increase when a larger $D0_{xy}$ is used in general. For the same $P_{ratio,crit}$, the fractions of 'serious projection' tend to increase using larger $D0_{xy}$, with the exception of $D0_{xy}$=0.15Mpc. Using a certain $D0_{xy}$ (Fig. 2.9), the false detection rates increase when a lower $P_{ratio,crit}$ is used. The fractions of 'serious projection' increase as well when the $P_{ratio,crit}$ is lower with a fixed $D0_{xy}$, except for $D0_{xy}$=0.30Mpc.

In summary, the tests of different linking criteria show that there is a dynamic relation between $P_{ratio,crit}$ and $D0_{xy}$. The use of larger linking length, while providing a better recovery rate, tends to form more groups which are not truly physically related. This higher recovery rate and larger fractions of false detections and projections are also applicable to small $P_{ratio,crit}$. Therefore, a set of $P_{ratio,crit}$ and $D0_{xy}$ should be chosen which is a compromise between the recovery and false detection rates. We adopt $P_{ratio,crit} = 0.37$ and $D0_{xy}$=0.25 Mpc for further tests of our algorithm.

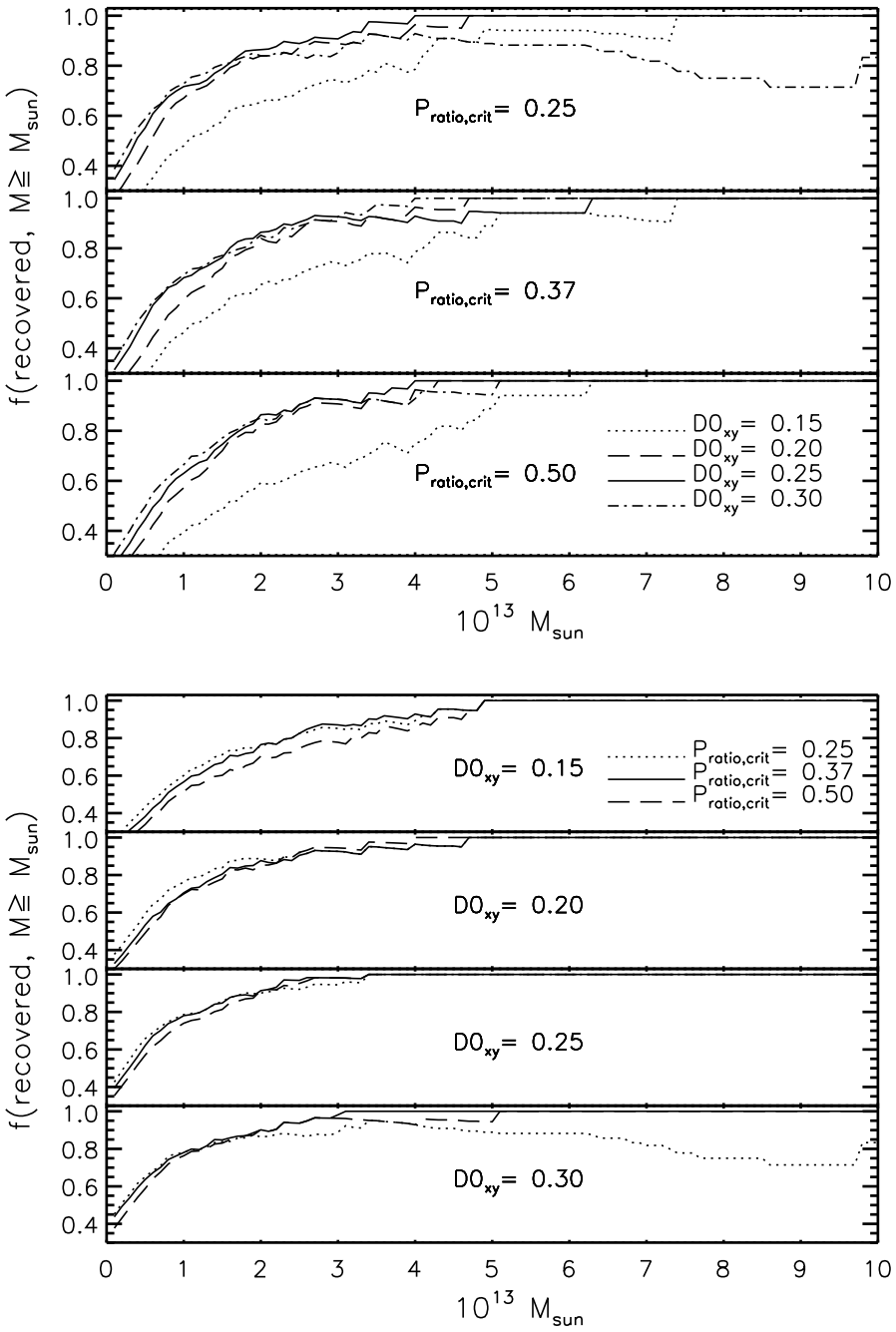

Figure 2.7: The repeated Test 1 results (recovery rate) using pFOF groups formed with different $P_{ratio,crit}$ and $D0_{xy}$ as indicated in the plots. *Top:* The results using various $D0_{xy}$ with a fixed $P_{ratio,crit}$. *Bottom:* The recovery rate using different $P_{ratio,crit}$ with a certain $D0_{xy}$.

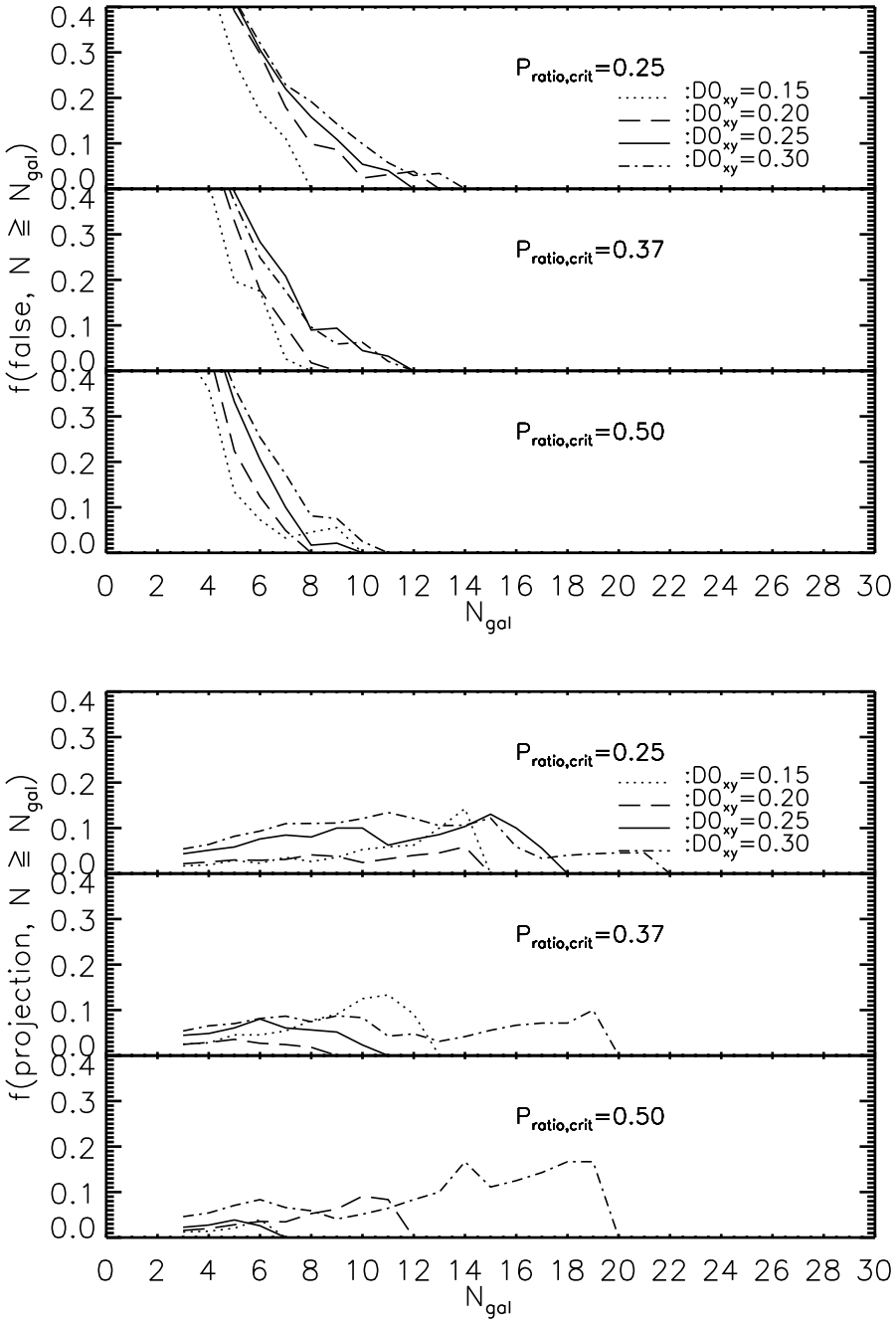

Figure 2.8: *Top:* The repeated Test 2 results (false detection rate) using various $D0_{xy}$ with a fixed $P_{ratio,crit}$. *Bottom:* The fractions of pFOF groups containing members from multiple mock groups ('serious projection') using different $D0_{xy}$ and a certain $P_{ratio,crit}$. The false detection rates and fractions of 'serious projection' increases when $D0_{xy}$ is larger.

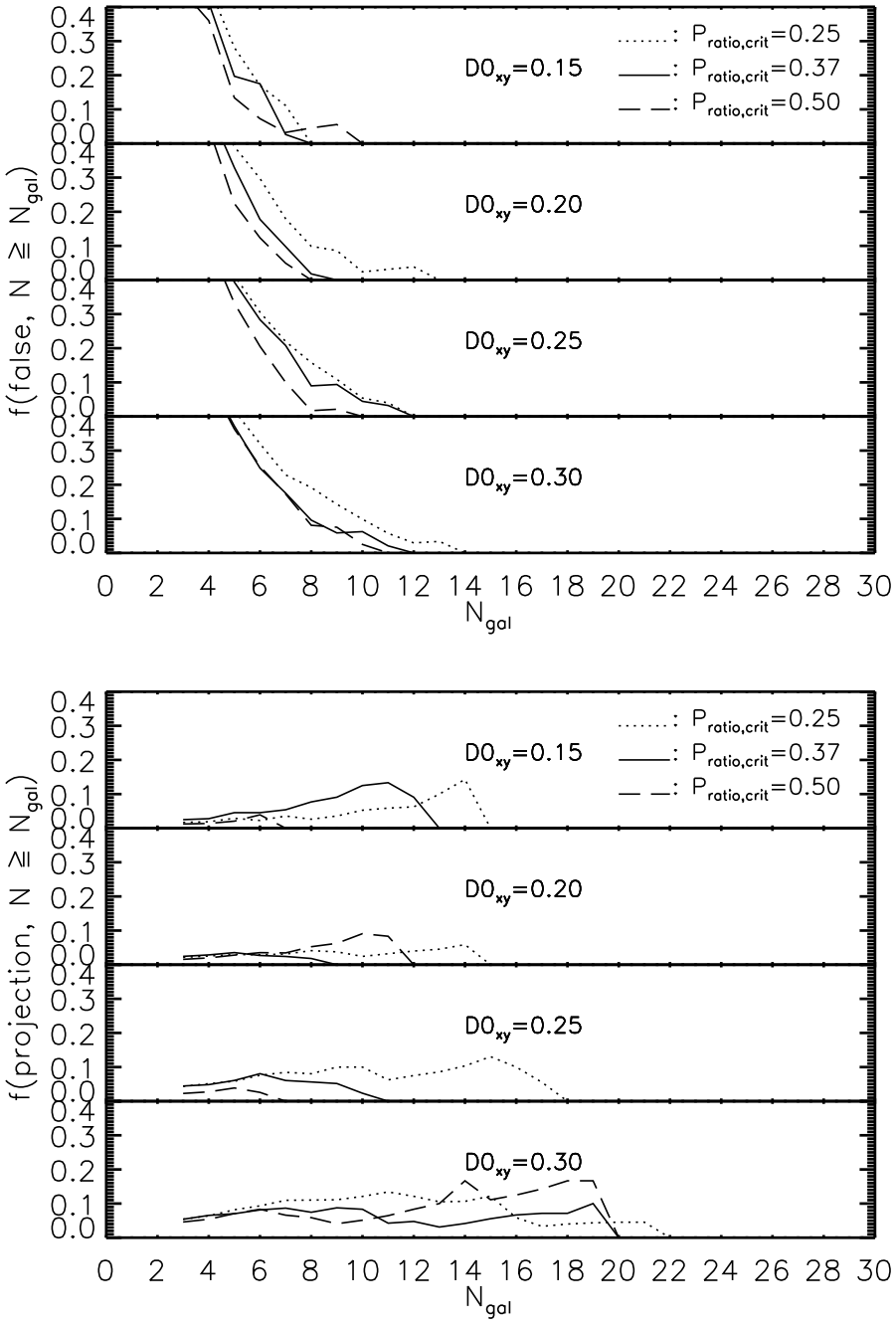

Figure 2.9: Same as Fig. 2.8 but plotted in a fixed $D0_{xy}$ with different $P_{ratio,crit}$.

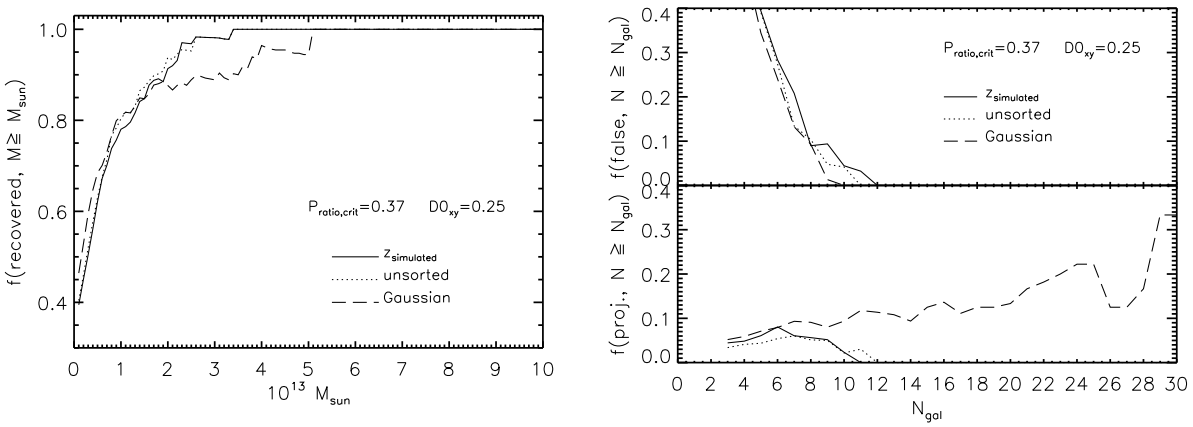

Figure 2.10: *Left:* The repeated Test 1 results (recovery rate) using the '$z_{simulated}$', 'unsorted', and 'Gaussian' samples (see Test 5 and Test 6 in §2.7). *Right:* The false detection rates and fractions of the pFOF groups flagged as 'serious projection' using those three samples in the *Left* plot.

Test 5: the order of seeding galaxies

To discuss how the order of seed galaxies affects the group finding results, we perform the same group finding code, but the input catalogs are randomly ordered by the object IDs. We remind the reader that the input catalogs (the '$z_{simulated}$' sample) in Test 1 and Test 2 are sorted by the peak value of each galaxy's photometric redshift probability density. Thereupon, we use 'unsorted' and 'sorted' catalogs in short to refer to these two types of input catalogs. These two types of catalogs contain identical galaxies and properties, but differs only in the galaxy order in the catalogs. Both Test 1 and Test 2 are conducted again using 'non-sorted' catalogs with the same linking criteria, $P_{ratio,crit}$=0.37 and $D0_{xy} = 0.25$ Mpc.

The results, presented as the dotted curves in Fig. 2.10, show a similar recovery rate and a also similar fractions of false detected and 'serious projected' groups, compared to those using the 'sorted' sample (solid curves). Note that our pFOF algorithm takes the steps of forming 'mini-groups'. The role of galaxy orders mainly lies in the steps of unifying 'mini-groups', where the existing 'mini-groups' (or merged ones) are used to combine with more 'mini-groups' with lower ranks. We decide to sort our catalogs by the peak values of photometric redshift probability of individual galaxies, so that each final group grows from the 'mini-groups' of seed galaxies with the best quality.

Test 6: Gaussian probability densities

We are also interested in how the group membership changes if we assume Gaussian photometric redshift probability densities. To do this, we take each galaxy's photometric redshift and error as the mean and standard deviation of a Gaussian distribution to generate a Gaussian photometric redshift probability. We call these catalogs 'Gaussian', and refer to those catalogs using real photometric redshift probability densities ('$z_{simulated}$' sample) as 'non-Gaussian'. The completeness correction weight w_i is accordingly calculated for the 'Gaussian' sample. The w_i is ~ 1.074 at m_{R_c}=22.5, and the averaged w_i is ~ 1.025. Galaxies in both the 'Gaussian' and 'non-Gaussian' samples are sorted by the peak values of their photometric redshift probability densities. The estimated background counts are re-computed using the 'Gaussian' sample, which are similar to what are estimated using the 'non-Gaussian' sample.

The results are illustrated as the dashed curves in Fig. 2.10. Compared to the Test 1 results of using the '$z_{simulated}$' sample (the solid curves), the 'Gaussian' sample recovers more mock groups of halo mass less than $1.3 \times 10^{13} M_{\odot}$ but it fails to recover as many mock groups of halo mass richer than $1.3 \sim 5.0 \times 10^{13} M_{\odot}$ as using the '$z_{simulated}$' sample. From the results of false detection rate and tests of 'serious projection', the 'Gaussian' sample has a smaller fraction of false detected pFOF groups but $\sim 13\%$ of true groups are flagged as 'serious projection'. Gaussian photometric redshift probability density is the simplest assumption in dealing with photometric redshift uncertainties in group finding. The results of Fig. 2.10 using 'Gaussian' and 'non-Gaussian' ('$z_{simulated}$') samples suggest that the asymmetric shape of galaxy's photometric redshift probability density has a role in determining group membership.

Test 7: the accuracy of photometric redshift measurements

To explore the performance of the pFOF algorithm when the accuracy in photometric redshift measurements changes, we re-construct the simulated photometric redshift sample, and then repeat Test 1 and Test 2. We take the same steps in § 2.7.1 in generating photometric redshifts and probability densities, but scale the dispersion between the simulated photometric redshift and mock galaxy redshift by a factor of 0.5. The probability densities are consequently rescaled by the same factor. The overall dispersion between the simulated photometric redshift and actual redshift is ~ 0.037 at $0 \leq z_{mock} < 0.6$ and ~ 0.069 at $0.6 \leq z_{mock} < 0.9$. We apply the same criteria in selecting the sample, and refer to this sample as 'z_{half}'.

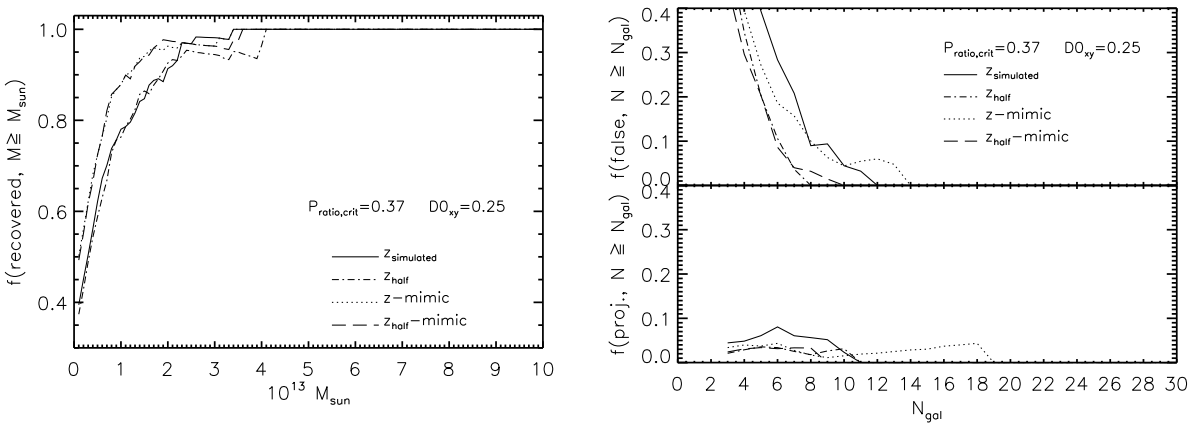

Figure 2.11: *Left:* The repeated Test 1 results using the '$z_{simulated}$', 'z_{half}','z-mimic', and 'z_{half}-mimic' samples (see Test 7 and Test 8 in §2.7). *Right:* The false detection rates and fractions of 'serious projection' using those four samples in the *Left* plot.

The test results using 'z_{half}' are presented in Fig. 2.11 as the dash-dotted curves. The 'z_{half}' sample recovers fewer mock groups of $2 \sim 4 \times 10^{13} M_{\odot}$ halo mass than the result of the '$z_{simulated}$' sample by 4%. However, the 'z_{half}' sample contains a smaller fraction of false detected pFOF groups, $\sim 65\%$ of the result using the '$z_{simulated}$' sample. This test of using the 'z_{half}' sample shows that the recovery rate is not a strong function of photometric redshift accuracy, but the false detection rate is. This illustrates that the group finding robustness depends on the photometric redshift accuracy.

Test 8: the use of accurate redshifts

To examine how photometric redshift accuracy affects the group-finding performance, we repeat Test 1 and Test 2 but using photometric redshift catalogs which the accurately known redshift of each galaxy is assigned as its photometric redshift. We refer to these catalogs as 'z-mimic' catalogs. The photometric redshift probability densities for galaxies in the 'z-mimic' catalogs are created in the same way as the '$z_{simulated}$' sample described in § 2.7.1. That is, the photometric redshift probability density of each galaxy resembles the real data, even though its true redshift has been assigned as its photometric redshift. The same sample selecting criteria and the pFOF codes are applied to these 'z-mimic' catalogs.

To test how the uncertainty in photometric redshift affects the group finding results, we also re-construct the 'z-mimic' catalogs but scale the probability densities to be twice as accurate (i.e., scale by a factor of 0.5), and refer to these as 'z_{half}-mimic' catalogs.

The same criteria of sample selection and pFOF codes are used.

The test results using the 'z-mimic' and 'z_{half}-mimic' samples are presented in Fig. 2.11 as the dotted and dashed curves. Both the 'z-mimic' and 'z_{half}-mimic' samples have better recovery rate ($> 80\%$ for $7 \times 10^{12} M_{\odot}$) compared to the use of the '$z_{simulated}$' sample ($> 80\%$ for $1.2 \times 10^{13} M_{\odot}$). The Test 2 results using 'z-mimic' and 'z_{half}-mimic' samples show that the false detection rates are $\sim 10\%$ for reference pFOF groups of $N_{gal} \geq 8$ and $N_{gal} \geq 5.88$, respectively. In the meantime, $\sim 2\%$ of pFOF groups of $N_{gal} \geq 8$ in the 'z-mimic' sample are flagged as 'serious projection', but none of the pFOF groups of the same richness in the 'z_{half}-mimic' contains 'serious projection'. This further illustrates that group finding performance strongly relies on the accuracy of photometric redshift measurements, and also on individual galaxies' photometric redshift uncertainties (i.e., the width of a photometric redshift density).

2.7.3 Examples of Recovered Groups

In view of the Test 1-8 results, we conclude that our pFOF group finding algorithm is able to identify galaxy groups using photometric redshift samples, although the performance of group finding results depends on the accuracy of photometric redshift measurements. We summarize our test results using mock samples in Table 2.1. In Fig. 2.13 and 2.14, we present two typical examples of the identified mock and pFOF groups formed using $P_{ratio,crit} = 0.37$ and $D0_{xy} = 0.25$ Mpc. In each figure, we show the sky locations of the mock group members. The members of the pFOF group which matches the mock group galaxies are marked by diamonds. The simulated photometric redshift distribution of members in the mock group and the individual photometric redshift probability density of the matched pFOF group members are presented as well.

2.8 CNOC2 Groups

2.8.1 The Group Samples

We further test our pFOF algorithm by comparing the group finding results to the CNOC2 groups (Carlberg et al. 2001). The published CNOC2 groups catalog were generated using a friends-of-friends algorithm with $r_p^{max} = 0.25 h^{-1} Mpc$ and $r_z^{max} = 5 h^{-1} Mpc$ as the linking parameters in the transverse and radial direction. A total of 192 groups in an area of 1.5 square degrees were identified at a median redshift of 0.33. The groups have

Table 2.1: Mock Test Results

Sample	$P_{ratio,crit}$	$D0^a_{xy}$	$M^{k,e}_{R_c}$	recovery rate[b]	false dection rate[c]	serious projection	note
$z_{simulated}$	0.37	0.25	$M^*+1.0$	31%	0%	8%	sorted, non-Gaussian
$z_{simulated}$	0.37	0.25	$M^*+1.5$	67%	0%	5%	
$z_{simulated}$	0.37	0.25	$M^*+2.0$	80%	9%	5%	
$z_{simulated}$	0.25	0.15	$M^*+2.0$	65%	0%	3%	
$z_{simulated}$	0.25	0.20	$M^*+2.0$	79%	10%	3%	
$z_{simulated}$	0.25	0.25	$M^*+2.0$	80%	16%	8%	
$z_{simulated}$	0.25	0.30	$M^*+2.0$	80%	19%	8%	
$z_{simulated}$	0.37	0.15	$M^*+2.0$	61%	0%	5%	
$z_{simulated}$	0.37	0.20	$M^*+2.0$	73%	2%	2%	
$z_{simulated}$	0.37	0.25	$M^*+2.0$	80%	9%	5%	
$z_{simulated}$	0.37	0.30	$M^*+2.0$	80%	10%	7%	
$z_{simulated}$	0.50	0.15	$M^*+2.0$	55%	5%	1%	
$z_{simulated}$	0.50	0.20	$M^*+2.0$	72%	0%	3%	
$z_{simulated}$	0.50	0.25	$M^*+2.0$	76%	2%	2%	
$z_{simulated}$	0.50	0.30	$M^*+2.0$	79%	8%	7%	
Gaussian	0.37	0.25	$M^*+2.0$	82%	9%	13%	
z_{half}	0.37	0.25	$M^*+2.0$	80%	0%	3%	
z-mimic	0.37	0.25	$M^*+2.0$	90%	10%	3%	
z_{half}-mimic	0.37	0.25	$M^*+2.0$	89%	3%	3%	

[a] in Mpc

[b] for mock groups of $M_{halo} \geq 1.2 \times 10^{13} M_\odot$

[c] for pFOF groups of $N_{gal} \geq 8$

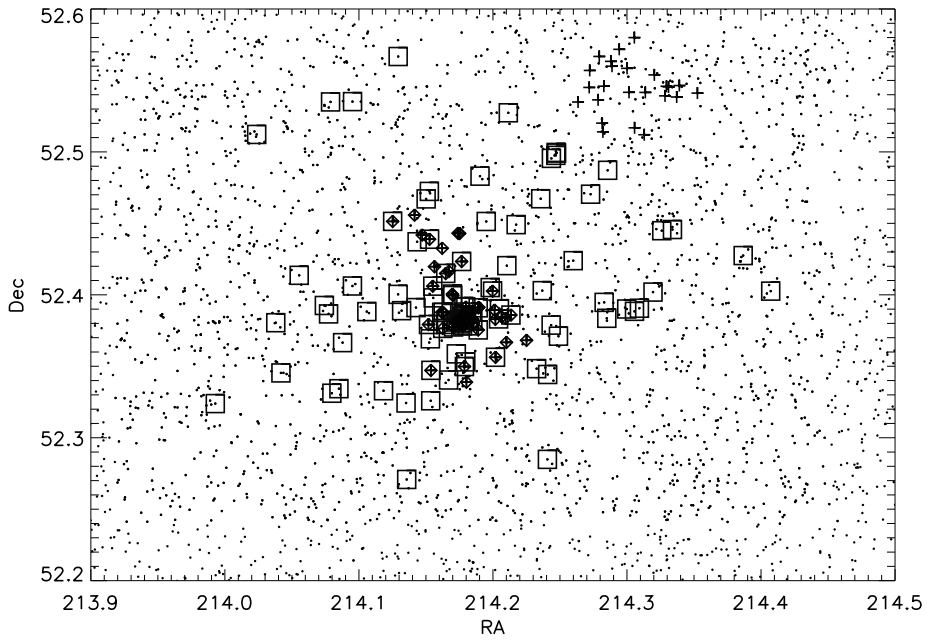

Figure 2.12: The sky map of a rich mock group (z=0.237, $M = 20 \times 10^{13} M_{\odot}$) and the pFOF groups in the same sky region. The solid dots are galaxies in the '$z_{simulated}$' sample. The squares mark the position of each member of the mock group in the sample. The crosses indicate the members of each pFOF groups, selected with $N_{gal} \geq 10$ and $z_{pFOF} < z_{cut}$. The members of the pFOF group which matches the mock group are marked by diamonds. Note that another group (crosses) is completely separated from the mock group.

a median dynamically determined velocity dispersion of 190 km/s. The average number of galaxies identified in each group is ~ 4. The richness of CNOC2 groups is computed as $\eta_{CNOC2} = \sum_i^N (w_{m,i} w_{z,i})$ where $w_{m,i}$ and $w_{z,i}$ are the weights based on the magnitude and redshift selection functions (Yee et al. 2000). As a result, the group richness is ~ 1.74 times greater than the identified group members, i.e., the true average group richness is ~ 7. The four CNOC2 patches coincide with the RCS1 observations (Hsieh et al. 2005), but do not have complete overlap. We apply our pFOF algorithm with $P_{ratio,crit} = 0.37$ and $D0_{xy} = 0.25$ Mpc to the RCS catalogs in the same sky coverage as the CNOC2 patches. The samples are selected as described in § 2.3. Due to the incomplete coverages in the RCS, we have 109 of the published CNOC2 groups in our comparison list. We set a redshift cut as $0.19 \leq z < 0.41$, since the redshift distribution of CNOC2 groups becomes incomplete beyond $z \sim 0.4$ (Carlberg et al. 2001).

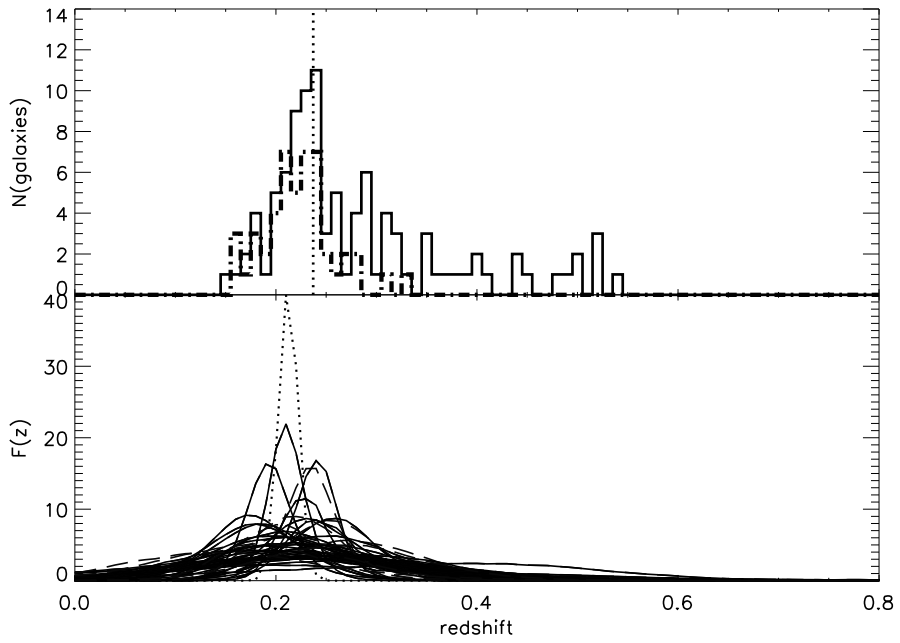

Figure 2.13: *Top:* The histogram (0.01 bin size) of simulated photometric redshift of galaxies in the mock group (solid) and members of the matched pFOF group (dash-dotted). The vertical dotted line indicates the mock group redshift. *Bottom:* The individual photometric redshift probability distributions of the matched pFOF group members (i.e., the group galaxies in diamonds in Fig. 2.12) are plotted as solid curves, and galaxies considered as background galaxies (i.e., galaxies not in this mock group halo) are plotted in dashed curves. The group redshift distribution of this matched pFOF group is plotted as the dotted curve, $z_{pFOF} = 0.217 \pm 0.009$.

2.8.2 The Group Finding Results

We conduct the comparison between CNOC2 and pFOF groups in similar manners as Test 1 and Test 2 in § 2.7.1. First, CNOC2 groups are used as the reference; second, pFOF groups are considered as the reference and used to test the completeness of CNOC2 groups.

(1) Test I: The fraction of recovered CNOC2 groups

To define a pFOF group which recovers a CNOC2 group, we carry out the matching procedure by determining the separation between their group centers. The reference CNOC2 groups are selected at $0.19 \leq z < 0.41$ and with $\eta_{CNOC2}/N < 2.5$. We have 65 reference CNOC2 groups, and 54 of them are from the 0223 and 0920 patches. We define that a matched pFOF group must have its center within 0.25Mpc (the linking length

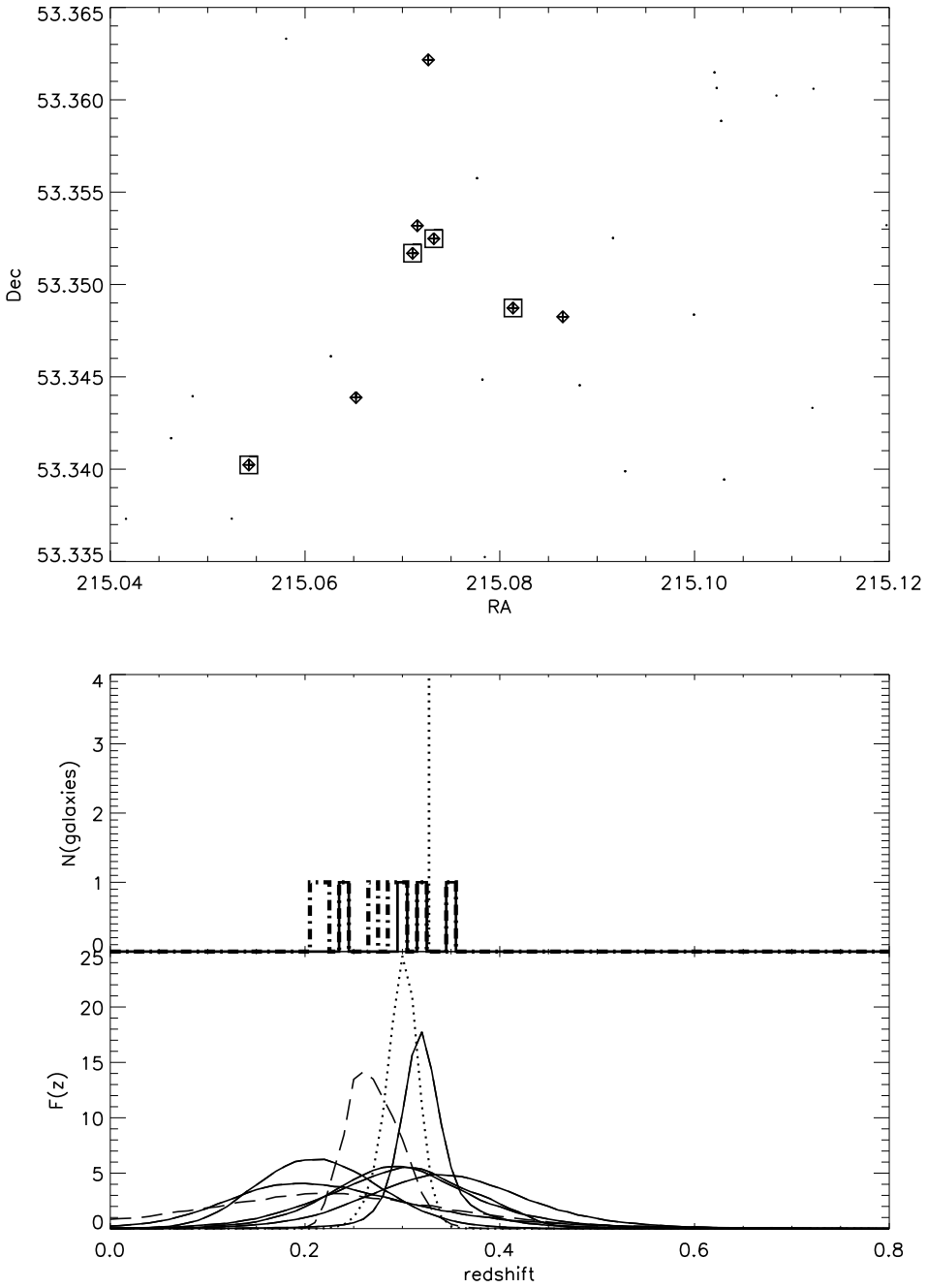

Figure 2.14: same as Fig. 2.13 but for a poorer mock group at z=0.327 and of $1.9 \times 10^{13} M_{\odot}$. The matched pFOF group has the richness of $N_{gal} = 5.46$ at $z_{pFOF} = 0.303 \pm 0.018$.

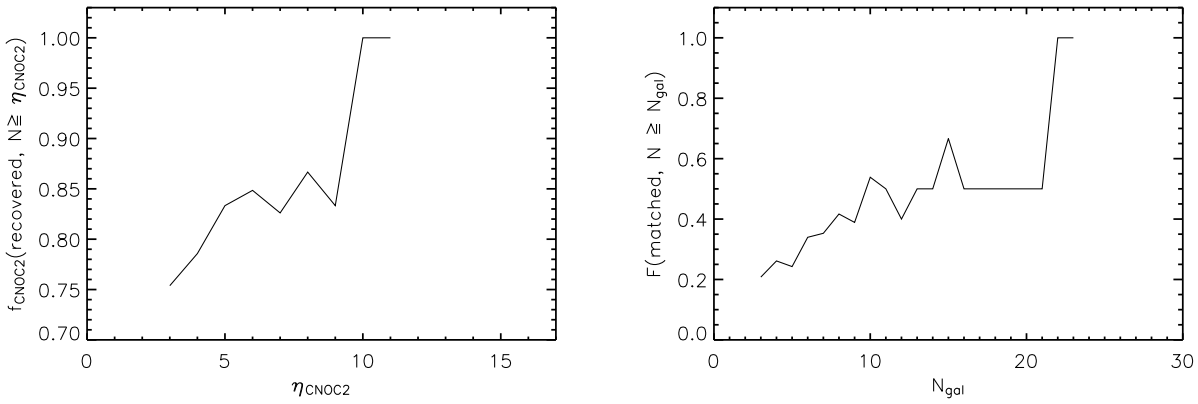

Figure 2.15: *Left:* The recovery rate as a function of CNOC2 group richness η_{CNOC2}. *Right:* The fraction of matched reference pFOF groups to the total. The y-axis can be considered as the sampling rate of CNOC2 group catalogs, *if* we assume there is no false detected pFOF groups.

used in Carlberg et al. 2001) to a CNOC2 group center, and satisfy $N_{gal} \geq 3$.

The recovery rate as a function of CNOC2 group richness η_{CNOC2} is plotted in Fig. 2.15. The recovery rate is $\sim 90\%$ for richness cutoff of $\eta_{CNOC2} \geq 5$. We note that this is similar to those from the mock group tests.

(2) Test II: The completeness rate of CNOC2 groups

To examine the completeness of CNOC2 groups, we compare CNOC2 groups to pFOF groups. The reference pFOF groups are selected to be at $0.19 \leq z < 0.41$ with $N_{gal} \geq 3$. We have 231 pFOF groups satisfying these conditions using $P_{ratio,crit} = 0.37$ and $D0_{xy} = 0.25$ Mpc. The matching process is carried out by identifying CNOC2 groups which the separations of their centers to the reference pFOF group centers are less then 0.25Mpc. For the purpose of estimating the sampling rate of CNOC2 groups, we plot in Fig. 2.15 the ratio of matched reference pFOF groups to the total as a function of group richness N_{gal}. Fig. 2.15 shows that $\sim 50\%$ pFOF groups of $N_{gal} < 20$ are consistent with CNOC2 groups. If we take the fraction of false detected pFOF groups to be $\sim 10\%$ based on the results of Test 2 in § 2.7.1, the result indicates that the completeness rate of CNOC2 group is $\sim 56\%$ for poor groups, which is similar to what was estimated (roughly 50%) in Carlberg et al. (2001).

2.9 Conclusions

In this chapter we have presented a new group-finding algorithm for identifying galaxy groups using photometric redshift catalogs. With the development of photometric redshift techniques, the interest of studying galaxy groups or clusters with photometric redshift has grown greatly. The relatively large uncertainties in the redshift estimation can cause problems in the identification of groups or clusters. Among the most common group finding techniques, the friends-of-friends method utilizes the straightforward approach by searching for over densities in galaxy distribution. However, the FOF algorithm is mostly used in spectroscopic redshift catalogs or simulated data sets for which the radial position information is well provided. We therefore develop an algorithm, pFOF, to identify galaxy groups using photometric redshift measurements.

The basic working principle of our pFOF algorithm is to improve the group redshift by joining new galaxy members. Mock catalogs are used to test the performance of pFOF algorithm including the effect of different linking criteria, input galaxy orders, and the Gaussian assumption of photometric redshift probability densities. Using samples with dispersion between simulated photometric and true galaxy redshift ~ 0.061, the comparisons as a function of both mock and pFOF group richness exhibit reasonable results: (1) greater than 80% of the mock groups of $1.2 \times 10^{13} M_{\odot}$ halo mass are recovered, (2) the fractions of false detected pFOF groups is about 10% for groups of $N_{gal} \geq 7.91$, and (3) $\sim 5\%$ of pFOF groups are flagged as 'serious projection' for which the pFOF group members are contributed by multiple mock groups. We find that the group finding results strongly depend on the sample depth. The samples should be sufficiently deep ($\sim M^* + 1.5$) into the luminosity function for reliable group finding results. Moreover, tests using samples of accurate redshift measurements reveal that the pFOF group membership strongly depends on the photometric redshift measurement accuracy. We also apply our algorithm to the RCS-CNOC2 patches, and compare the results to the published CNOC2 groups. The comparisons yield good agreements over $0.19 \leq z < 0.41$ for rich CNOC2 groups, and the results are consistent with the mock tests. In view of the above, we conclude that our group-finding algorithm is able to identify galaxy groups with the capability of dealing with photometric redshift uncertainties.

The purpose of developing this algorithm is to provide a method for searching for galaxy groups (and clusters) in photometric redshift data sets. We will apply this pFOF algorithm to the CNOC1 and RCS data sets. These data sets will provide us with a large sample of galaxy groups at $0.2 \leq z < 0.6$, and enable us to study the environmental

dependence of galaxy properties and their evolution.

References

Abazajian, K., et al. Adelman-McCarthy, J. K., Agüeros, M. A., Allam, 2005, AJ, 129, 1755

Berlind, A. A., et al. 2006, ApJS, 167, 1

Bolzonella, M., Miralles, J.-M., & Pelló, R. 2000, A&A, 363, 476

Botzler, C. S., Snigula, J., Bender, R., & Hopp, U. 2004, MNRAS, 349, 425

Brodwin, M., Lilly, S. J., Porciani, C., McCracken, H. J., Le Fèvre, O., Foucaud, S., Crampton, D., & Mellier, Y. 2006, ApJS, 162, 20

Budavári, T., et al. 2005, ApJ, 619, L31

Capak, P., et al. 2004, AJ, 127, 180

Carlberg, R. G., Yee, H. K. C., Morris, S. L., Lin, H., Hall, P. B., Patton, D. R., Sawicki, M., & Shepherd, C. W. 2001, ApJ, 552, 427

Chen, H.-W., Marzke, R. O., McCarthy, P. J., Martini, P., Carlberg, R. G., Persson, S. E., Bunker, A., Bridge, C. R., & Abraham, R. G. 2003, ApJ, 586, 745

Connolly, A. J., Csabai, I., Szalay, A. S., Koo, D. C., Kron, R. G., & Munn, J. A. 1995, AJ, 110, 2655

Cowie, L. L., Barger, A. J., Hu, E. M., Capak, P., & Songaila, A. 2004, AJ, 127, 3137

Croton, D. J., et al. 2006, MNRAS, 365, 11

Eke, V. R., et al. 2004, MNRAS, 348, 866

Geller, M. J. & Huchra, J. P. 1983, ApJS, 52, 61

Gerke, B. F., et al. 2005, ApJ, 625, 6

Giavalisco, M., et al. 2004, ApJ, 600, L93

Gladders, M. D. & Yee, H. K. C. 2005, ApJS, 157, 1

Hsieh, B. C., Yee, H. K. C., Lin, H., & Gladders, M. D. 2005, ApJS, 158, 161

Kodama, T. & Arimoto, N. 1997, A&A, 320, 41

Lin, H., Yee, H. K. C., Carlberg, R. G., Morris, S. L., Sawicki, M., Patton, D. R., Wirth, G., & Shepherd, C. W. 1999, ApJ, 518, 533

Marinoni, C., Davis, M., Newman, J. A., & Coil, A. L. 2002, ApJ, 580, 122

Merchán, M. E. & Zandivarez, A. 2005, ApJ, 630, 759

Mobasher, B., et al. 2004, ApJ, 600, L167

Springel, V., et al. 2005, Nature, 435, 629

Tago, E., et al. 2006, Astronomische Nachrichten, 327, 365

Weinstein, M. A., et al. 2004, ApJS, 155, 243

Wirth, G. D., et al. 2004, AJ, 127, 3121

Yee, H. K. C. 1991, PASP, 103, 396

Yee, H. K. C., Ellingson, E., & Carlberg, R. G. 1996, ApJS, 102, 269

Yee, H. K. C., et al. 2000, ApJS, 129, 475

Chapter 3

Environment Measures and Population Fraction

In Chapter 2, we presented a new method for identifying galaxy groups in a photometric redshift sample. This method, named the probability Friends-of-Friends (pFOF) method, uses the standard friends-of-friends linking idea in 2D space and utilizes group redshift as a conditional redshift probability density to determine group membership in redshift. The overall excellent performance of the method has already been demonstrated by applying it to the mock catalogs from the Virgo Consortium Millennium Simulation and the data from the CNOC2 field redshift survey. The primary motivation for developing this algorithm is its application to the dependence of galaxy properties on their group environment. It is commonly accepted that the majority of galaxies in high galaxy density regions appear red in color, and the central regions of galaxy clusters are dominated by the red galaxy population (see § 1.3 in Chap 1). By examining when, where and how galaxies are being transformed, we can gain information on the nature of the physical mechanisms responsible for the transformation. Therefore, with an attempt to study galaxy photometric properties in different environments associated with galaxy groups and clusters, we demarcate the environmental effects into the *local* and *global* regimes. For the purpose of unfolding the environmental effects on galaxy evolution, we shall investigate the dependence of galaxy properties on *only* one environmental variable with other parameters controlled. In this chapter we define different environment measures and demonstrate the calculation of the population fraction. The structure of this Chapter is as follows. We start with the estimation of background galaxies as a function of redshift in § 3.1. The environmental parameters are defined in § 3.2, and the computation of population fraction is detailed in § 3.3. Finally we present a summary in § 3.4. We will

use these parameters in our investigation of properties of galaxies in groups and clusters in Chapters 4, 5, and 6.

3.1 Background Galaxy Density

Correction of background galaxy counts is essential for any works using photometric redshift, because of the less accurate redshift measurement. For the purpose of studying galaxy properties at a cluster or group redshift, even though the photometric redshift technique helps eliminate most fore- or background galaxies, some of them are still scattered into the cluster or group redshift space. On the other hand, some of actual cluster or group galaxies may scatter into other redshift space. Statistically, we expect similar numbers of galaxies which scatter in and out in the field at a redshift interval. However, in a cluster or group redshift, there are more cluster or group galaxies scattered into other redshift spaces than the reverse direction. This may cause a bias in the studies of galaxy properties at a specific redshift, if such differentiated accuracies in photometric redshift measurement exhibited by galaxies of different types are not corrected.

It is impossible to identify which galaxies are contributed from the background without knowing their actual redshifts. Fortunately, the counts or number density of the contaminating galaxies at a specific redshift can be estimated statistically by averaging galaxies over a sufficiently large area.

We use three RCS CFHT patches (*0920*, *1417*, and *1614*; Gladders & Yee 2005; Hsieh et al. 2005) as the control fields to derive galaxy surface density as a function of redshift. These three RCS patches have the deepest photometry and cover a total of 11.83 square degrees. To construct the redshift distribution function $n(z)$ of galaxies within a projected area, we first select galaxies in the control fields using the same selection criteria as the sample, including selections in photometric redshift and sample depth. We then count the number of galaxies at each redshift, $N(z)$, using a bin size of 0.01 by summing up all the weighted probability densities in photometric redshift in this redshift interval, as

$$N(z) = \int_{z-0.005}^{z+0.005} P_i(z') w_i dz',$$

where $P_i(z)$ is the photometric redshift probability density of each galaxy and w_i is the complete weight due to the removal of galaxies of unreliable photometric redshift measurements. The surface density at each redshift $n(z)$ is accordingly obtained by dividing $N(z)$ with the total area of the RCS control samples at each redshift. We

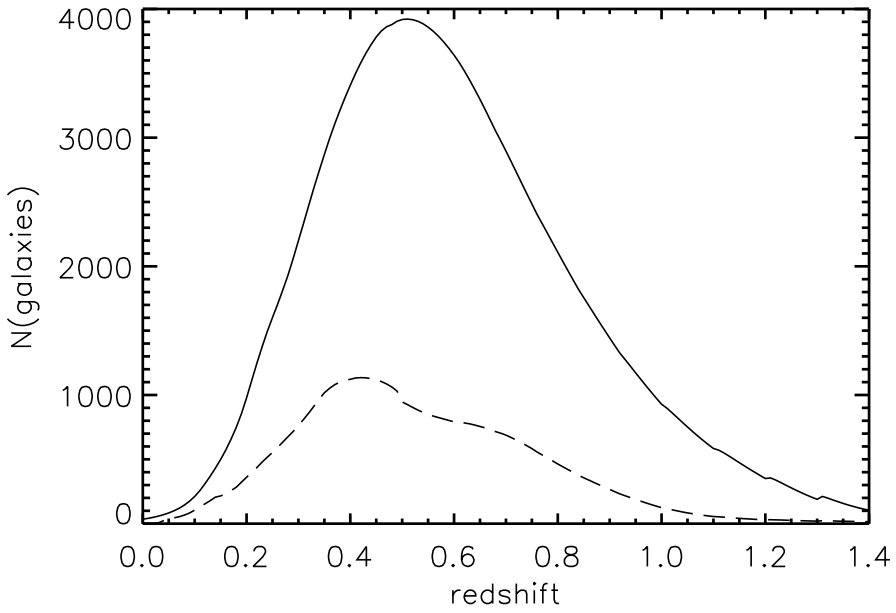

Figure 3.1: The total background galaxy counts as a function of redshift (the solid curve) computed using a control sample of depth to $M^*_{R_c} + 1.5$ over an area of 11.83 squared degree. The dashed curve is for the red galaxies, which are defined using galaxies of color redder than halfway between the colors of the early- and late-type galaxies at each redshift. The control samples become incomplete to $M^*_{R_c} + 1.5$ at $z > 0.5$.

present the $N(z)$ as a function of redshift in Fig. 3.1.

In § 2.6 in Chapter 2 we have presented the computation of the estimated contaminating galaxies within a galaxy group contributed by the background, $\Sigma_{grp,bg}$, as

$$\Sigma_{grp,bg} = \int L(z)n(z)dz,$$

where $L(z)$ is the photometric redshift likelihood of a galaxy group. Note that $n(z)$ is expressed as $\Sigma_{bg}(z)$ in § 2.6.

3.2 Environmental Parameters

3.2.1 Local Galaxy Environment: Local Projected Galaxy Density

To characterize the local galaxy environment we use local galaxy number density as a conventional approach to provide a spatial description of the local environment. A non-

parametric method to determine such density is based on the n^{th} nearest neighbor. In a simulated or redshift complete survey where accurate redshift information is available, this n^{th}-nearest-neighbor method uses the volume $V(r)$ centered on a given galaxy as a variable, and let the volume extend to its n^{th}-nearest-neighbor. Consequently, this volume is large in low galaxy density regions, and small in high galaxy density locations. However, galaxy velocity dispersion becomes higher in denser environment, such galaxy density estimation using the n^{th}-nearest-neighbor method could underestimate local densities without correcting for peculiar velocities in distance measurement (Mateus et al. 2007). In order to avoid this effect, a better way to derive local galaxy density using the nearest-neighbor method is to consider a projected distribution of galaxies instead of the true spatial one. A common approach is to restrict neighbors to a given velocity interval to exclude foreground and background objects, then measure the projected distance to the nearest-neighbors. This projected n^{th}-nearest neighbor distance r_n is expressed as a surface density, $\Sigma_n = n/(\pi r_n^2)$. This procedure in using projected galaxy density has been intensively adopted in studies devoted to galaxy environments such as the papers using 2dFGRS (e.g., Lewis et al. 2002) and SDSS (e.g., Gómez et al. 2003; Goto et al. 2003; Blanton et al. 2003; Balogh et al. 2004) data.

However, to calculate the local projected galaxy density in a photometric redshift sample, the computation of Σ_n should be corrected for the background contamination. In this work we use the expression

$$\Sigma_5 = \frac{\sum_i^n w_i - \pi r_5^2 \Sigma_{bg}(z_{igal})}{\pi r_5^2}$$

to estimate the local projected galaxy density based on the distance to the 5^{th} nearest-neighbor. All these neighbors are selected to be in the same redshift space as the central galaxy *igal* using the $P_{ratio,crit}$ criterion described in Chapter 2. In this calculation, n is the 5^{th}-nearest projected galaxy such that the total completeness weight $\sum_i^n w_i \geq 5$, r_5 is the distance in Mpc to this 5^{th}-nearest galaxy, and $\Sigma_{bg}(z_{igal})$ is the estimated background galaxy density in the redshift space of the central galaxy. This correction for the background galaxy density is necessary, because we are using photometric redshifts which are considerably less accurate than the spectroscopically measured redshifts.

A correction is applied to the local projected galaxy density when galaxies are located near the edges of the missing survey pointings or chips. To compute the correction in local projected galaxy density, we first cast randomly but uniformly distributed points over a patch. Using 40,000 points within a 2k×4k chip, each galaxy is then assigned a circle with radius of its r_5. By counting the numbers of the uniformly distributed points,

we can estimate the actual area within the r_5 to the seed galaxy, and calculate the actual galaxy density locally within the r_5 distance. A set of points is then draw from the random field based on this estimated density over the missing area. Each of these points is treated as a galaxy. The r_5 and the Σ_5 are then re-calculated with these fake galaxies included. About 93% of galaxies maintain their Σ_5 values with corrections of $< 10\%$, and 7% of them have their Σ_5 corrected significantly.

3.2.2 Global Cluster Environment: Cluster-centric Radius

The fact that galaxies in clusters are different from galaxies in the field has been attributed to a variety of mechanisms acting on a variety of scales. It has been suggested that galaxies can rebound up to $1.77R_{200}$ (Mamon et al. 2004) as they fall into a cluster, thus blurring the definition of cluster and field. One way to gauge the environmental influence of galaxy clusters is to investigate galaxy properties at different spatial distances from the cluster centers. However, such distance measurements should be scaled based on the cluster virial radius to consider the variation in the mass of the clusters in a sample. If a fixed physical scale is used, it may include the cores of the most massive clusters and a substantial part of the outskirts of the less massive clusters. A common approach to define the cluster virial radius is to integrate the cluster density profile up to the radius R_k with the interior mean density k times the critical density.

We adopt R_{200} as the virial radius of our clusters, and use the *cluster-centric radius* in units of R_{200} (denoted as 'r_{CL}') to delineate the global cluster environmental effect. Our cluster samples contain the spectroscopically confirmed CNOC1 clusters and the photometrically identified RCS clusters via the red-sequence method. The R_{200} for the CNOC1 clusters has been published in Carlberg et al. (1997), and we adopt empirically derived R_{200} for the RCS cluster samples using the correlation between cluster richness and R_{200} as shown in Yee & Ellingson (2003).

3.2.3 Environment Within Galaxy Groups: Group Richness and Group-centric Radius

With a line-of-sight velocity dispersion of few hundred km/s (e.g., Ramella et al. 1989; Tucker et al. 2000; Carlberg et al. 2001), galaxy groups exhibit similar but not entirely identical properties as clusters, such as differentiated galaxy morphology and luminosity at different group-centric radii. These gradients in the properties of group galaxies in-

dicate the correlation between galaxies and their group environment. To probe the role of galaxy groups in galaxy evolution, we discuss the role of galaxy groups using group richness and group-centric radius.

In § 2.6 in Chapter 2 we have defined N_{gal} and N_{gz} as the group richness parameters. N_{gz} is the total number of galaxies linked together into a group, and N_{gal} is the net total member count in a galaxy group after correcting for the background contaminating galaxies.

However, owing to the linking procedure in the pFOF algorithm, galaxies in the same halo may break into more than one aggregation, hence N_{gal} may fail to represent the true group richness related to the halo mass. Therefore, we adopt another group richness parameter insensitive to the sub-clustering of group galaxies: B_{gc}. The B_{gc} is defined as the amplitude of the cluster center-galaxy correlation function, and can be estimated via a deprojection of the angular correlation function into the spatial one by assuming spherical symmetry. In other words, the B_{gc} amplitude is estimated by counting the excess galaxy counts up to a certain apparent magnitude within a given radius, and is corrected for the background counts and scaled by the luminosity function. The details on the computation and the tests of the robustness of B_{gc} are described in Yee & López-Cruz (1999).

In an infall picture, new galaxies are added at the periphery of a galaxy group. As a result, group galaxies should exhibit different properties at various group-centric radii. By the same token as the last subsection, we use group-centric radii normalized by the group virial radius R_{200} to discuss different galaxy group environments within a galaxy groups. The R_{200} values for groups are also estimated using the R_{200}-B_{gc} correlation established by Yee & Ellingson (2003).

3.3 The Red Galaxy Fraction

For galaxies in a given environment or within a galaxy group, their photometric properties are quantified by the f_{red} parameter, the *red galaxy fraction* . This f_{red} is computed using galaxies of various absolute magnitude bins up to $M^*_{R_c} + 1.5$ on the observed color-magnitude diagram with m_{R_c} properly k- and evolutionary corrected. Since galaxy SED type is characterized by the rest 4000 Å break, we define red galaxies using observed galaxy $B - R_c$ color at $z < 0.5$ and $V - I_c$ color at $z > 0.5$, so that the rest 4000 Å break is straddled by the chosen filters.

The red galaxies are defined as galaxies within a color slice of the observed red se-

quence at a given redshift. We adopt the theoretical color-magnitude sequence built by Kodama & Arimoto (1997). We cross-check the zero-points between the model and observed red-sequence color in our samples. An offset is applied to the zero-point of the model if such an offset is observed. The lower boundary to define the 'red region' is based on half the color difference between the E/S0 and Sc galaxies at the redshift of the sample. The upper boundary is set as $\Delta(B - R_c)$=0.30 above the red sequence. Since the f_{red} is computed on the observed color-magnitude diagram, the locations of the color boundaries vary with redshift.

To consider the uncertainties in computing the fraction of red galaxies, we assume a Gaussian color uncertainty for each galaxy, so that the probability of each galaxy within the 'red region' can be estimated. The total number of red galaxies N_{red} is, consequently, the sum of these probabilities within this red region.

We compute f_{red} using a statistical inference, because the number of galaxies in a certain environment (such as in a galaxy group) is not large in most situations, and the background contamination plays a role in estimating the true fraction of red group members (D'Agostini 2004; Andreon et al. 2006). The following is a demonstration in computing f_{red} for a galaxy group. The same idea can be applied to a set of individual galaxies in any given environment. Let us assume that the number of total and red galaxies in a given environment are:

$$N_{tot} = N_{grp} + N_{bg} = N_{gal} + N_{bg},$$

and

$$N_{red} = N_{grp,red} + N_{bg,red} = \sum w_{i,red} + N_{bg,red},$$

where both $N_{grp,red}$ and $N_{bg,red}$ follow the binomial distribution. The symbol N denotes the number of objects indicated by the subscripts, and *'bg'* abbreviates *background*. With only N_{tot} and N_{red} observed, the probability function F of f_{red} (a posterior) is inferred as:

$$F(f_{red}|N_{red}, N_{tot}, \lambda_b, P_b), \tag{3.1}$$

where P_b is the portion of red galaxies contained in the background, i.e., $N_{bg,red} = P_b \cdot N_{bg}$, and λ_b is the expectation value of the background galaxy count assuming a Poisson distribution. Using Bayes' theorem, the posterior probability can be written as:

$$F(f_{red}|N_{red}, N_{tot}, \lambda_b, P_b) = \sum_{N_{grp,red}} F(N_{red}|N_{tot}, \lambda_b, P_b) \cdot F_0(N_{grp}, f_{red})$$

$$= \sum_{N_{grp,red}} \delta_{N_{tot},N_{grp}+N_{bg}} F(N_{red}|N_{grp}, f_{red}, N_{bg}, P_b) F(N_{bg}|P_{\lambda_b}) F_0(N_{grp}, f_{red})$$

where $\delta_{N_{tot},N_{grp}+N_{bg}} = 1$ *only* if $N_{tot} = N_{grp} + N_{bg}$, and $F_0(N_{grp}, f_{red})$ is the prior. Since both $N_{grp,red}$ and $N_{bg,red}$ follow the binomial distribution, the $F(N_{red}|N_{grp}, f_{red}, N_{bg}, P_b)$ term in the above expression can be written as the sum of two binomial variables,

$$F(N_{red}|N_{grp}, f_{red}, N_{bg}, P_b) = \sum_{N_{grp,red},N_{bg,red}} \delta_{N_{red},N_{grp,red}+N_{bg,red}} F(N_{grp,red}|B_{N_{grp},f_{red}}) F(N_{bg,red}|B_{N_{bg},P_b})$$

where $N_{grp,red}$ can range from 0 to N_{grp} and $N_{bg,red}$ from 0 to N_{bg}, and $B_{n,p}$ is the well known binomial distribution. In short, by assuming a uniform prior, i.e., $F_0(N_{red}, f_{red}) =$ *constant*, we can write the probability function of f_{red} as:

$$F(f_{red}|N_{red}, N_{tot}, \lambda_b, P_b)$$

$$\propto \sum_{N_{grp,red}}^{0 \to N_{grp}} \frac{N_{grp}!}{(N_{grp} - N_{grp,red})! N_{grp,red}!} f_{red}^{N_{grp,red}} (1 - f_{red})^{N_{grp} - N_{grp,red}}$$

$$\frac{N_{bg}!}{(N_{bg} - N_{bg,red})! N_{bg,red}!} P_b^{N_{bg,red}} (1 - P_b)^{N_{bg} - N_{bg,red}} \frac{e^{-\lambda_b} \lambda_b^{N_{bg}}}{N_{bg}!}.$$

Accordingly, we take the mean and the 68% central confidence interval of f_{red} probability function as the estimated f_{red} and its uncertainty. We illustrate examples of f_{red} probability function for the cluster groups in Fig 3.2 with the shaded regions delimiting the 68% central confidence interval.

3.4 Summary

To study galaxy photometric properties in various environments, we have defined proxies to parameterize different environments. We are interested in influences due to local and global environments. The local environment proxy is the projected galaxy density calculated based on the 5^{th}-nearest-neighbor method. The global environmental parameter is the cluster-centric radii in unit of the virial radii. We are also interested in galaxy environment in galaxy groups, which are identified using the pFOF algorithm described in Chapter 2. We use group richness in terms of net count of group members (expressed as the B_{gc} parameter) and group-centric radii scaled by group virial radii to describe the environments offered by galaxy groups. The photometric properties of galaxies in a given environment is indicated by the f_{red} parameter, the fraction of red galaxies. We have detailed its computation from the viewpoint of statistical inference for a better estimation of the true fraction of red galaxies. Galaxies tend to form into galaxy groups, and

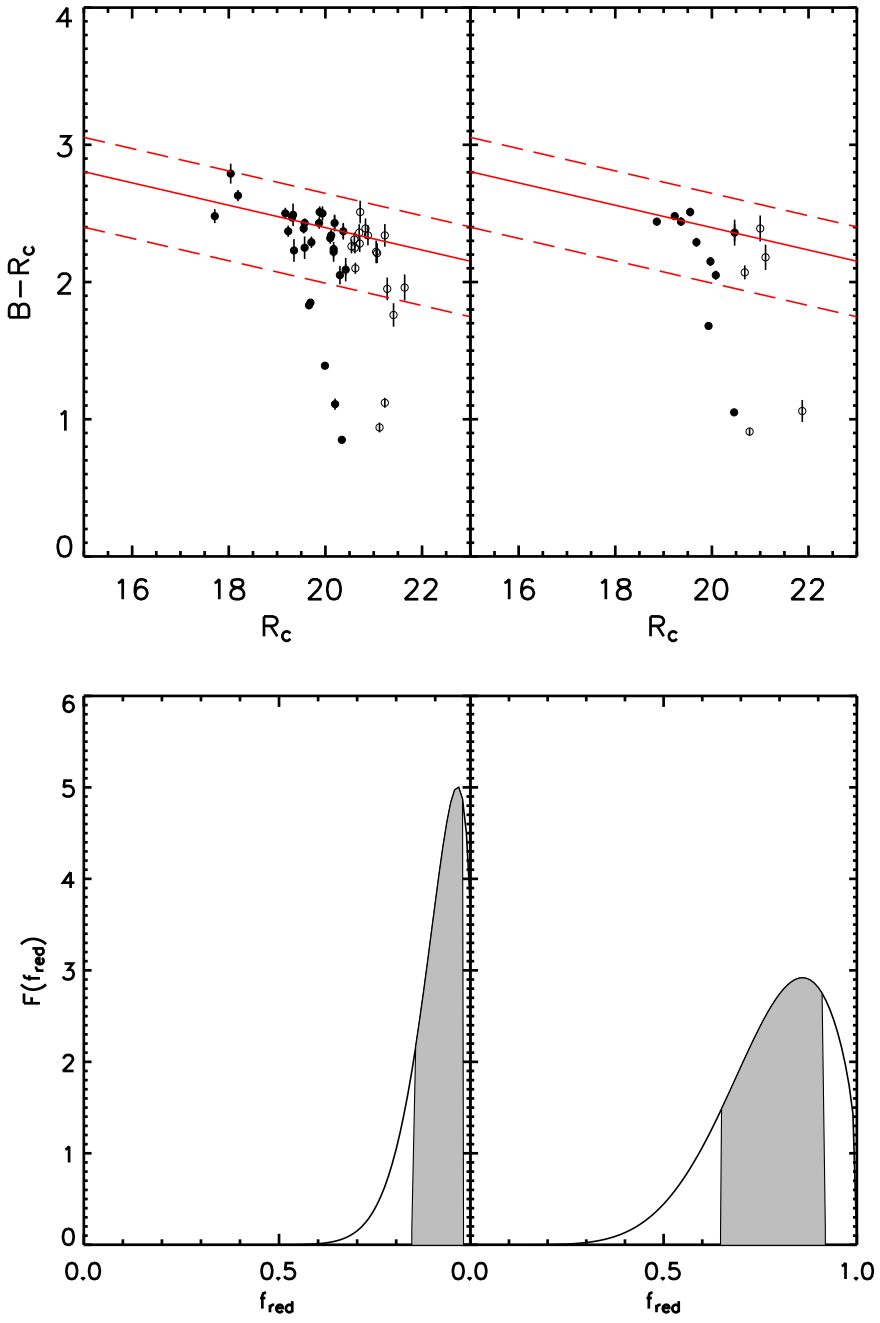

Figure 3.2: *Top:* The observed color-magnitude diagrams for members in two galaxy groups in the redshift space of a cluster at $z_{pFOF} = 0.239$, where the solid and open circles represent galaxies brighter and fainter than $M^{k,e}_{R_c} = M^*_{R_c} + 1.5$, respectively. Note that no correction in background galaxies for the group members has been carried out. The solid line is the theoretical color-magnitude relation at the cluster redshift, and the region between the two dashed lines defines the red galaxies. The lower boundary is set based on half of the color difference between early- and late-type galaxies. *Bottom:* The distribution function of red galaxy fraction for the same two galaxy groups as the *Top* plot but with background count corrected in the f_{red} computations. The shaded area is the 68% of the central confidence interval.

whole groups can be dragged into clusters along filaments. Consequently, properties of galaxies in a specific location can be affected by various environments simultaneously. In the following three chapters, we will probe the trends of f_{red} as a function of only one environmental parameter with others controlled, so that any changes in f_{red} can reflect the influence of only a certain environment.

References

Andreon, S., Quintana, H., Tajer, M., Galaz, G., & Surdej, J. 2006, MNRAS, 365, 915

Balogh, M. L., Baldry, I. K., Nichol, R., Miller, C., Bower, R., & Glazebrook, K. 2004, ApJ, 615, L101

Blanton, M. R., et al. 2003, ApJ, 594, 186

Carlberg, R. G., Yee, H. K. C., & Ellingson, E. 1997, ApJ, 478, 462

Carlberg, R. G., Yee, H. K. C., Morris, S. L., Lin, H., Hall, P. B., Patton, D. R., Sawicki, M., & Shepherd, C. W. 2001, ApJ, 552, 427

Cooper, M. C., Newman, J. A., Madgwick, D. S., Gerke, B. F., Yan, R., & Davis, M. 2005, ApJ, 634, 833

D'Agostini, G. 2004, ArXiv Physics e-prints

Domínguez, M. J., Zandivarez, A. A., Martínez, H. J., Merchán, M. E., Muriel, H., & Lambas, D. G. 2002, MNRAS, 335, 825

Dressler, A. 1980, ApJ, 236, 351

Eke, V. R., et al. 2004, MNRAS, 348, 866

Faltenbacher, A. & Mathews, W. G. 2007, MNRAS, 375, 313

Gómez, P. L., et al. 2003, ApJ, 584, 210

Goto, T., Yamauchi, C., Fujita, Y., Okamura, S., Sekiguchi, M., Smail, I., Bernardi, M., & Gomez, P. L. 2003, MNRAS, 346, 601

Kodama, T. & Arimoto, N. 1997, A&A, 320, 41

Lewis, I., et al. 2002, MNRAS, 334, 673

Mamon, G. A., Sanchis, T., Salvador-Solé, E., & Solanes, J. M. 2004, A&A, 414, 445

Mateus, A., Sodré, L., Cid Fernandes, R., & Stasińska, G. 2007, MNRAS, 374, 1457

Ramella, M., Geller, M. J., & Huchra, J. P. 1989, ApJ, 344, 57

Tucker, D. L., et al. 2000, ApJS, 130, 237

Yee, H. K. C. & Ellingson, E. 2003, ApJ, 585, 215

Yee, H. K. C. & López-Cruz, O. 1999, AJ, 117, 1985

Chapter 4

The Individual and Group Galaxies in X-ray Selected Clusters: the CNOC1 Sample

4.1 Introduction

In Chapter 2 we presented a new method for identifying galaxy groups using photometric redshift. This method, dubbed the probability friends-of-friends (pFOF) algorithm, utilizes the group redshift space as a conditional probability density to consider uncertainties in the photometric redshift of individual galaxies. The primary motivation for developing the algorithm is its application to mutli-wavelength broadband photometry data sets to provide a large sample of galaxy groups, with the goal to explore various environmental influences on galaxy properties. In this Chapter we present an investigation of galaxy properties in cluster, group, and their local environments from the CNOC1 cluster sample.

With increasingly detailed studies of galaxy properties such as stellar populations and morphology, our knowledge of galaxies in the Universe has greatly improved. The large-scale structure in the Universe shows that some galaxies are located in low-density filaments while others populate high-density clusters. This complicates our understanding of galaxy evolution over the Hubble time, because galaxy properties depend not only on time but also on environment. Therefore, in order to picture galaxy evolution in the Universe, galaxy properties need viewing simultaneously and systematically over time and in different environments.

Since the first quantitative study using 55 clusters by Dressler (1980), the morphology-density relation is well accepted as evidence for the environmental dependence of galaxy properties. Early-type galaxies favour the dense environment, while late type galaxies are common in less dense environment. Following this pioneering work, a considerable number of studies on this topic have been carried out or extended (e.g., Domínguez et al. 2001; Goto et al. 2003; Hogg et al. 2003; Tanaka et al. 2005; Nuijten et al. 2005; Tanaka et al. 2005). The general conclusion is that this morphology-density relation still applies to galaxies in concentrated and regular clusters at high redshift ($z \sim 0.5$) (Dressler et al. 1997).

In order to unfold the role of time and environment in galaxy evolution in clusters, we study these two major factors using both individual galaxies and galaxy groups in 16 clusters from the CNOC1 follow-up observations. Galaxy clusters grow by accreting infalling galaxies and groups. The cluster central region is occupied by the uniform old and red population. Moreover, $\sim$ 60% galaxies are found in groups (Tully & Fisher 1987; Eke et al. 2004) and galaxies in a group may have evolved already before the whole group falls into a cluster: i.e., what is referred to as *pre-processing* (Fujita 2004). Therefore, cluster and group galaxy populations give us a unique opportunity to study the environmental effect on large (global) and small (local) scales.

The main aim of this work is to investigate the color properties of cluster galaxies when they are located in group environment or in the low galaxy density regions, and hence offer a study for comparison with galaxies in the field. The structure of this chapter is as follows. We present the data in §4.2. Then we briefly describe the photometric redshift method to estimate galaxy redshift and sample selection in §4.3. We delineate the group finding method and the parameters to quantify groups in §4.4. The identification of cluster galaxies and groups are detailed in §4.5. We review the calculations of the environmental parameters and red galaxy fraction in §4.6. The results are given in §4.7. Finally we discuss the environmental effects from the perspectives of individual cluster galaxies and those in galaxy groups and summarize the results in §4.8. We adopt $\Omega_m = 0.7$, $\Omega_\Lambda = 0.3$, and $H_0 = 70$ km/s/Mpc.

4.2 The Cluster Catalogs

4.2.1 The Data

The original CNOC1 Cluster Redshift Survey (Yee et al. 1996) contains a total of 16 rich X-ray selected galaxy clusters at $0.17 < z < 0.55$ with the main goal of measuring the density parameter, Ω_m. The observations were made using the CFHT Multi-Object-Spectrograph (MOS) with Gunn g and r images to $r \sim 24$ and spectroscopy to $r \sim 21.5$. The multi-color photometric follow-up observations in this study targeted 15 of the CNOC1 clusters using the CFHT 12K camera carried out in a total of 9 nights in 2000 and 2001. The camera, composed of 12 chips with $0.206''$ per pixel, has a $42' \times 28'$ field of view. Five clusters were taken from queue observations and the other ten were from classic observations. Among these 15 clusters, 14 clusters were in $BVRI$ with seeing from $\sim 0.70''$ to $1.24''$ in the R_c-passband. MS0015+16 (CL0015+16, z=0.55) was observed in B and V only, and hence is excluded for not having enough passbands for our photometric redshift method. We also exclude the MS1224+20 field because this field is non-photometric and not deep enough for our science purpose. MS0302+16 (z=0.425, $\alpha_{2000} = 03:05:35.42$, $\delta_{2000} = 17:10:3.43$) was targeted incorrectly to MS0302.5+1717 (z=0.425, $\alpha_{2000} = 03:05:18.110$, $\delta_{2000} = 17:28:24.92$), about $18.82'$ North from the original CNOC1 target. Another cluster, CL0303+1706 (z=0.418, $\alpha_{2000} = 03:06:18.7$, $\delta_{2000} = +17:18:03$), is in the South-East of MS0302.5+1717.

The pointings for MS1231+15 and MS1358+62 contain other clusters in the field. Abell 1560 ($\alpha_{2000} = 12:34:07.1$, $\delta_{2000} = 15:10:28$, z=0.244; Abell et al. 1989; Ulmer & Cruddace 1982; David et al. 1999) is South of MS1231+15. MS1358+62 has been known as a binary cluster in CNOC1 analysis (Carlberg et al. 1996). The other cluster in the MS1358+62 field is at $\alpha_{2000} = 13:59:39.511$, $\delta_{2000} = 62:18:47.0$, and z=0.329. In summary, our data set contains 12 CNOC1 clusters in the follow-up sample and 4 other confirmed clusters. The sample properties and exposure times are listed in Tables 4.1 and 4.2.

4.2.2 Photometry and Color Calibration

For the queue observed data, the basic data reduction steps and calibrations were undertaken using the *Elixir* system at CFHT. For the classically observed data, the data reduction proceeded in the standard way using IRAF, including bias subtraction and flat fielding. The photometric calibration was performed by using images of standard fields

Table 4.1: Properties of CNOC1 Follow-up Data Set

Cluster	R.A.(J2000)	Dec.(J2000)	z	$m_{R_c,lim}$	seeing[a]	note
MS0302+1717	03:05:18.1	17:28:24.9	0.425	24.10	0.7	classical
						not the CNOC1 cluster
CL0303+1706	03:06:18.7	17:18:03.0	0.418			S-E field
						not the CNOC1 cluster
MS0440+02	04:43:09.9	02:10:21.4	0.197	23.71	0.58	classical
MS0451+02	04:54:14.1	02:57:10.5	0.201	23.72	0.68	classical
MS0451-03	04:54:10.9	-03:00:57.1	0.539	22.80	1.11	classical
MS0839+29	08:42:55.9	29:27:27.3	0.193	23.05	0.86	classical
MS0906+11	09:09:12.7	10:58:29.2	0.171	23.03	0.82	classical
MS1008-12	10:10:32.3	-12:39:52.5	0.306	23.35	1.17	classical
MS1224+20	12:27:13.3	19:50:56.5	0.330	21.70		queue, not use
MS1231+15	12:33:55.4	15:25:59.1	0.235	23.80	0.82	queue
Abell 1560	12:34:07.1	15:10:28.2	0.244			S field
						not the CNOC1 cluster
MS1358+62	13:59:50.5	62:31:04.5	0.329	22.65	1.24	classical
	13:59:38.0	62:18:47.0	0.329			S field
						not the CNOC1 cluster
MS1455+22	14:57:15.1	22:20:33.9	0.257	23.20	0.93	queue
MS1512+36	15:14:22.5	36:36:20.9	0.373	23.85	0.87	queue
MS1621+26	16:23:35.5	26:34:15.9	0.428	23.35	0.93	classical
Abell 2390	21:53:36.8	17:41:43.7	0.228	24.05	0.72	classical

[a] in R_c-band frame in arcsecond

Table 4.2: Total Exposure Time[a] for Each Observing Frame

Cluster	B	V	R_c	I_c	Cluster	B	V	R_c	I_c
MS0302+16	92	20	16	16	MS1224+20	69	12	12	12
MS0440+02	20	7	7	7	MS1231+15	20	7	7	7
MS0451+02	20	7	7	7	MS1358+62	69	15	10.5	15
MS0451-03	60	69	24	24	MS1455+22	20	7	7	7
MS0839+29	20	7	7	7	MS1512+36	23	15	14	14
MS0906+11	40	7	7	14	MS1621+26	20	12	16	10
MS1008-12	44	7	14	7	Abell 2390	15	10	10	12

a: in minutes

from Landolt (1992).

The object finding, aperture photometry, and star-galaxy classification were carried out using the *Picture Processing Package* (*PPP;* Yee 1991; Yee et al. 1996). This package has the capability to perform faint galaxy photometry in a moderately crowded field. The object-finding algorithm is carried out based on the signal-to-noise ratio of the input pixels. This algorithm detects objects by systematically examining each pixel in an image and identifying the locations of peak brightness of objects in the image. Objects with an intensity above a preset selection threshold level and satisfying a number of criteria (e.g., a minimum number of connected pixels, a sharpness test, etc., see Yee et al. (1996)) are then cataloged. In general, about 2,000 to 3,000 objects on average are detected in each chip. The photometry is achieved by constructing and analyzing the flux growth curve of an object. The total magnitude is measured in an 'optimal aperture', and then corrected to a standard aperture of 8.5″ diameter using the PSF profile of reference stars, if the optimal aperture of an object is smaller than the standard aperture. The color of each object is measured independently from the total magnitude, using a 'color aperture' of 3″ (or the optimal aperture, whichever is smaller). The total magnitude for the second filter is then computed from the color and the total magnitude of the first filter. The star-galaxy classification is accomplished by comparing the growth curve of each object to a local set of bright, but not saturated, reference stars. The algorithm classifies objects into four categories: galaxies, stars, saturated stars, and spurious 'non-object' (cosmic ray detection or cosmetic defects, for example). The details of this package are described

in Yee (1991) and Yee et al. (1996).

In order to check the photometry of the CNOC1 follow-up observation, we compare R_c to Gunn r, which were taken in the original CNOC1 observation, using the transformation $r = R_c + 0.28 + 0.027 \times (B - R_c)$ derived from the M67 field. To check the color offsets in other passbands, we take the calibrated R_c photometry as the reference. For B and V photometry, we compare the star colors to those in the *Red-Sequence Cluster Survey* (RCS; Gladders & Yee 2005) CFHT patches (Hsieh et al. 2005) using bright stars ($18 \leq R_c \leq 22$). Because the RCS uses $BVRz'$ instead of $BVRI$ passbands, we compare the distributions of $I - R_c$ star colors to those in the MS1231+15, MS1455+22, and MS1512+36 fields. These three pointings were processed using the *Elixir* system, for which the I-band photometry are consistent with each other after being crossing-checked. The zero points in BVI are shifted if any color offsets are present. The color correction ensures consistent photometry estimation of galaxies in the samples.

4.2.3 Astrometry

The astrometry information of each frame was calibrated using the IRAF package **MSCRED** with USNO-a2 catalogs. The **MSCRED** package has the ability to operate on multi-CCD data simultaneously without the need to split each image frame into separate CCD images and process them individually. Therefore, each CNOC1 12K follow-up observation pointing was made into a multi-extension FITS with 12 extensions. An astrometry calibration file was generated by **msctpeak** command based on the MS0302+16 field. After updating the image headers with the calibration file, **mscczero** and **msccmatch** commands were used to apply the shifts and match the positions between the objects on the images and USNO-a2 catalogs. To be consistent, the coordinate of each object was precessed to be in J2000. We also updated the astrometry in the headers of the original CNOC1 MOS images, so the 12K objects can be easily matched with the those spectroscopically observed using MOS.

4.3 Photometric Redshift and Sample Selection

The photometric redshift technique allows us to estimate galaxy redshift with photometry information. Due to fuzzier redshift information obtained from the photometric redshift technique, it requires careful considerations in selecting the samples. In this section we review the photometric redshift technique and the sample selection, for which the details

can be found in § 2.2 and § 2.3 in Chapter 2.

4.3.1 Redshift Estimation

Galaxy redshifts are estimated using the empirical photometric redshift technique from Li & Yee (2007, see Chapter 2). The empirical photometric redshift technique assumes that redshift is a polynomial function of galaxy colors and magnitudes. The coefficients of this polynomial can be estimated by fitting the galaxies in a training set, which is a catalog containing the information of galaxy redshifts and magnitudes. Our training set contains 3988 galaxies in $BVRIz'$ up to $z \sim 1.4$ with $R_c < 24.$, constructed from the Hubble Deep Field (Giavalisco et al. 2004) and CNOC2 catalogs (Yee et al. 2000). The properties of the training set are described in Hsieh et al. (2005) and Chapter 2. To achieve better constrained solutions, the galaxies with spectroscopic redshifts in the CNOC1 sample (2022 galaxies in total) are added to the training set. The photometric redshift uncertainties and probability densities of individual galaxies are obtained in this photometric redshift technique as well.

To assess the accuracy of our photometric redshift, we compare the photometric redshifts with the spectroscopic ones for the 2022 galaxies with spectroscopic redshifts from the original CNOC1 MOS observation in Fig. 4.1. The differences between photometric and spectroscopic redshifts are plotted in Fig. 4.1 as a function of galaxy magnitude and $B - R_c$ color. The overall $\sigma(z_{phot} - z_{spec})$ is ~ 0.051, with $\sigma(z_{phot} - z_{spec}) \sim 0.048$ and ~ 0.108 for $R_c < 21.5$ and $R_c \geq 21.5$, respectively. Blue galaxies ($B - R_c < 1.8$) has $\sigma(z_{phot} - z_{spec}) \sim 0.070$, while $\sigma(z_{phot} - z_{spec})$ for red galaxies ($B - R_c \geq 1.8$) is ~ 0.041.

4.3.2 Galaxy Sample Selection

A sample of galaxies is selected in a photometric redshift range of $0.02 \leq z \leq 1.4$. The upper photometric redshift limit is due to the passband wavelength coverage for the 4000 Å break in our training set. We select galaxies by their photometric redshift probability densities within a range based on each galaxy's photometric redshift z_i satisfying:

$$P(z) = \int_{z_i - 3\sigma_{z_c ut}}^{z_i + 3\sigma_{z_c ut}} P_i(z')dz' > 0.997.$$

with $\sigma_{z_c ut}$ set to 0.2(1+z), which is equivalent to not including galaxies whose photometric redshift uncertainties is larger than 0.2(1+z). Each galaxy in the sample is then assigned a completeness correction weight w_i to account for galaxies excluded from the sample due to the $\sigma_{z_c ut}$ criterion.

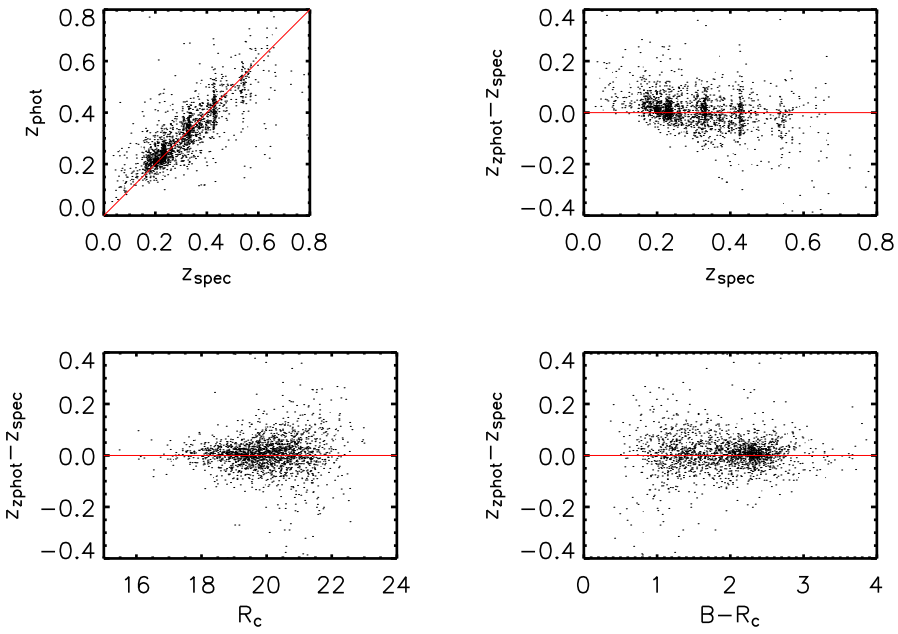

Figure 4.1: The estimated photometric redshift for 2022 CNOC1 galaxies with spectroscopic redshift. The top two panels are the comparison between the spectroscopic and photometric redshift. The overall dispersion is $\sigma(z_{phot} - z_{spec}) \sim 0.051$. At $z < 0.1$, the photometric redshift measurements are affected by not having a sufficiently blue band. The bottom two panels plot the $z_{phot} - z_{spec}$ as functions of galaxy magnitude and color. The difference is larger toward the fainter magnitude and blue color: $\sigma(z_{phot} - z_{spec}) \sim [0.048, 0.108]$ for $R_c < 21.5$ and $R_c \geq 21.5$, and $\sigma(z_{phot} - z_{spec}) \sim [0.041, 0.070]$ for $B - R_c \geq 1.8$ and $B - R_c < 1.8$.

The completeness correction is computed using the ratio of total galaxy number to the galaxy number satisfying our selection criteria in magnitude bins of $\Delta m = 0.1$. We set a cutoff in R_c based on where $w_i = 2$ to avoid high weight galaxies. The median and mean completeness correction factor w_i in the sample is ~ 1.079 and ~ 1.197.

The sample is also limited to be brighter than M*+2 in R_c-band after k- and evolution corrections. We adopt $M^*_{R_c}$=-21.41 (Kodama & Arimoto 1997). The k- and evolution corrections are computed separately for galaxies of different spectral types. A galaxy spectral type for each galaxy is estimated based on the observed $B - R_c$ color using the model color computed from galaxy spectral energy distribution (Poggianti 1997). The R_c luminosity evolution is approximated as $M(z) = M(0) - zQ$ where Q=1.24 for red galaxies and Q=0.11 for blue galaxies (Lin et al. 1999). The red and blue galaxies are

separated using the gap in $B - R_c$ at each redshift. The appropriate k- and evolution corrections for the B and R_c magnitudes are then applied to the red and blue galaxies, respectively, based on their photometric redshift.

4.4 Identifying Galaxy Groups

Galaxy groups in the photometric redshift catalogs are identified using the *'Probability Friends-of-Friends'* algorithm (pFOF; see Chapter 2 for more details), a modified friends-of-friends group finding algorithm by considering photometric redshift probability density of each galaxy and group. The main idea of this algorithm is to treat the common photometric redshift space of the transversely connected galaxies as the group redshift space, which changes dynamically as new members are linked in. This updated group redshift is then used to search for more new members. Generally speaking, the group redshift is well confined by group members especially when the number of its members is large. The linking criteria are set by two parameters: $D0_{xy}$ and $P_{ratio,crit}$. The $D0_{xy}$ is the reference physical transverse linking length at z=0, which is scaled by $(1+z)^{-1}$. In practice, the linking length includes the adjustments for the completeness correction w_i and the varying galaxy number at different redshifts due to the apparent magnitude cutoff. The $P_{ratio,crit}$ is the criterion in determining friendship in redshift space, where P_{ratio} denotes the normalized total photometric redshift probability for galaxies in the same redshift space as other galaxies or a galaxy group. Galaxies must have their $P_{ratio} \geq P_{ratio,crit}$ in order to join into the group (see Chapter 2).

This algorithm has been tested using mock catalogs constructed from the Virgo Consortium Millennium Simulation (Springel et al. 2005), including the effects of using different linking criteria. The details of the tests are described in Chapter 2. As a compromise between the recovery and false detection rates, we adopt $P_{ratio,crit} = 0.37$ and $D0_{xy} = 0.25$ Mpc. With these parameters, the recovery rate is greater than 80% for mock groups of halo mass larger than $\sim 1.2 \times 10^{13} M_{\odot}$, and the false detection rate is less than 10% when a pFOF group contains ~ 8 members.

4.5 Galaxies And Groups In Cluster Redshift Space

For our attempt to study cluster environmental influence, we construct the samples of galaxies and groups in the same redshift space as the clusters. In using photometric redshift, the background galaxies and groups have a significant role in contaminating the sample. Such contamination, however, can be statistically estimated and corrected using a large control sample. We have described the control sample in §3.1 in Chapter 3, and we present the selection of the cluster galaxy sample in this section.

4.5.1 The Cluster As the Main Group

Loosely speaking, galaxy clusters can be treated as greatly rich galaxy groups. Because our sample is selected from the follow-up observations of the CNOC1 clusters with cluster redshift information available, we identify the galaxy group that coincides with the cluster center position as the main part of each cluster.

For a start, the center of a group is determined using group galaxies in the dense region where their local projected galaxy densities are above the mean local projected galaxy density of the group members. The center of this group is then calculated as the mean R.A. and Dec. of its members, weighted by their luminosity, completeness correction w_i, and local projected galaxy density. If a group has their members distributed in more than one dense region (i.e., clumps in the contours of the local projected density), only galaxies in the clump which has the largest galaxy number counts will be used. To designate the major galaxy aggregation of a cluster, each galaxy group is assigned a score based on (1) inversely the separations between the group centers and the cluster center, (2) the agreement of the group redshift compared to the cluster spectroscopic redshift, and (3) the group richness. The cluster main group, i.e., the major galaxy aggregation of a cluster, is determined as the galaxy group which has the best score.

The redshifts of our 16 major cluster galaxy aggregations ($z_{pFOF,cl}$) compared to the spectroscopic redshifts ($z_{spec,cl}$) has a dispersion of $\sigma(z_{pFOF,cl} - z_{spec,cl}) \sim 0.019$ (Fig. 4.2). The centers of our major cluster galaxy aggregations are on average $\sim 30''$ from the physical centers (i.e., where the cD galaxies are). The richness of CNOC1 clusters has been calculated in Yee & Ellingson (2003) using the B_{gc} parameter, which is the amplitude of the galaxy cluster center correlation function measured individually for each cluster. The B_{gc} parameter is calculated using an aperture of $0.5h_{50}^{-1}$Mpc to compute the net

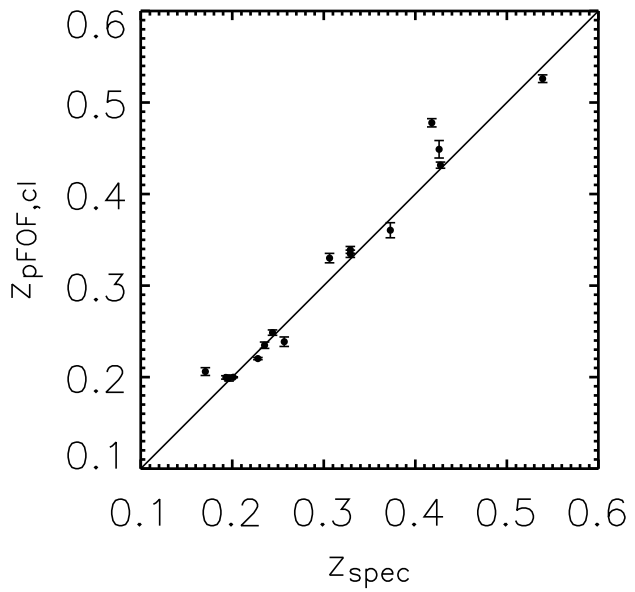

Figure 4.2: The comparison of the cluster redshift estimated by the pFOF algorithm and spectroscopically observed. The dispersion $\sigma(z_{pFOF,cl} - z_{zspec})$ is ~ 0.019.

excess counts of galaxies to a certain apparent magnitude and is then normalized by the luminosity function and the spatial distribution of cluster galaxies (Yee & López-Cruz 1999). It is interesting to compare the pFOF group richness N_{gal} of the cluster main groups to their B_{gc} values, because Yee & Ellingson (2003) show a correlation between the B_{gc} parameter and cluster virial radius. We plot the N_{gal} parameter and B_{gc} for the identified cluster main galaxy groups in Fig. 4.3. MS0906+11 is excluded in Fig. 4.3 due to unavailable B_{gc} information. In general, the larger N_{gal} corresponds to larger B_{gc}. The basic properties of our 16 identified cluster main groups are listed in Table 4.3.

4.5.2 Cluster Galaxies And Groups

In order to explore cluster environmental effects on the properties of individual galaxies and galaxy groups, we create samples of galaxies and groups in cluster redshift space using the photometric redshift probability densities of the cluster main groups. We follow the same idea used in determining the group membership in the pFOF algorithm. That is, the P_{ratio} of each galaxy or group to the redshift of the cluster main groups should satisfy $P_{ratio} \geq P_{ratio,crit}$, with the same $P_{ratio,crit}$ value used in the pFOF algorithm.

We select groups as those with richness $N_{gal} \geq 8$ (i.e., containing at least 8 net

Table 4.3: Properties of pFOF Determined CNOC1 Clusters ($D0_{xy} = 0.25Mpc$)

Cluster	R.A.(J2000)	Dec.(J2000)	$z_{pFOF,cl}$	N_{gal}	R^a_{200}	f_{red}
MS0302+16	03:19:33.78	17:28:29.50	0.4488 ± 0.0095	27.36 ± 2.40	1.20	0.698 ± 0.115
MS0302+16b	03:34:55.36	17:18:29.93	0.4778 ± 0.0045	135.02 ± 5.00	2.05	0.624 ± 0.053
MS0440+02	04:47:29.20	02:10:21.61	0.1989 ± 0.0032	29.49 ± 2.34	1.24	0.922 ± 0.057
MS0451+02	04:33:27.70	02:57:7.39	0.1998 ± 0.0005	208.46 ± 12.62	1.97	0.947 ± 0.080
MS0451-03	04:33:8.99	0-:0.:48.40	0.5260 ± 0.0041	222.12 ± 12.94	2.07	0.357 ± 0.052
MS0839+29	08:44:0.90	29:27:40.79	0.1996 ± 0.0018	70.37 ± 2.66	1.60	0.831 ± 0.056
MS0906+11	09:16:53.57	10:57:55.06	0.2060 ± 0.0042	36.54 ± 2.77	1.79^b	0.939 ± 0.045
MS1008-12	10:38:6.73	0-:39:52.22	0.3300 ± 0.0051	57.44 ± 3.62	1.94	0.933 ± 0.043
MS1231+15	12:28:37.58	15:26:59.07	0.2348 ± 0.0034	38.96 ± 2.49	1.30	0.907 ± 0.055
MS1231+15s	12:33:36.84	15:13:40.05	0.2486 ± 0.0029	60.75 ± 3.37	1.57	0.942 ± 0.041
MS1358+62	13:58:8.87	62:29:56.77	0.3294 ± 0.0039	45.10 ± 3.74	1.64	0.958 ± 0.031
MS1358+62s	13:53:30.65	62:19:5.19	0.3347 ± 0.0040	53.48 ± 3.67	1.50	0.932 ± 0.043
MS1455+22	14:17:54.90	22:19:54.15	0.2386 ± 0.0051	33.14 ± 2.39	2.24	0.903 ± 0.067
MS1512+36	15:35:36.41	36:36:23.11	0.3771 ± 0.0093	14.79 ± 1.97	1.21	0.915 ± 0.067
MS1621+26	16:53:52.16	26:34:52.09	0.4315 ± 0.0033	42.47 ± 3.02	1.39	0.884 ± 0.061
A2390	21:24:15.98	17:41:17.10	0.2202 ± 0.0012	126.67 ± 4.27	2.16	0.927 ± 0.036

[a] in *Mpc, h=0.7*

[b] using the single peak in the velocity dispersion in Borgani et al. (1999)

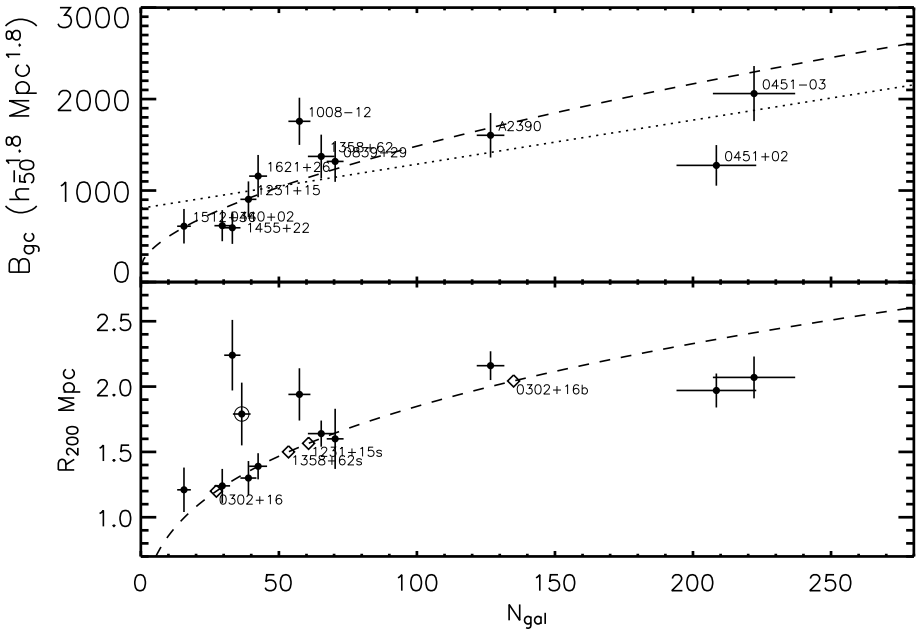

Figure 4.3: *Top:* The comparison between group richness N_{gal} and cluster richness B_{gc} for the identified cluster main groups. MS0906+11 is excluded from the plot because of the unavailable B_{gc} information. The dotted line is the linear fit result as $B_{gc} = 806.44 + 4.82\ N_{gal}$, and the dashed line is the result using a power-law fit as $B_{gc} = 164.66 + 83.33\ N_{gal}^{0.6}$. *Bottom:* The correlation between N_{gal} and the cluster virial radius R_{200}. The value for MS0906+11 is marked by open circle. The dashed curve is a $N_{gal} = 11.81 \times R_{200}^3$ power-law fit result. The clusters with unknown spectroscopically determined R_{200} are marked as the open diamonds, which their R_{200} values are estimated from the fit result.

members), and $N_{gz} \geq 5$, where N_{gz} is the number of the linked group members returned from the pFOF algorithm. As presented in Fig. 2.6 in Chapter 2, the fraction of false galaxy groups is less than 10% for $N_{gal} \geq 8$ computed using $M^{k,e}_{R_c,cut} = M^*_{R_c} + 2.0$. We have 89 cluster groups formed using $P_{ratio,crit} = 0.37$ and $D0_{xy} = 0.25\ Mpc$ satisfying our richness selection. Hereafter, by 'cluster galaxies' or 'cluster groups' we mean galaxies or groups which have been selected to be in the same redshift space as the clusters.

We present an example of the selection of cluster galaxies and groups in Fig. 4.4. The cluster galaxies exhibit an excess peak in the photometric redshift space in contrast to the field galaxy distribution. As illustrated in Fig. 4.4, our method in estimating galaxy redshift and selecting cluster galaxies eliminates efficiently most foreground and background galaxies.

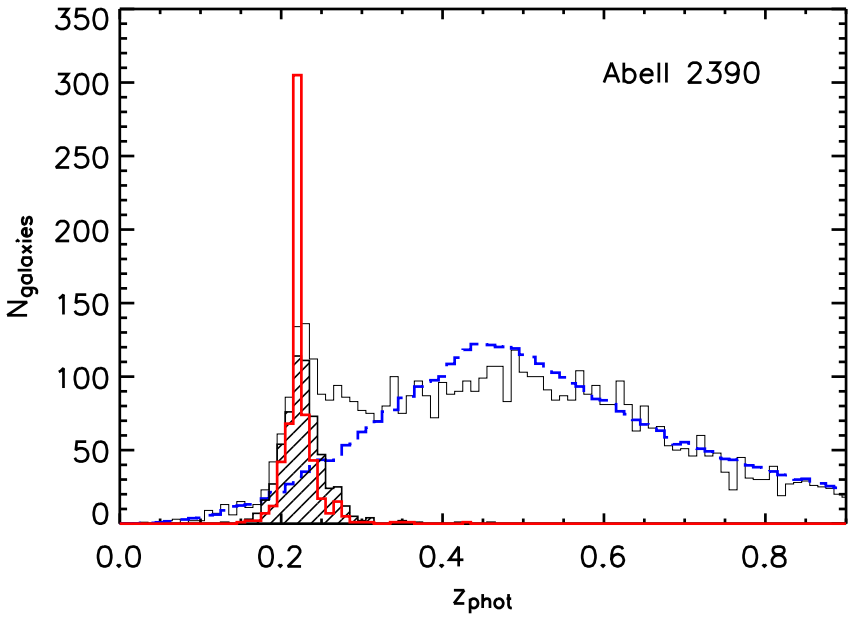

Figure 4.4: The photometric redshift distribution of all galaxies ($m_{R_c} < 22.80$) in the sample of Abell 2390 field (the thin open histogram). The background galaxy distribution estimated by the RCS CFHT patches (Hsieh et al. 2005) is shown in dashed histogram. The thick open histogram is for cluster galaxies selected using group redshift, and the hatched histogram is selected using photometric redshift of individual galaxies. The cluster galaxies show an excess in galaxy numbers in the photometric redshift space contrasted with the background galaxies.

We present an example of the sky locations in Fig. 4.5 for cluster galaxies and groups in the Abell 2390 field, a rich, large cluster at z=0.228. The cluster has a global elongation about -50^0 from the N-S axis from the central core spanning both sides of the cD galaxy (Abraham et al. 1996; Pierre et al. 1996). An infalling sub-component has been studied in Abraham et al. (1996) at the projected distance $\sim 650''$ to the cluster center. This infalling group is identified by the pFOF algorithms as well, marked by crosses in Fig. 4.5. Our pFOF algorithm also identifies two other groups. None of their members is within the original CNOC1 spectroscopically coverage, about 96″and 277″away from the spectroscopically identified infalling group. These two pFOF groups are marked as open squares and triangles in Fig. 4.5. We present the observed color-magnitude diagrams for all the cluster groups in Fig. 4.6. Galaxies in the cluster main group exhibit a well defined red-sequence, while galaxies in the infalling groups have less prominent red

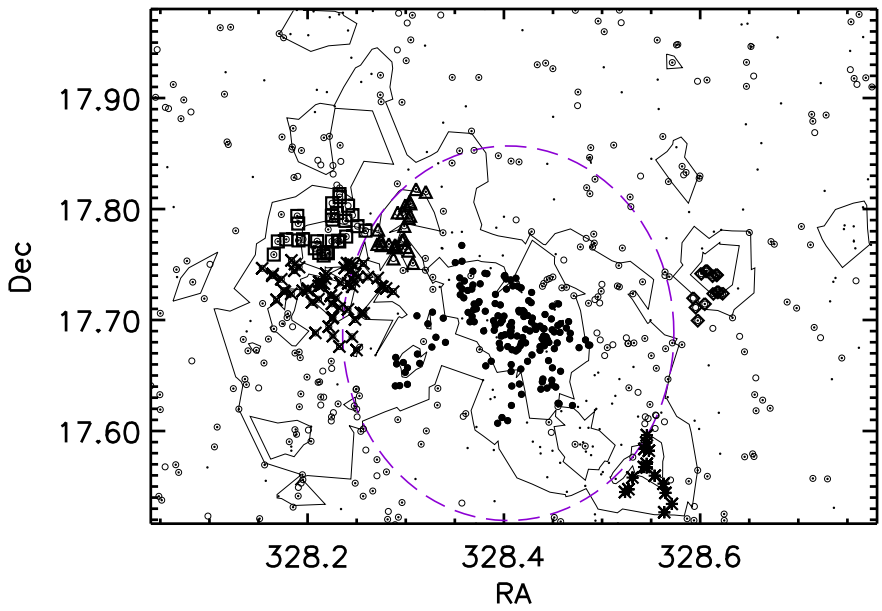

Figure 4.5: The map of Abell 2390 with groups found using the pFOF algorithm. Galaxies selected in the cluster redshift space using individual photometric redshift probability densities are plotted as the dots. Galaxies selected using group redshift are marked by open circles. The symbols in different shapes denote members of cluster groups with $N_{gal} \geq 8$. The cluster main group is marked in solid circles. The contours of the local projected galaxy density Σ_5 are calculated based the cluster galaxies (the dots) and are overlaid with levels of one-third and two-thirds of the Σ_5 distribution in the Abell 2390 sample. The dashed circle has a radius of 1 R_{200}.

sequences than that of the cluster main group.

4.6 The Environmental Parameters and f_{red}

We intend to study the color properties of cluster galaxies in different environments with the aim of unfolding the environmental effect on galaxy evolution. For this purpose, we demarcate the environmental effect into *local* and *global* regimes, and use a population fraction of red galaxies to quantify galaxy color properties as an indicator of their evolutionary stage. We have discussed the derivation of the environmental parameters and red galaxy fraction in Chapter 3. Here we provide a brief review.

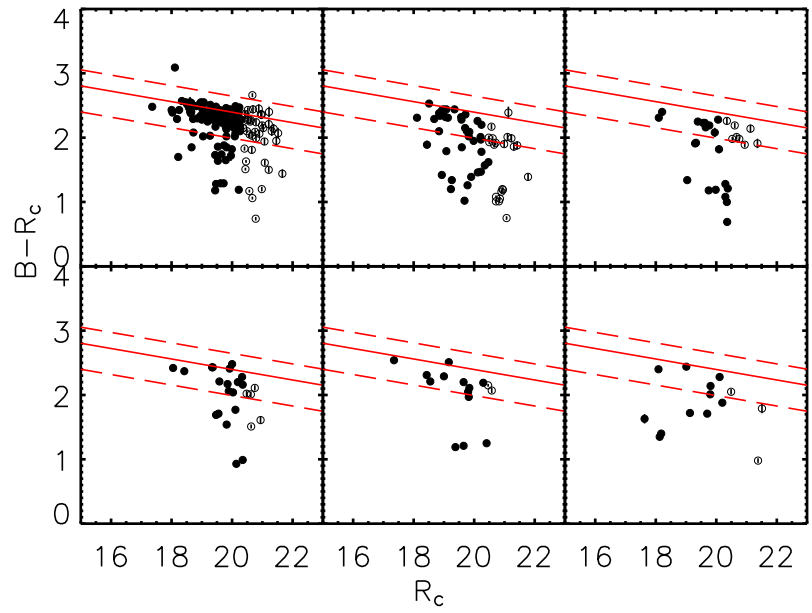

Figure 4.6: The observed color-magnitude diagram of galaxies ($M^{k,e}_{Rc} < M^* + 2.0$) in Abell 2390 cluster groups. The theoretical red-sequence is overlaid in each panel as the solid line, while the dashed lines define the region for cluster red galaxies. Panels on the top row from the left to the right are for the cluster main group, and the groups marked with crosses and squares, and the bottom panels are for the groups plotted in triangles, stars, and diamonds in Fig. 4.5. The galaxies fainter than $M^*_{Rc} + 1.5$ are marked by open circles.

4.6.1 Local Galaxy Environment: Local Galaxy Density

The local environment for individual galaxies is characterized using a projected nearest-neighbor density. For each galaxy, the local galaxy density is computed using a circular aperture as

$$\Sigma_5 = \frac{\sum_i^n w_i - \pi r_5^2 \Sigma_{bg}(z_{CL})}{\pi r_5^2}.$$

In this calculation, n is the n^{th} nearest galaxy such that the total completeness weight $\sum_i^n w_i \geq 5$, r_5 is the distance in Mpc to this 5^{th} nearest galaxy, and $\Sigma_{bg}(z_{CL})$ is the estimated background galaxy density in the cluster redshift space (equivalent to $\Sigma_{grp,bg}(z)$ in §2.6 in Chapter 2). In Fig. 4.5, we also overlay the contours of local galaxy density to illustrate the substructures in the cluster redshift space.

4.6.2 Global Cluster Environment: Cluster-Centric Radius

The global cluster environmental influence is delineated using the cluster-centric radius parameter, denoted as 'r_{CL}', in units of R_{200}. The R_{200} is the radius within which the mass density is 200 times the critical density. We use the values published in Carlberg et al. (1997) for our CNOC1 clusters, except for MS0906+11, which is overestimated due to the broad velocity dispersion composed of two merging clusters. Borgani et al. (1999) also analyze the velocity dispersions of CNOC1 clusters. In their work, they separate these two merging clusters in MS0906+11 and present their respectively velocity dispersions as 886 and 725 km/s. Scaled with the values in Carlberg et al. (1997), we use the value R_{200}=1.79 Mpc for MS0906+11. Yee & Ellingson (2003) have shown that there is a correlation between the cluster R_{200} and the B_{gc} parameter. For those clusters with unknown R_{200}, we estimate the values using a solution derived from the correlation between N_{gal} and R_{200}, assuming a power-law relation of $N_{gal} = kR_{200}^3$ (Fig. 4.3). The R_{200} value of each cluster is listed in Table 4.3 as well.

4.6.3 Red Galaxy Fraction: f_{red}

In a given environment or within a galaxy group, the red galaxy fraction, f_{red}, is computed using galaxies with $M_{R_c}^{k,e} < M_{R_c}^{*}+1.5$. The red galaxies are defined as galaxies with $B-R_c$ redder than the color which is halfway between E/S0 and Sc galaxies. The computation is conducted on the observed color-magnitude diagram, and therefore the boundaries to define the red galaxies are different for clusters at different redshifts. Because background galaxies play an important role in affecting the estimation of the true red galaxy fraction, especially in a sample of small size, we use a statistical inference to estimate the f_{red} probability function (see Chapter 3), as:

$$F(f_{red}|N_{red}, N_{tot}, \lambda_b, P_b)$$

$$\propto \sum_{N_{grp,red}}^{0\rightarrow N_{grp}} \frac{N_{grp}!}{(N_{grp}-N_{grp,red})!N_{grp,red}!} f_{red}^{N_{grp,red}} (1-f_{red})^{N_{grp}-N_{grp,red}}$$

$$\frac{N_{bg}!}{(N_{bg}-N_{bg,red})!N_{bg,red}!} P_b^{N_{bg,red}} (1-P_b)^{N_{bg}-N_{bg,red}} \frac{e^{-\lambda_b}\lambda_b^{N_{bg}}}{N_{bg}!},$$

where the symbol N denotes the number of objects indicated by the subscripts, with *'bg'* abbreviating for *background*, P_b is the portion of red galaxies contained in the background, and λ_b is the expectation number of the background galaxy assuming a Poisson

distribution. We then take the 68% central confidence interval of f_{red} probability function as the uncertainty of the estimated f_{red}.

4.7 Results

4.7.1 The Butcher-Oemler Effect

The trend of population fraction changing in galaxy cluster with redshift is generally referred to as the Butcher-Oemler effect, which was originally probed using the fraction of blue galaxies for 33 clusters up to $z \sim 0.5$ (Butcher & Oemler 1984). Instead of using the fraction of blue galaxies as the parameter to indicate evolutionary stage of galaxies, we use f_{red} where larger f_{red} reflects smaller blue galaxy fraction and vice versa. To probe the trend of f_{red} at different redshifts ('f_{red}-z' trend, for short) in each cluster, we compute f_{red} for each cluster by using (1) members of each cluster main group, all cluster galaxies (2) within $1R_{200}$, and (3) in 1-1.5R_{200}. The dependence of f_{red} on redshift for the clusters is plotted in Fig. 4.7, where the spectroscopic redshift of each cluster is used. We also overlay the results of linear fitting between f_{red} and redshift in Fig. 4.7. We find that in most cases f_{red} computed using galaxies in the cluster main group is larger than that using the other two selection methods. This is because our identified cluster main groups are in an area smaller by a factor ~ 4 than $1R_{200}$ for most cases, hence their averaged f_{red} is larger. We observe that the f_{red} computed in the above three ways all show decreasing trends with redshift. The values using galaxies in the cluster main groups show the most gentle gradient. Using all cluster galaxies within $1R_{200}$ or at $1 - 1.5R_{200}$, the gradient becomes steeper. It was shown in Ellingson et al. (2001) that the Butcher-Oemler effect is not significant within $0.5R_{200}$; our result of Fig. 4.7 is consistent with their work.

4.7.2 Cluster Galaxies

We examine the f_{red} parameter in different environments for the cluster galaxies. Only cluster galaxies of $M^{k,e}_{R_c} < M^*_{R_c} + 1.5$ are used. The cluster galaxies are classified into *bright* and *faint* if they are brighter or fainter than $M^{k,e}_{R_c} = M^*_{R_c} + 0.7$. This $M^*_{R_c} + 0.7$ separation gives roughly equal galaxy counts in the bright and faint subsamples. The local projected galaxy density is divided into three subsamples: *low*, *intermediate*, and *high* Σ_5 regions. The division in each Σ_5 bin is based on equal galaxy counts in these three

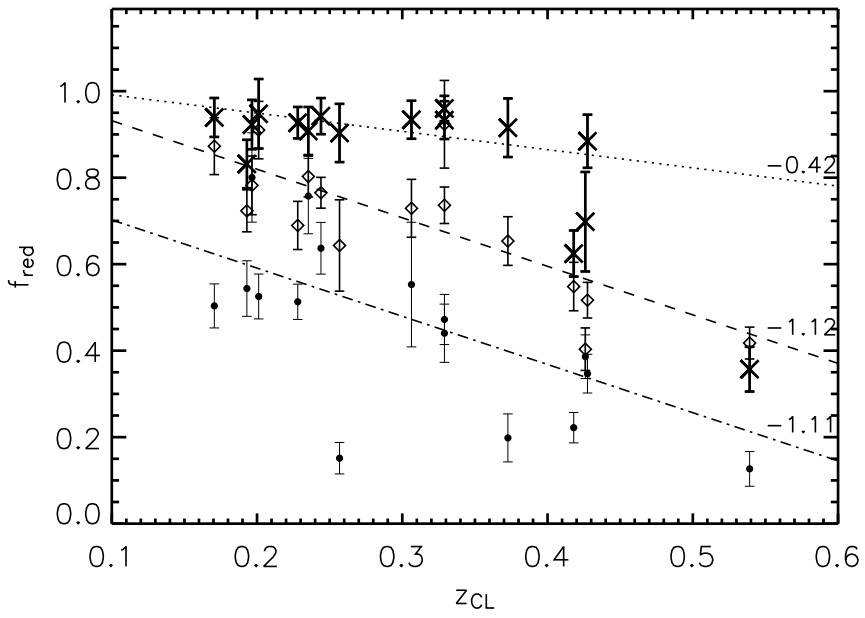

Figure 4.7: The red galaxy fractions for our 16 clusters using (1) galaxies in the identified cluster main groups, displayed with the thick crosses; cluster galaxies (2) within 1 R_{200}, presented as the open diamonds; and (3) at $1 - 1.5R_{200}$, plotted as the solid circles. A linear fitting between f_{red} and cluster spectroscopic redshift is performed, and has the slope indicated along the line. The negative slopes illustrate the Butcher-Oemler effect.

bins in each cluster to take into account the variations in the mean Σ_5 among different cluster fields. The cluster-centric radii are separated into *inner* : $0 \leq r_{CL} < 1.5R_{200}$ and *outer* : $1.5 \leq r_{CL} < 4.0R_{200}$ regions, since most clusters reach the edge of the science frame at $3 - 4R_{200}$. The cluster galaxies are binned into three redshift separations as $z < 0.30$, $0.30 \leq z < 0.40$, and $0.40 \leq z < 0.55$, and there are 8, 4, and 4 clusters in each redshift bin, respectively. We present f_{red} in each redshift bin in each environment for the bright and faint cluster galaxies in Fig. 4.8. We start with discussing the difference of f_{red}-z trends between the bright and faint cluster galaxies, then we probe the trends in regions of different local galaxy densities and cluster-centric radii.

The literature has shown that fractions of blue and red populations strongly depend on galaxy luminosity (e.g., Cucciati et al. 2006; Balogh et al. 2004): most bright galaxies are dominated by the red population. At higher redshift, red galaxies on average are brighter than the 'blue cloud' on the color-magnitude diagram (e.g., Cassata et al. 2007). With an attempt to investigate dependence of galaxy population fractions on environment

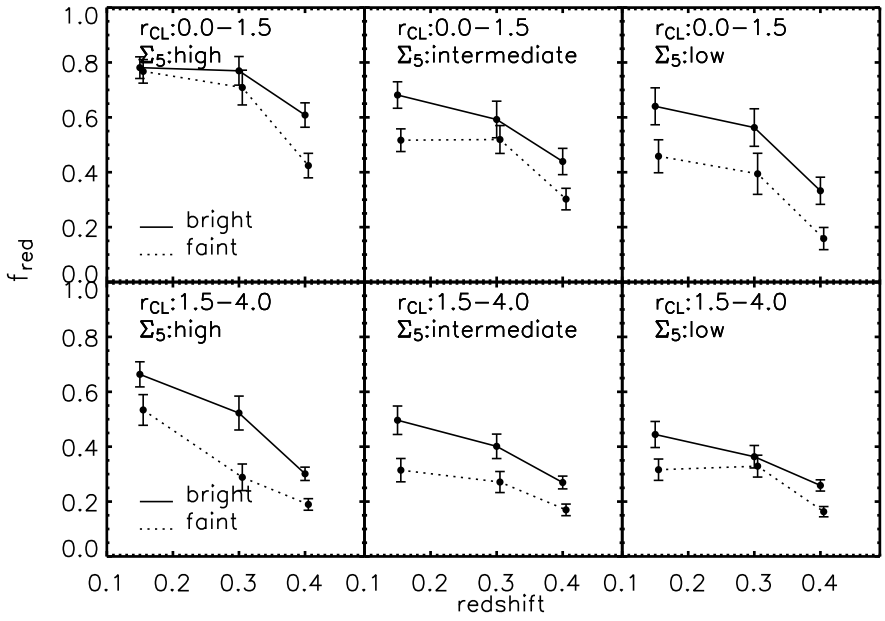

Figure 4.8: The red galaxy fraction for the cluster galaxies as a function of redshift in different environments as noted in each panel. The solid and dotted curves are for bright and faint cluster galaxies, respectively, which are separated at $M_{R_c}^{k,e} = M_{R_c}^{*} + 0.7$. In each panel, the bright cluster galaxies possess larger f_{red} than the faint subsample.

in our sample, we must acknowledge the strong relationship between galaxy populations and their luminosities. Fig. 4.8 shows the f_{red}-z trend in each environment for bright and faint cluster galaxies (separated at $M_{R_c}^{*} + 0.7$). In each panel, the f_{red} declines with increasing redshift, as expected from the Butcher-Oemler effect. This declining f_{red}-z trend is observed in the *inner* and *outer* regions and for all local galaxy density divisions. Within a fixed Σ_5 and r_{CL} location, the bright cluster galaxies (solid curves) possess larger f_{red} than that of the faint cluster galaxies (dotted curves). Our results of controlling galaxy local and global environments, therefore, provide evidence for 'down-sizing' star formation history in all environments, where the decreases in star formation with time are larger for bright galaxies than faint ones. We note that the f_{red}-z trends are steeper in the high Σ_5 bins compared to those in the low Σ_5 divisions. This indicates that evolution is quickened in regions of high galaxy density.

To probe the local environmental effect due to local galaxy density, we plot in Fig. 4.9 the f_{red} as a function of Σ_5 ('f_{red}-Σ_5' trend) at different redshift in each r_{CL}. The solid, dotted, and dashed curves in each panel in Fig. 4.9 represent the $0 \leq z < 0.30$,

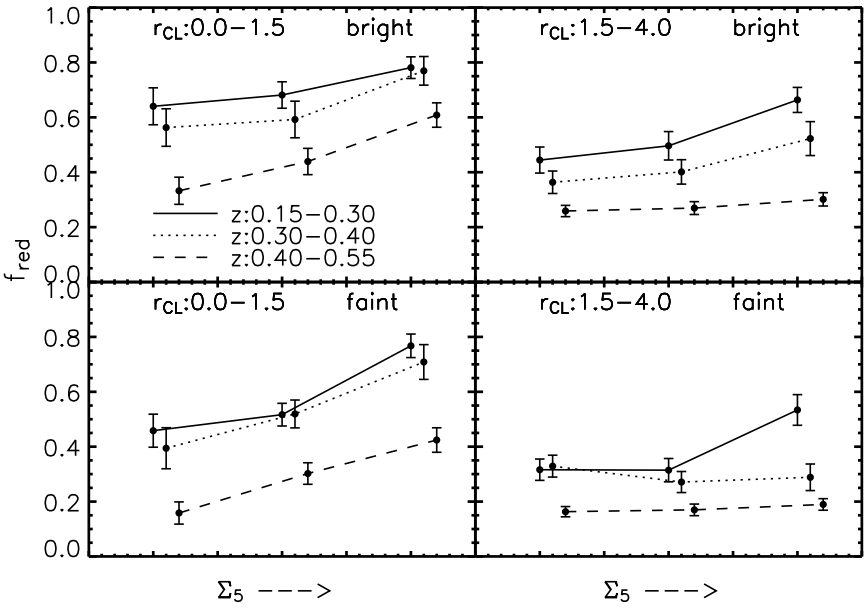

Figure 4.9: The red galaxy fraction for the cluster galaxies as a function of local galaxy density Σ_5 with r_{CL} controlled. The solid, dotted, and dashed curves represent the $z < 0.30$, $0.30 \leq z < 0.40$, and $0.40 \leq z < 0.55$ redshift bins, respectively. The bright and faint cluster galaxies at $0.40 \leq z < 0.55$ (the dashed curves) exhibit very weak dependence of their f_{red} on Σ_5 at the *outer* r_{CL} but not the *inner* r_{CL} locations, indicating the accelerated local density effect driven by the cluster environment.

$0.30 \leq z < 0.40$, and $0.40 \leq z < 0.55$ redshift bins. The bright and faint cluster galaxies show the increasing f_{red}-Σ_5 trends at a fixed redshift in both the *inner* and *outer* r_{CL} locations. In the *inner* r_{CL} region, the increasing f_{red}-Σ_5 trend is well observed at each redshift for both the bright and faint cluster galaxies. For the *outer* r_{CL} locations, the bright and faint cluster galaxies exhibit very weak f_{red}-Σ_5 trends at the $0.40 \leq z < 0.55$ redshift interval (the dashed curves). Compared with the stronger f_{red}-Σ_5 trends in the *inner* r_{CL} regions, this result indicates that the effect of local density on stellar population is accelerated by the cluster environment.

To further search for evidence of global cluster environmental influence, the local projected galaxy density Σ_5 is controlled and the f_{red}-z trends are explored in two different r_{CL} regions, graphed in Fig. 4.10. Here the solid and dotted curves represent the *inner* and *outer* r_{CL} divisions. In each Σ_5 bin, both the bright and faint cluster galaxies show declining f_{red}-z trends, and the f_{red} is always smaller in the *outer* r_{CL} regions. This

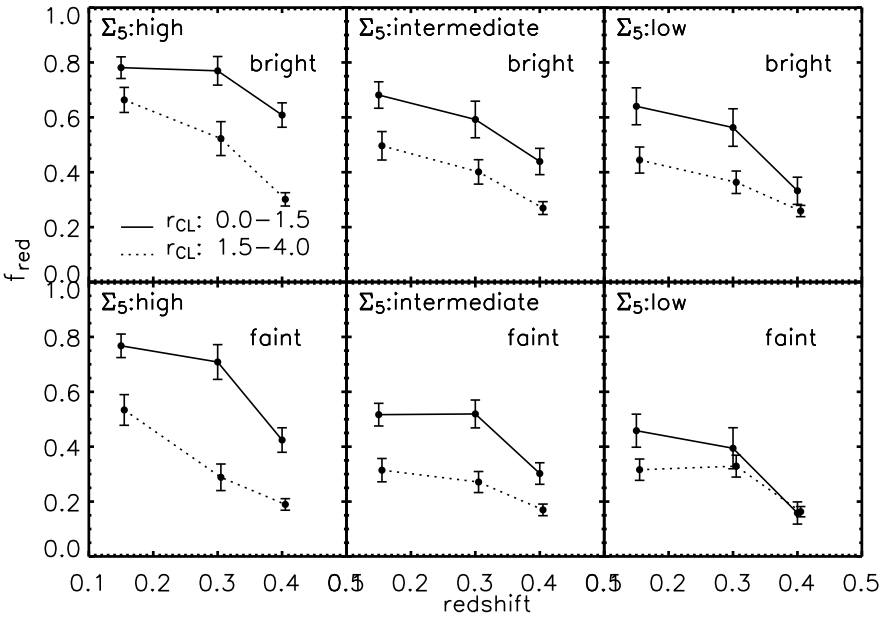

Figure 4.10: The red galaxy fraction for the cluster galaxies at different r_{CL} in each fixed Σ_5 bin. The solid and dotted curves represent the cluster galaxies in the *inner* : $0 \leq r_{CL} < 1.5R_{200}$ and *outer* : $1.5 \leq r_{CL} < 4.0R_{200}$, respectively. The cluster galaxies at the *inner* r_{CL} regions possess larger f_{red} than those at the *outer* r_{CL} locations.

demonstrates the global environmental influence related to r_{CL}.

4.7.3 Cluster Galaxies In Galaxy Groups

Differences Between Group and Non-Group Galaxies

To probe the role of galaxy groups in the evolution of cluster galaxies, we flag the cluster galaxies into 'group' and 'non-group' cluster galaxies according to the pFOF group finding results. The group cluster galaxies are the cluster galaxies classified as members of galaxy groups of $N_{gal} \geq 8$ and $N_{gz} \geq 5$ (see § 4.5.2), and the non-group cluster galaxies are those in poor galaxy groups of $N_{gal} < 3$ and $N_{gz} < 3$. The use of different cutoffs in N_{gal} and N_{gz} is to reduce the ambiguity in distinguishing the effect of group membership. The cluster galaxies associated with the cluster main groups are excluded from the group cluster galaxies, so that the environmental effect caused by galaxy groups can be fairly investigated. We have a total of 3,344 and 5,747 group and non-group cluster galaxies in the sample.

The environmental influence of galaxy groups will be discussed in a similar manner as

§ 4.7.2. The f_{red} for the group and non-group cluster galaxies are computed in different Σ_5 and r_{CL} bins with the same divisions in § 4.7.2, but the bright and faint magnitude subsamples are merged for better signal. The results are graphed in Fig. 4.11-4.13 with either Σ_5 or r_{CL} controlled.

Fig. 4.11 presents the f_{red}-z trends for the group and non-group cluster galaxies in a fixed environment, plotted as the solid circles connected by the solid and dotted lines, respectively. The cluster galaxies in the cluster main groups (hereafter 'main cluster galaxies' for short) are overlaid with the square symbols wherever their f_{red} are available. Fig. 4.11 shows a declining f_{red}-z trends with increasing redshift in all environmental panels for both the group and non-group cluster galaxies, but the group subsample exhibits a steeper f_{red}-z slope. At $0.40 \leq z < 0.55$, the group and non-group subsamples exhibit similar f_{red} in each Σ_5 division. However, the group cluster galaxies have their f_{red} increased more rapidly toward lower redshift compared with the non-group subsample. If the f_{red}-z trend for the non-group subclass can be considered as the outcome of natural evolution, the steeper f_{red}-z trend for the group subsample suggests that there are mechanisms associated with galaxy groups to quicken the evolution of the galaxies therein. In other words, the Butcher-Oemler effect is applicable to galaxy groups. One may naturally argue that galaxy groups are sites of high galaxy density and hence their member galaxies are at an advanced evolutionary stage caused by the local environmental effect of galaxy density. After controlling the local galaxy density Σ_5, the group and non-group cluster galaxies still show a difference in their f_{red}. This supports the 'preprocessing' scenario, because group galaxies exhibit a more advanced evolutionary stage in a given local galaxy density environment.

Fig. 4.11, however, shows another interesting aspect. In the intermediate Σ_5 bins, the main cluster galaxies exhibit differentiated f_{red} from the group ones at all redshifts. In the high Σ_5 locations, the f_{red} possessed by the group cluster galaxies are smaller than that of the main cluster galaxies at $0.30 \leq z < 0.40$ and $0.40 \leq z < 0.55$, but both the group and main cluster galaxies exhibit similar f_{red} at $z < 0.30$. This shows that the differences in f_{red} between the group and main cluster galaxies depend on Σ_5 and redshift. The main cluster galaxies have their f_{red} reached ~ 1 at $z < 0.30$ in the intermediate Σ_5 bin, but this occurs at $0.30 \leq z < 0.40$ in the high Σ_5 division. For the group cluster galaxies, $f_{red} \sim 1$ is only observed at $z < 0.30$ in the high Σ_5 bin. The non-group cluster galaxies, however, possess f_{red} significantly less than 1 in all environments. The differences among group, non-group, and main cluster galaxies reflect that galaxies in groups are still relatively young compared with those in galaxy clusters and the non-

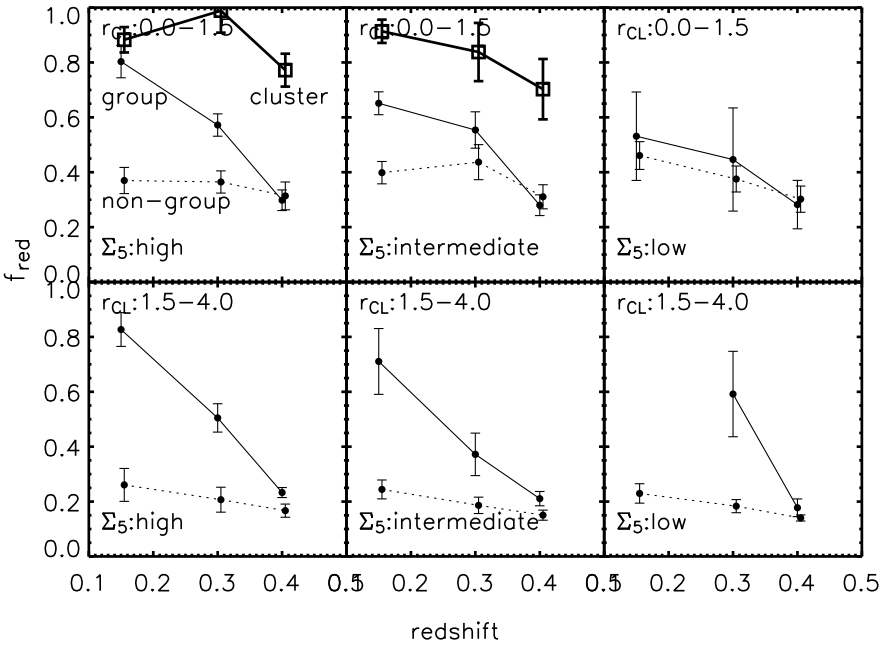

Figure 4.11: The red galaxy fraction for the group and non-group cluster galaxies as a function of redshift in different environments, as notated in each panel. The solid and dotted curves with solid circles are for the group and non-group cluster galaxies, respectively. The red galaxy fraction for the cluster galaxies in the cluster main groups are overlaid as the open squares for a comparison. The group cluster galaxies exhibit steeper f_{red}-z trends than the non-group subsample.

group galaxies are at the youngest evolutionary stage. In other words, the times that galaxies reach their near-final evolutionary stage of $f_{red} \sim 1$ depend on the environment.

The Cluster Environmental Influence

To investigate the cluster environmental influence on properties of group and non-group subsamples, we study the f_{red}-z trends at different r_{CL} with the local projected galaxy density Σ_5 controlled. We replot Fig. 4.11 in Fig. 4.12, where the group and non-group cluster galaxies at the *inner* and *outer* r_{CL} locations are plotted in solid circles connected by the solid and dotted lines. The f_{red}-z trends for the main cluster galaxies are overlaid as the squares in the panels associated with the group cluster galaxies. Fig. 4.12 shows that the differences in f_{red} between the *inner* and *outer* r_{CL} regions are more apparent for the non-group cluster galaxies. Within the measurement uncertainties, we find no apparent difference in high Σ_5 regions between the group cluster galaxies at the *inner*

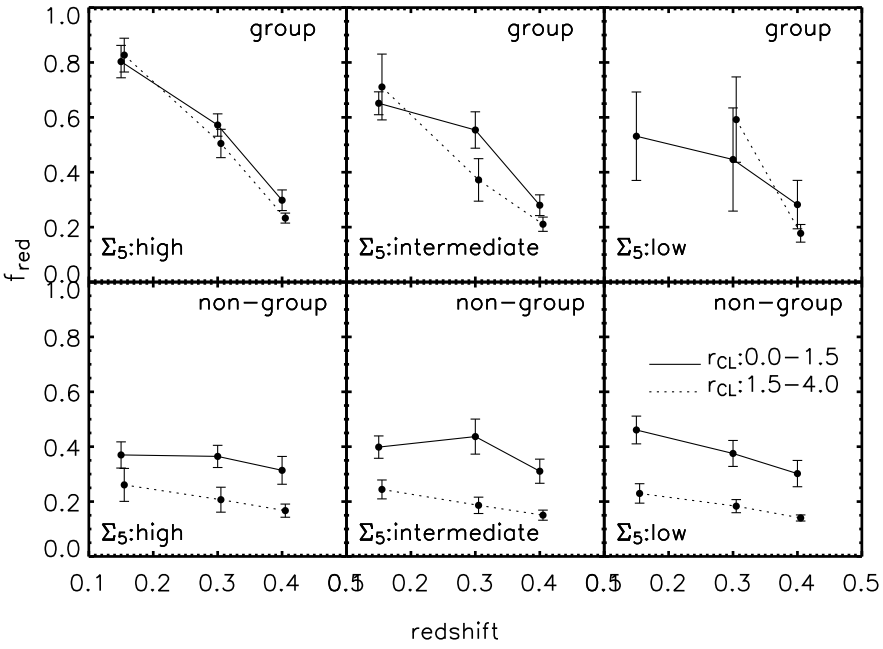

Figure 4.12: The red galaxy fraction for the group and non-group cluster galaxies as a function of redshift in different r_{CL} locations in a fixed Σ_5 bin. The solid and dotted curves represent the *inner* : $0 \leq r_{CL} < 1.5R_{200}$ and *outer* : $1.5 \leq r_{CL} < 4.0R_{200}$ devisions, respectively. The f_{red} values for the main cluster galaxies are marked with the open squares in the panel with the group cluster galaxies. The group cluster galaxies have similar f_{red} at the *inner* and *outer* r_{CL} regions, but the non-group cluster galaxies at the *inner* r_{CL} regions exhibit apparently larger f_{red} than that at the *outer* r_{CL} locations.

and *outer* r_{CL} locations. If the regions of high galaxy density for the group subsample correspond to the cores of groups, this result suggests that the central regions of galaxy groups still maintain their own properties as they fall into clusters, whereas the cluster potential produces a strong effect on non-group galaxies.

The Local Environmental Effect

As the properties within central regions of galaxy groups are not largely affected by the cluster environmental influence, it is interesting to examine whether the local projected galaxy density Σ_5 causes any changes in the group galaxies. To do this, the cluster r_{CL} parameter is controlled and we plot the f_{red} as a function of Σ_5 for both group and non-group cluster galaxies in Fig. 4.13 at each redshift interval. Generally speaking, both group and non-group cluster galaxies exhibit weak dependence of their f_{red} on Σ_5 in a

fixed r_{CL} region. At $z < 0.30$ (perhaps $0.30 \leq z < 0.40$ as well) in the *inner* r_{CL} bin, the group subsample may have larger f_{red} toward higher Σ_5, but the increases are within the measurement errors. The weak dependence in f_{red} on Σ_5 exhibited by the group cluster galaxies indicates that the evolution of group cluster galaxies does not depend strongly on the local projected galaxy density. In tandem with the results in Fig. 4.12 that the cluster environment is observed to have significant influence on the non-group cluster galaxies, but not on the group ones, both the cluster r_{CL} and local Σ_5 are observed to have little influence on group galaxies. This suggests that star formation in group galaxies is truncated regardless of their r_{CL} and Σ_5 environments. In other words, the f_{red} has a much stronger dependence on group and non-group classification than local density. Therefore, the dependence of f_{red} on Σ_5 is a reflection of a dependence on group halo mass, as group galaxies are embedded in haloes of larger mass.

Consequently, the results of Fig. 4.11 to Fig. 4.13 suggest that the properties of galaxies in groups are strongly affected by being in a group. Such group influence is intrinsic to the galaxy groups themselves and could be the dominant influence on the properties of galaxies when they are sited in the large-scale cluster environment. These results can be taken as evidence of 'pre-processing' in galaxy groups, and its occurrence is independent of the local density and global environments of the groups.

4.8 Discussion and Conclusion

We have investigated the environmental effects on the properties of cluster galaxies using individual galaxies and those in galaxy groups. We have used local projected galaxy density Σ_5 and cluster-centric radii r_{CL} in units of R_{200} as the proxies of local and global environment, and adopted red galaxy fraction f_{red} as the measurement of galaxy color properties.

Starting with the f_{red} in the cluster main groups, we observe that these f_{red} have weaker declining trends with increasing redshift compared to those using the cluster galaxies within $1R_{200}$ or at $1.0 - 1.5R_{200}$. We note that the projected radius of the cluster main groups is $\sim 55\%$ of the R_{200} on average. Therefore, this result is consistent with what is presented in Ellingson et al. (2001) that the Butcher-Oemler effect is largely absent within $0.5R_{200}$.

Using individual cluster galaxies in Fig. 4.8, we find that bright cluster galaxies possess larger f_{red} than faint cluster galaxies. There are growing numbers of studies showing that galaxy evolution has a dependence on galaxy luminosity (mass). The star

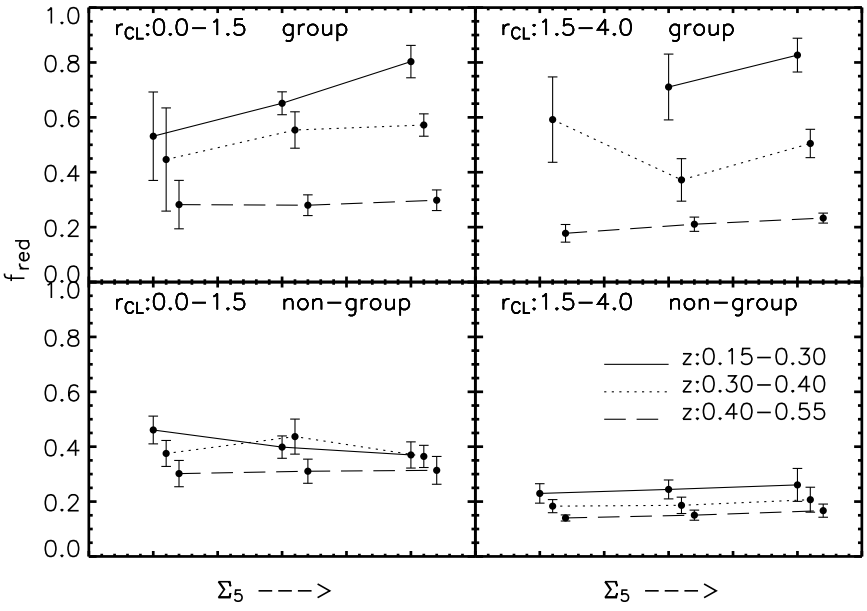

Figure 4.13: The red galaxy fraction for the group and non-group cluster galaxies as a function of Σ_5 at different redshift with r_{CL} controlled. The solid, dotted, and dashed curves represent the $z < 0.30$, $0.30 \leq z < 0.40$, and $0.40 \leq z < 0.55$ redshift bins, respectively. Both the group and non-group cluster galaxies exhibit weak trends of their f_{red} on Σ_5.

formation takes place and is also completed earlier in massive galaxies, but less massive galaxies may still have their star formation ongoing (e.g., Sheth et al. 2006; De Lucia et al. 2006). This evolutionary scenario is generally referred to as 'down-sizing' (Faber et al. 1995; Cowie et al. 1996). Our results by investigating f_{red} for galaxies of different luminosities in a fixed environment is consistent with the galaxy down-sizing evolutionary scenario, and further show that the down-sizing effect is found in all galaxy environments.

As galaxy density increases toward the cluster central region, a proper way to investigate local and global environmental influence is to control one of them, then probe galaxy properties as a function of the other environmental variable. Numerous studies have found that there are fewer star forming galaxies in regions of high galaxy density (e.g., Mateus et al. 2007; Doyle & Drinkwater 2006; Gómez et al. 2003). Along the natural evolutionary path, galaxy evolution can be accelerated in dense environment over a short time scale (e.g., Balogh et al. 2004; Carretero et al. 2007). After controlling r_{CL}, we find that the f_{red} generally increases toward higher Σ_5 regions, but such local

environment driven evolution may be accelerated under the cluster environment (Fig. 4.9), in that the changes in f_{red} due to Σ_5 is more apparent within the *inner* r_{CL} regions compared with the *outer* r_{CL} locations. In other words, the results of Fig. 4.9 suggest that the strength of the local environmental effect may be a function of cluster-centric radii.

To investigate global environmental influence, we control Σ_5 and observe that f_{red} is larger for cluster galaxies in the *inner* r_{CL} regions compared to those in the *outer* r_{CL} locations (Fig. 4.10). It has been known that galaxy clusters host red and old elliptical galaxies in their cores. One example of cluster environmental influence on galaxy population properties is the build-up of red sequence galaxies (Tanaka et al. 2005; de Lucia et al. 2007). The literature has discussed possible mechanisms active in galaxy clusters in transforming galaxy morphology and star formation activities (e.g., ram-pressure stripping: Gunn & Gott (1972); Abadi et al. (1999); galaxy-galaxy or galaxy-cluster interaction: Aguilar & White (1985); Merritt (1984); Gallagher & Ostriker (1972)). Perhaps the main argument about cluster environmental influence is due to the existence of dense galaxy aggregations in clusters, hence galaxy evolution is still driven mainly by local environmental impact. Our study probes f_{red} in different r_{CL} within three controlled Σ_5 bins, therefore any changes in f_{red} in a fixed Σ_5 division can reflect the influence of cluster environment. After controlling Σ_5, we find that the cluster galaxies have steeper trends between their f_{red} and redshift in the *high* Σ_5 bin. In other words, galaxy evolution is quickened in the high galaxy density regions. Based on our results of Fig. 4.8 to Fig. 4.10, we conclude that the evolution sequence starts from bright galaxies in high galaxy density regions, and global cluster environment enhances their evolution especially at high redshift.

Since galaxy groups are sites of relatively higher galaxy density compared with the field, the local and global environmental influence can also be studied using cluster galaxies in groups. Recent works have shown that galaxy groups can 'pre-process' galaxies therein, as star formation is slower or truncated in group galaxies before the group enters into a main cluster (e.g., Cortese et al. 2006; Boselli & Gavazzi 2006). We also have discussed the f_{red}-z trends for both group and non-group cluster galaxies by controlling either Σ_5 or r_{CL}. The subsample of the group cluster galaxies has the galaxies in the cluster main groups excluded, and can offer a fair study about the effect of galaxy groups. We note that different Σ_5 regions for the group galaxies may be related to the projected distances from the group centers. Group galaxies located in high Σ_5 regions are possibly at the group cores, while those in the sites of low Σ_5 are perhaps at large group-centric

radii. In contrast, the non-group galaxies in high Σ_5 regions are likely galaxies in compact but poor groups which are not rich enough to satisfy our group definition. Our results (Fig. 4.11) show that the group cluster galaxies have steeper gradients between their f_{red} and redshift than the non-group cluster galaxies, after we control for Σ_5. This is evidence for pre-processing in galaxy groups. Furthermore, we find that the difference caused by the pre-processing becomes more apparent at lower redshift. The cluster environment primarily impacts on the non-group cluster galaxies, while galaxies in the cluster groups show minor changes in their f_{red} at different r_{CL} locations, especially the group galaxies in high Σ_5 regions (i.e., the group cores, Fig. 4.12). We also find that the group galaxies exhibit weak or non-existent dependence of their f_{red} on Σ_5 (Fig. 4.13), indicating the weak role of local projected galaxy density in affecting the evolution of the group cluster galaxies. Based on these results, we conclude that the properties of galaxies in groups are strongly affected by their group environment. In the context of halo models (e.g., Cooray & Sheth 2002; van den Bosch et al. 2007), our conclusion can be interpreted as the dependence of galaxy properties on halo mass. Rich galaxy groups correspond to haloes of large mass, while non-group galaxies are in less massive haloes. A massive halo hosts more galaxies, where galaxy mergers are more common (likely the most dominant mechanism) compared with a halo of less mass. Therefore, galaxies in groups have their properties largely more affected than non-group galaxies.

Our analyses and interpretations are suggestive, based on a small-size sample of 16 clusters and 78 cluster groups. In the next two chapters we will use the *Red-sequence Cluster Survey* follow-up catalogs (RCS; Hsieh et al. 2005). With 33.6 deg^2 area in the sky, the sample size will increase by a factor of ~ 10 and provide a statistically significant sample. With the RCS sample, we will extend the study of cluster environmental influence to large cluster-centric radii. We will further control group and non-group cluster galaxies by their luminosities, and will be able to study properties of galaxy groups in details.

We summarize the results using the CNOC1 sample as follows.

• Bright galaxies possess larger f_{red} compared with faint galaxies in a fixed environment (Fig. 4.8). This is evidence for supporting 'down-sizing' star formation history.

• Galaxy evolution is quickened in high galaxy density regions. The f_{red} decreases with higher redshift faster in high Σ_5 regions than that in low Σ_5 locations with r_{CL} controlled (Fig. 4.10). Galaxy evolution is also accelerated in the cluster virialized region. The cluster galaxies have steeper f_{red}-Σ_5 trends in the *inner* r_{CL} regions compared with those in the *outer* r_{CL} locations (Fig. 4.9). That is, the local environmental effect is relatively stronger in the *inner* r_{CL} than the *outer* r_{CL} locations.

• The Butcher-Oemler effect is observed in the *inner* (larger than the cores) and *outer* r_{CL} locations and for all Σ_5 regions (Fig. 4.10).

• Global cluster environment is primarily effective on the non-group cluster galaxies. Group galaxies have less significant changes in their f_{red} compared with non-group galaxies when they are located at different cluster-centric radii, especially those in regions of high Σ_5 (Fig. 4.12).

• Galaxy groups pre-process galaxies therein, and exhibit the Butcher-Oemler effect. Group cluster galaxies exhibit steeper f_{red}-z trends than non-group cluster galaxies after controlling Σ_5 (Fig. 4.11). Both the group and non-group cluster galaxies have similar f_{red} at $0.40 \leq z < 0.55$, but the f_{red} is larger for the group subsample at $z < 0.30$. Both r_{CL} and Σ_5 have weak influence on group galaxies. Properties of galaxies in groups are strongly affected by their group environment, and such influence is intrinsic within galaxy groups (Fig. 4.12 and Fig. 4.13). The group and non-group separation produces a much more significant f_{red} differentiation than Σ_5 and r_{CL}. Whether a galaxy belongs to a sufficiently massive halo (i.e., group environment) is a dominant factor that determines the star formation history.

References

Abadi, M. G., Moore, B., & Bower, R. G. 1999, MNRAS, 308, 947

Abell, G. O., Corwin, H. G., & Olowin, R. P. 1989, ApJS, 70, 1

Abraham, R. G., et al. 1996, ApJ, 471, 694

Adami, C., Biviano, A., Durret, F., & Mazure, A. 2005, A&A, 443, 17

Aguilar, L. A. & White, S. D. M. 1985, ApJ, 295, 374

Andreon, S., Lobo, C., & Iovino, A. 2004, MNRAS, 349, 889

Andreon, S., Quintana, H., Tajer, M., Galaz, G., & Surdej, J. 2006, MNRAS, 365, 915

Balogh, M. L., Baldry, I. K., Nichol, R., Miller, C., Bower, R., & Glazebrook, K. 2004, ApJ, 615, L101

Bekki, K. 1999, ApJ, 510, L15

Borgani, S., Girardi, M., Carlberg, R. G., Yee, H. K. C., & Ellingson, E. 1999, ApJ, 527, 561

Boselli, A. & Gavazzi, G. 2006, PASP, 118, 517

Butcher, H. & Oemler, A. 1984, ApJ, 285, 426

Caldwell, N. & Rose, J. A. 1997, AJ, 113, 492

Carlberg, R. G., Yee, H. K. C., Ellingson, E., Abraham, R., Gravel, P., Morris, S., & Pritchet, C. J. 1996, ApJ, 462, 32

Carlberg et al. 1997, ApJ, 485, L13+

Carretero, C., Vazdekis, A., & Beckman, J. E. 2007, MNRAS, 1506

Cassata, P., et al. 2007, ArXiv Astrophysics e-prints

Cortese, L., Gavazzi, G., Boselli, A., Franzetti, P., Kennicutt, R. C., O'Neil, K., & Sakai, S. 2006, A&A, 453, 847

Cowie, L. L., Songaila, A., Hu, E. M., & Cohen, J. G. 1996, AJ, 112, 839

Cucciati, O., et al. 2006, A&A, 458, 39

D'Agostini, G. 2004, ArXiv Physics e-prints

David, L. P., Forman, W., & Jones, C. 1999, ApJ, 519, 533

de Lucia, G., et al. 2007, MNRAS, 374, 809

De Lucia, G., Springel, V., White, S. D. M., Croton, D., & Kauffmann, G. 2006, MNRAS, 366, 499

De Propris, R., Stanford, S. A., Eisenhardt, P. R., & Dickinson, M. 2003, ApJ, 598, 20

Domínguez, M., Muriel, H., & Lambas, D. G. 2001, AJ, 121, 1266

Doyle, M. T. & Drinkwater, M. J. 2006, MNRAS, 372, 977

Dressler, A. 1980, ApJ, 236, 351

Dressler et al. 1997, ApJ, 490, 577

Eke et al. 2004, MNRAS, 348, 866

Ellingson, E., Lin, H., Yee, H. K. C., & Carlberg, R. G. 2001, ApJ, 547, 609

Faber, S. M., Trager, S. C., Gonzalez, J. J., & Worthey, G. 1995, in IAU Symp. 164: Stellar Populations, ed. P. C. van der Kruit & G. Gilmore, 249–+

Fujita, Y. 2004, PASJ, 56, 29

Gallagher, J. S. & Ostriker, J. P. 1972, AJ, 77, 288

Gladders, M. D. & Yee, H. K. C. 2005, ApJS, 157, 1

Gómez, P. L., et al. 2003, ApJ, 584, 210

Goto, T., Yamauchi, C., Fujita, Y., Okamura, S., Sekiguchi, M., Smail, I., Bernardi, M., & Gomez, P. L. 2003, MNRAS, 346, 601

Gunn, J. E. & Gott, J. R. I. 1972, ApJ, 176, 1

Helsdon, S. F. & Ponman, T. J. 2003a, MNRAS, 339, L29

—. 2003b, MNRAS, 340, 485

Hogg et al. 2003, ApJ, 585, L5

Hsieh, B. C., Yee, H. K. C., Lin, H., & Gladders, M. D. 2005, ApJS, 158, 161

Kodama, T. & Arimoto, N. 1997, A&A, 320, 41

Kodama, T. & Bower, R. G. 2001, MNRAS, 321, 18

Kodama, T., Smail, I., Nakata, F., Okamura, S., & Bower, R. G. 2001, ApJ, 562, L9

Krick, J. E., Bernstein, R. A., & Pimbblet, K. A. 2006, AJ, 131, 168

Landolt, A. U. 1992, AJ, 104, 340

Lin, H., Yee, H. K. C., Carlberg, R. G., Morris, S. L., Sawicki, M., Patton, D. R., Wirth, G., & Shepherd, C. W. 1999, ApJ, 518, 533

Mamon, G. A. 2000, in ASP Conf. Ser. 197: Dynamics of Galaxies: from the Early Universe to the Present, ed. F. Combes, G. A. Mamon, & V. Charmandaris, 377–+

Margoniner, V. E., de Carvalho, R. R., Gal, R. R., & Djorgovski, S. G. 2001, ApJ, 548, L143

Mateus, A., Sodré, L., Cid Fernandes, R., & Stasińska, G. 2007, MNRAS, 374, 1457

Merritt, D. 1984, ApJ, 276, 26

Metevier, A. J., Romer, A. K., & Ulmer, M. P. 2000, AJ, 119, 1090

Mulchaey, J. S. & Zabludoff, A. I. 1998, ApJ, 496, 73

Nuijten, M. J. H. M., Simard, L., Gwyn, S., & Röttgering, H. J. A. 2005, ApJ, 626, L77

Oemler, A. J. 1974, ApJ, 194, 1

Pierre, M., Le Borgne, J. F., Soucail, G., & Kneib, J. P. 1996, A&A, 311, 413

Pimbblet, K. A. 2003, Publications of the Astronomical Society of Australia, 20, 294

Poggianti, B. M. 1997, A&AS, 122, 399

Sheth, R. K., Jimenez, R., Panter, B., & Heavens, A. F. 2006, ApJ, 650, L25

Smail, I., Edge, A. C., Ellis, R. S., & Blandford, R. D. 1998, MNRAS, 293, 124

Solanes, J. M., Salvador-Solé, E., & González-Casado, G. 1999, A&A, 343, 733

Springel et al. 2005, Nature, 435, 629

Tanaka, M., Kodama, T., Arimoto, N., Okamura, S., Umetsu, K., Shimasaku, K., Tanaka, I., & Yamada, T. 2005, MNRAS, 362, 268

Tran, K.-V. H., van Dokkum, P., Illingworth, G. D., Kelson, D., Gonzalez, A., & Franx, M. 2005, ApJ, 619, 134

Treu, T., Ellis, R. S., Kneib, J., Dressler, A., Smail, I., Czoske, O., Oemler, A., & Natarajan, P. 2003, ApJ, 591, 53

Tully, R. B. & Fisher, J. R. 1987, Nearby galaxies Atlas (Cambridge: University Press, 1987)

Ulmer, M. P. & Cruddace, R. G. 1982, ApJ, 258, 434

van den Bosch, F. C., et al. 2007, MNRAS, 376, 841

Wilman, D. J., Balogh, M. L., Bower, R. G., Mulchaey, J. S., Oemler, A., Carlberg, R. G., Morris, S. L., & Whitaker, R. J. 2005, MNRAS, 358, 71

Yamauchi, C. & Goto, T. 2004, MNRAS, 352, 815

Yee, H. K. C. 1991, PASP, 103, 396

Yee, H. K. C., Ellingson, E., & Carlberg, R. G. 1996, ApJS, 102, 269

Yee, H. K. C. & López-Cruz, O. 1999, AJ, 117, 1985

Chapter 5

Individual Galaxies in Optically Selected Clusters: the RCS Sample

5.1 Introduction

With the goal to investigate galaxy properties both in local and global environments, we have discussed in Chapter 4 the galaxy population fraction as a function of only one environmental parameter with the others controlled. The results in Chapter 4 have revealed that the Butcher-Oemler effect is observed at both *inner* and *outer* cluster-centric radii (r_{CL}) locations and in regions of different local projected galaxy densities, while it is stronger in high galaxy density regions. We have also observed that both the Butcher-Oemler effect and the local galaxy density effect are more pronounced within the *inner* r_{CL} location. Meanwhile, bright galaxies possess larger red population fractions than faint galaxies within a fixed environment. However, the CNOC1 sample is small in size, containing only 16 clusters. Furthermore, the sample only extends to $\sim 3-4$ cluster virial radii, hence the investigation of cluster environmental influence is limited to the infall regions, and not contrasted by the field.

At redshift $z \sim 0.3-0.6$, the Red-sequence Cluster Survey (RCS; Gladders & Yee 2005) offers an excellent opportunity to explore such environmental dependence on galaxy properties in space associated with galaxy groups and clusters. The RCS is an imaging survey in R_c and z' to search for galaxy clusters up to $z \sim 1.0$. The survey covers 92 deg^2 conducted using with the CFHT 3.6m and CTIO 4m telescopes. Follow-up imaging in B and V is available for a total of ~ 40 deg^2 from both the North (CFHT) and South (CTIO) patches. The four-color photometry enables photometric redshift estimation. The large

sky area of the survey allows us to study galaxies in different environments from galaxy cluster core into the field. Furthermore, the RCS clusters are selected optically, offering a comparison to the X-ray selected clusters from CNOC1. In this chapter, we use the RCS data, aided with photometric redshifts, to investigate galaxy properties in various environments over a range of redshifts. We focus on individual galaxies in cluster redshift space in this chapter, and will concentrate on galaxy groups in the next chapter. The structure of this chapter is as follows. We present the data in § 5.2 and the photometric-redshift sample in § 5.3. We provide a brief review of the measurements of environment and population fraction in § 5.4. The results are presented in § 5.5, followed by the discussion in § 5.6. Finally we summarize our results in § 5.7. We adopt a flat cosmology with $\Omega_m = 0.30$, $\Omega_\Lambda = 0.70$, and $H_0 = 70$ km/s/Mpc.

5.2 Data

The primary goal of the RCS is to measure Ω_m and σ_8 using the cluster mass function (Gladders & Yee 2005). The survey covers 22 widely separated patches in total in the Northern and Southern sky. The observations were carried out during May 1999 to Jan 2001. The imaging of the ten Northern patches was conducted using the CFHT 12K camera on the 3.6m telescope. The camera has $12k \times 8k$ pixels in total made of twelve $2k \times 4k$ CCDs, and gives a 42×28 arcmin^2 field of view with $0.206''$ per pixel. The layout of each patch is arranged to be 15 pointings in a slightly overlapping grid of 3×5 pointings, giving a patch size of 2.1×2.3 deg^2. The seeing on average is $\sim 0.62''$ and $\sim 0.70''$ for the data observed in the z' and R_c passband, respectively. The observations of the 12 Southern patches were performed using the CTIO MOSAICII camera on the 4m telescope. The camera has $8k \times 8k$ pixels in total made of eight $2k \times 4k$ CCDs, and gives a 36×36 arcmin^2 field of view with $0.267''$ per pixel. Each patch has a 3×4 MOSAICII pointings in size of 1.8×2.4 deg^2. The seeing is $\sim 0.90''$ and $\sim 1.02''$ in the z' and R_c data. The RCS survey has a depth reaching $M^*_{R_c} + 1.0$ at $z \sim 1.0$. The 5σ limiting magnitude for the point source is $z_{AB} = 23.9$ and $R_c = 24.8$ (Vega) using an aperture of diameter $2.7''$. We summarize the RCS observations in Table 5.1.

For the CFHT patches, follow-up observations were made in B and V filters using the same telescope (Hsieh et al. 2005). The follow-up observation covers 33.6 deg^2 in total with 108 pointings ($\sim 75\%$ of the original RCS-CFHT patches). The runs were from May 2001 to June 2002. The typical exposure time in B and V are 840s and 480s, respectively. The average seeing is $\sim 0.95''$ in B and $\sim 0.65''$ in V. The 5σ limiting

magnitudes are B=25.0 and V=24.5 with an aperture of diameter 2.7″ on average.

Different from the field follow-up observations of the CFHT, the follow-up observations for the CTIO patches were targeted at selected RCS clusters. The motivation of the CTIO follow-up observations is to provide multi-color imaging as support for the RCS multi-object spectroscopy program which aims at obtaining a large sample of galaxy spectra in clusters to study the evolution of cluster populations as a function of cluster properties such as richness and dynamical state. The data were taken during runs in March, April, and September 2005. The targets were chosen from the RCS cluster catalogs with clusters of $B_{gc,rs} \geq 400$ and $\sigma_{rs} \geq 3.3$ at $z = 0.3 \sim 0.9$. The $B_{gc,rs}$ is a cluster richness parameter defined by the amplitude of galaxy-cluster center correlation function (Yee & López-Cruz 1999) using the red-sequence galaxies within 0.5Mpc of the cluster center. The σ_{rs} is the significance of peaks found in the galaxy density maps from the different color slices in the RCS cluster finding algorithm (Gladders & Yee 2005). Twenty pointings were imaged, for a total of ~ 7 deg^2. Ten of them were observed in the BV passbands only, as the R and z' photometry were available from the original RCS catalogs. The other ten pointings were observed in $BVRI$ filters, because the targets were located near the edges of the original RCS patches or the original RCS z' photometry is not deep enough at high redshift for the scientific purpose. The typical exposure time under good seeing condition ($\leq 1''$) in $BVRI$ were [60,24,20,16], [60,36,24,24], and [60,60,48,24] minutes for clusters at $z = 0.3 - 0.5$, $z = 0.5 - 0.7$, and $z = 0.7 - 0.9$, respectively. For consistency with the other data in this thesis, we choose clusters at $0.20 \leq z < 0.60$ from this data set. The RCS follow-up observations are summarized in Table 5.2.

5.2.1 Photometry Measurement

The z' and R_c data in the original RCS observation have been reduced as part of the RCS project (see Gladders & Yee 2005). The CFHT follow-up B and V catalogs together with z' and R_c photometry have been generated by Hsieh et al. (2005). This subsection focuses on the CTIO follow-up subset. The data were reduced using standard IRAF tasks for multi-extension FITs images, including bias subtraction and sky flatfielding. The object finding and photometry measures were executed using an algorithm in the *Picture Processing Package* (PPP; Yee 1991; Yee et al. 1996). A brief review of the algorithms has been presented in 4.2.2 in Chapter 4.

Table 5.1: Summary of The RCS Observations

Patches	CHFT	CTIO
Telescope diameter	3.6m	4m
CCD	12K	MOSAIC II
Pixel scale	$0.206''$	$0.267''$
CCD Field of view	$42' \times 28'$	$36' \times 36'$
Patch layout	3×5 pointings	3×4 pointings
Patch size	2.1×2.3 deg^2	1.8×2.4 deg^2
Filter	z' R_c	z' R_c
Exposure time	z': 1200s	z': 1500s
	R_c : 900s	R_c : 1200s
typical seeing	z': $0.65''$	z': $0.90''$
	R_c: $0.70''$	R_c: $1.05''$
5σ point-source limiting magnitude	$z_{AB} = 23.9$	
	$R_c(Vega) = 24.8$	

5.2.2 photometric calibration

For the CTIO subset, the photometry is calibrated using Landolt standard star fields (Landolt 1992), which were taken each night. Each Landolt field was observed more than once during the run. Assuming typical airmass term constants of [-0.15,-0.12,-0.09,-0.04] for BVR_cI at Cerro Tololo, we derive the zero points and color terms using the following equation:

$$m_{cal} = m_{computed} + Z + k * airmass + c * (m' - m_{computed}). \quad (5.1)$$

In the above equation, m_{cal} is the standard magnitude, $m_{computed}$ is the computed instrumental magnitude assuming a pseudo zero-point of 25 magnitude (hence the true zero-point is $25+Z$), k and c are the constants for the airmass and color term, and m' denotes the magnitude of the same object in the other filter. We demonstrate an example of the fit in Fig. 5.1 using the B-band standards. The vertical axis in the top

Table 5.2: The RCS Follow-up Observational Data

Patches	Northern (CFHT)	Southern (CTIO)
Runs	May 2001 - June 2002	March, April, September 2005
Filter	BV	$BV(R_c z'/I_c)$
total area	33.6 deg^2	$\sim$ 7deg^2
exposure time	B: 840s	B: 3600s
	V: 480s	V: 1440s - 3600s
		R_c: 1200s - 2880s
		I_c: 960s - 1440s
typical seeing	B: 0.95″	B: 1.35″
	V: 0.65″	V: 1.15″
		R_c: 1.25″
		I_c: 1.00″
5σ point-source limiting magnitude	B: 25.0	B: 24.64
	V: 24.5	V: 24.84
		R_c: 24.78
		I_c: 23.48

panel of Fig. 5.1 shows the difference between $m_{computed}$ and m_{cal} with airmass term applied versus the $V - B$ color from the Stetson's extension of the Landolt catalog (http://cadcwww.dao.nrc.ca/standards/). After applying a linear fit on $m' - m_{computed}$, the slope of the fit result is the color term and the true zero-point can be obtained by applying the offset to the pseudo zero-point. After applying the proper color term and zero-point, the calibrated magnitudes compared to the standard magnitudes are shown in the bottom panel of Fig. 5.1.

To ensure the internal agreement of our photometric calibration, the computed R_c photometry is cross-checked with the original RCS R_c using objects overlapping with the RCS patches. The BVI photometry is then adjusted using star color distributions in the RCS CFHT patches from Hsieh et al. (2005) with R_c photometry as the reference. The 5σ point-source limiting magnitudes are about [24.64, 24.84, 24.78, 23.48] for [20, 18, 10,

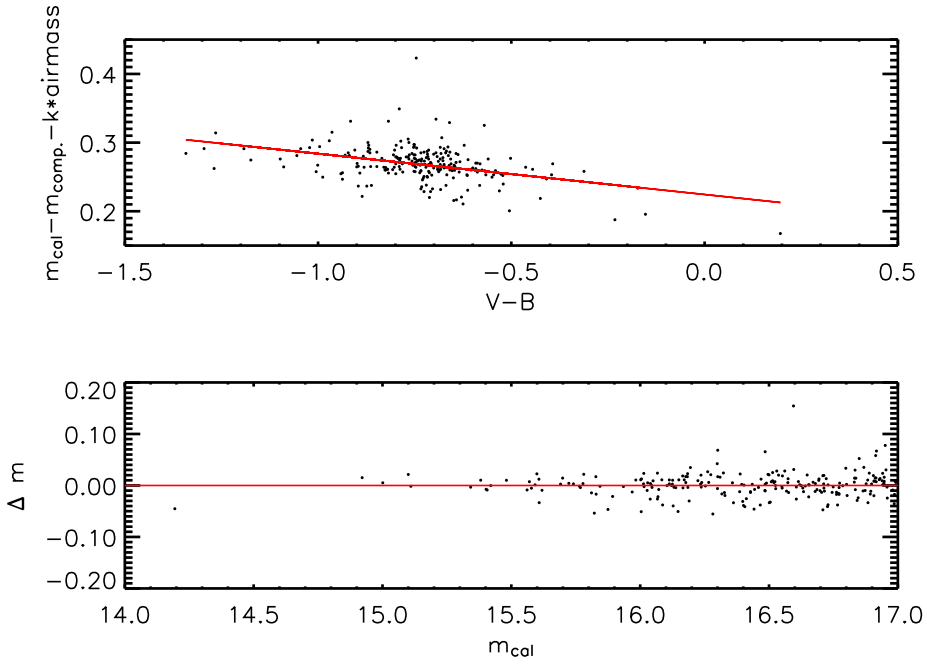

Figure 5.1: Derivations of the color term and zero point for B using 234 stars from the Stetson's extension of the Landolt standards. *Top:* Based on equation 5.1 with a constant airmass term, the y-axis is considered as a linear function of the observed color. Therefore, the slope (-0.0594) and offset (0.2244) of the linear fitting line are the color coefficient and the offset between the true and pseudo zero point. *Bottom:* The y-axis is the differences between the standard magnitudes and the calibrated ones after applying proper color correction and zero point. The r.m.s dispersion in Δm is ~ 0.020.

8] minutes total exposure time in BVR_cI, respectively.

5.3 Photometric Redshift Sample

5.3.1 Revised Photometric Redshift

The photometric redshift technique offers an easy and quick way to estimate numerous galaxy redshifts. Although the photometric redshift accuracy is not as precise as that of spectroscopic redshifts, it still provides reliable redshift information statistically speaking, and helps eliminate most background and foreground galaxies. We have presented the empirical photometric redshift technique in Chapter 2. The main concept of this photometric redshift technique is to assume that galaxy redshift can be expressed as a polynomial function of galaxy magnitudes and colors, with the coefficients derived from

a training set, a catalog containing spectroscopic galaxy redshifts and multi-passband photometry. The training set constructed from the Hubble Deep Field (HDF) and Canadian Network for Observational Cosmology Survey (CNOC2) observations contains 3,988 galaxies. Thanks to the overlaps between DEEP2 and RCS *0223* patch, we add the 1,312 galaxies with DEEP2 spectroscopic redshift and RCS photometry into the HDF+CNOC2 training set. These 5,300 training set galaxies are then divided into eleven bins based on their positions on the observed $(B - R_c)$ and R_c diagram. Each color-magnitude cell contains $\sim$ 500 galaxies on average. We then carry out the fitting procedure in each color-magnitude cell, and apply the solutions to galaxies in input catalogs with only photometry information. However, we find that the estimated photometric redshifts for faint training set galaxies ($\sim 22 \leq R_c < 24$) within an individual color-magnitude cell do not follow a correlation with spectroscopic redshift with a unity slope. We therefore apply a transformation to improve the poor photometric estimation. For galaxies in the input catalogs without spectroscopic redshift information, the transformation solution is assigned based on that of the training set which has the most similar color and magnitude as the input galaxy. The r.m.s. dispersions between estimated photometric and spectroscopic redshift for these faint magnitudes before and after applying the transformation are $\sim$0.122 and $\sim$0.085, respectively.

5.3.2 The Sample

Sample Selection

We select our sample as galaxies having photometric redshift between 0.02 and 1.4. Galaxies with large photometric redshift uncertainties are rejected from the sample. The selection criterion for photometric redshift error is:

$$P(z) = \int_{z_i - 3\sigma_{zcut}}^{z_i + 3\sigma_{zcut}} P_i(z')dz' > 0.997 :$$

the total probability for a galaxy within the $3\sigma_{z_{cut}}$ redshift range should be 0.997 at least. This $\sigma_{z_{cut}}$ is set as $\sigma_{z_{cut}} = 0.2(1 + z)$, equivalent to not including galaxies whose photometric redshift uncertainty is larger than 0.2(1+z). Owing to the removal of galaxies with large photometric redshift uncertainties, we compute a completeness weight w_i for each galaxy in the sample. This completeness is calculated based on the ratio of total galaxy number to that in the sample in each $\Delta m_{R_c} = 0.1$ magnitude bin. We use all galaxies in the calculation instead of separating them into blue and red galaxies, because we find that the completeness weights are similar for blue and red galaxies. In general,

the completeness weights increase toward faint magnitude. Therefore, a cutoff in R_c magnitude is set based on $w_i = 2$. The mean and median completeness weights in our sample are $w_i \sim 1.20$ and 1.09.

Galaxies in our sample are also selected as brighter than $M^*_{R_c} + 1.5$ with proper k- and e-corrections applied. We adopt $M^*_{R_c} = -21.41$ from Kodama & Arimoto (1997). The k-correction for each galaxy in our sample is estimated based on its position on the the galaxy color-redshift diagram using the tabular values in Poggianti (1997). The R_c luminosity evolution is approximated as $M(z) = M(0) - zQ$ where Q=1.24 for red galaxies and Q=0.11 for blue galaxies based on luminosity functions from the CNOC2 survey. (Lin et al. 1999).

The Clusters

For the purpose of studying global cluster environmental influence on galaxy properties, we select the cluster sample from the RCS cluster catalogs. The clusters are chosen as $B_{gc,rs} \geq 600$, $\Delta B_{gc,rs}/B_{gc,rs} < 1$, $\sigma_{rs} \geq 3.3$, and $z_{CL} < z_{cut}$. The z_{cut} is the redshift where the galaxy sample becomes incomplete at $M^*_{R_c} + 1.5$ in each patch, owing to the m_{R_c} cutoff based on $w_i = 2$. We have 60 clusters in total satisfying our selection criteria. The redshift distribution of these 60 clusters is presented in Fig. 5.2. We have 20, 25, and 15 clusters in $0.20 \leq z < 0.35$, $0.35 \leq z < 0.45$, and $0.45 \leq z < 0.60$, respectively. Galaxies in the sample are then classified as 'cluster galaxies' if the probability density distributions of their redshifts satisfy the criteria with respect to the redshift space of the clusters (see § 4.5.2 in Chapter 4).

Owing to the use of photometric redshifts, a galaxy may belong to multiple clusters. Because the gravitational potential of a galaxy cluster drops quickly as the cluster-centric radius increases, a galaxy within a few virial radii of a cluster is more likely to be affected by this cluster environment rather than by other clusters. Therefore we re-assign membership of cluster galaxies belonging to multiple clusters to a specific cluster if they are located within $2R_{200}$ of the cluster.

Limiting cluster galaxies to projected distances up to 10 virial radii and applying the galaxy selection criteria above, we have 49373, 101775, and 109454 cluster galaxies in each redshift bin.

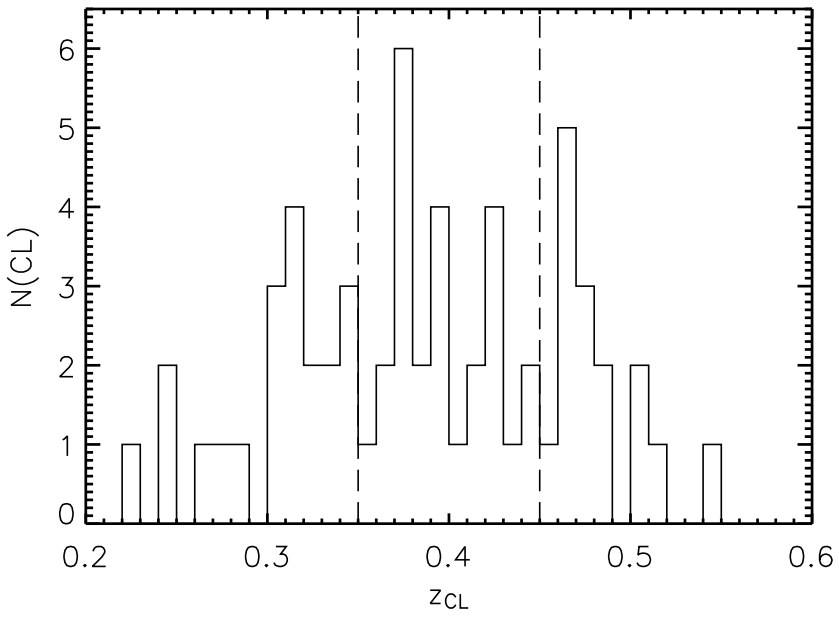

Figure 5.2: The redshift distribution of our cluster sample, 60 in total. The vertical dashed lines divide the clusters into three redshift bins as $0.20 \leq z_{CL} < 0.35$, $0.35 \leq z_{CL} < 0.45$, and $0.45 \leq z_{CL} < 0.60$. Note the the number of clusters at $z > 0.50$ drops due to fewer pointings having sufficient depth to be complete at the $M^*_{R_c} + 1.5$ limit.

5.4 Environmental Parameters and Population Fractions

The aim of this thesis is to probe galaxy photometric properties in different environments. These environments can be classified into *local* and *global* regimes. The local regimes can be further distinguished into *local projected galaxy densities* of individual galaxies, or galaxies within *galaxy groups*, while the *global* one focuses on the large-scale cluster environment. Generally speaking, old, passively evolving galaxies are red in color. Therefore a population fraction in a certain environment can indicate the evolutionary stage of the galaxies therein. We have defined these environmental parameters and the computed population fraction in Chapter 3. Here we present a brief review of them.

5.4.1 Local Projected Galaxy Density, Σ_5

The local projected galaxy density Σ_5 is calculated based on the nearest-neighbor method. First, all galaxies with their photometric redshift uncertainties in the same redshift space

as the seed galaxy are projected to the same redshift as the seed galaxy. A circular aperture centered at the seed galaxy then has its radius increased until the total completeness weight $\sum w_i$ reaches 5. This radius is taken as r_5, and Σ_5 is accordingly computed as

$$\Sigma_5 = \frac{\sum w_i}{\pi r_5^2} - \Sigma_{bg}(z_{seed}),$$

where $\Sigma_{bg}(z_{seed})$ is the estimated background galaxy surface density per Mpc^2 at the seed galaxy's redshift.

5.4.2 Cluster-Centric Radius, r_{CL}

To investigate galaxy properties as a function of cluster-centric radius, a fair comparison is to use scaled radii based on a dynamical radius of the cluster so that we can investigate dynamically similar parts of the clusters and are not limited only either to the core of rich clusters or outskirts of poor ones. We scale the projected distance to the centers by the virial radius R_{200} (the radius within which the density is 200 times the critical density). The R_{200} is estimated from the correlation with cluster richness B_{gc} (Yee & Ellingson 2003), because it is observationally expensive to measure. The typical value for R_{200} is ~ 1.45Mpc.

5.4.3 Population Fraction, f_{red}

The population fraction is indicated by the f_{red} parameter: the fraction of red galaxies after the background contamination correction. The f_{red} is computed using the observed color-magnitude diagram, where the boundary to define red and blue populations depends on redshift. We use observed $B-R_c$ color for $z < 0.5$ and $V-I_c$ color for $z \geq 0.5$ so that the chosen filters better straddle the 4000 Å break. We estimate f_{red} using a statistical inference, considering the small number of galaxies in a given environment for most situations. The detailed description of the computation is presented in §3.3 in Chapter 3.

5.5 Results

We follow a similar structure as §4.7.2 in Chapter 4 in exploring the proprieties of cluster galaxies in different local and global environments. We classify the RCS cluster galaxies into the same luminosity subclasses: *bright:* $M_{R_c}^{k,e} < M_{R_c}^* + 0.7$ and *faint:* $M_{R_c}^* + 0.7 \leq$

$M^{k,e}_{R_c} < M^*_{R_c} + 1.5$. The redshift of the RCS cluster galaxies are separated into three redshift bins: $0.20 \leq z < 0.35$ ($z \sim 0.30$), $0.35 \leq z < 0.45$ ($z \sim 0.40$), and $0.45 \leq z < 0.60$ ($z \sim 0.50$). The local projected galaxy density Σ_5 are binned into three divisions as *high*, *intermediate*, and *low* based on equal galaxy number at a fixed redshift. The global cluster environmental parameter, r_{CL}, is classified into six regions as 0-1, 1-2, 2-3, 3-4, 4-5, and 5-6 R_{200}. In the discussion we demarcate r_{CL} into three regimes: *virial*: within $1R_{200}$, *infall*: between $1 - 3R_{200}$, and *outskirts*: beyond $3R_{200}$. In this chapter we explore the dependence of f_{red} for individual cluster galaxies on four parameters: luminosity, redshift, Σ_5, and r_{CL}.

Fig. 5.3 plots the f_{red}-z trends for the cluster galaxies in two luminosity subsamples but reside in different r_{CL} and Σ_5 environments. Each environment is labelled in each panel, with r_{CL} increasing toward the right-hand columns and Σ_5 increasing toward the top rows. The solid and dotted curves in each panel represent the *bright* and *faint* subsamples, respectively. All the f_{red}-z trends in a fixed environment are declining with increasing redshift in Fig. 5.3. In other words, the Butcher-Oemler effect is observed in all environments. Meanwhile, for a fixed environment the bright subsample ($M^{k,e}_{R_c} < M^*_{R_c} + 0.7$) exhibits a larger f_{red} compared with the faint subclass for all cases. The differences in f_{red} among galaxies of different luminosities but located in the same environment and redshift indicate that galaxy properties depend strongly on their luminosities.

For the purpose of studying the effects of various environments, we focus on how f_{red} changes as a function of redshift or an environmental parameter for the bright and faint subsamples. We use x to denote any one of the three parameters: redshift, Σ_5, or r_{CL}. Fig. 5.3 is re-plotted in Fig. 5.4 to Fig. 5.8 as a function of x or in different axes to address the role of a specific parameter. We discuss the f_{red}-x trends for the luminosity subsamples with the other two parameters held constant.

5.5.1 Global Environmental Influence

To probe the cluster environmental influence on galaxies of different luminosities, we re-plot Fig. 5.3 by controlling both Σ_5 and redshift, and present it in Fig. 5.4. Each row is for a fixed redshift bin, and Σ_5 increases from the left to the right-hand column. The solid and dotted lines represent the bright and faint luminosity subsamples. Generally speaking, all the f_{red}-r_{CL} trends show a decline with increasing r_{CL}, but become basically flat in the *outskirts* regions, indicating that the cluster environmental influence is most significant within the cluster *virial* region. However, such a cluster environmental impact

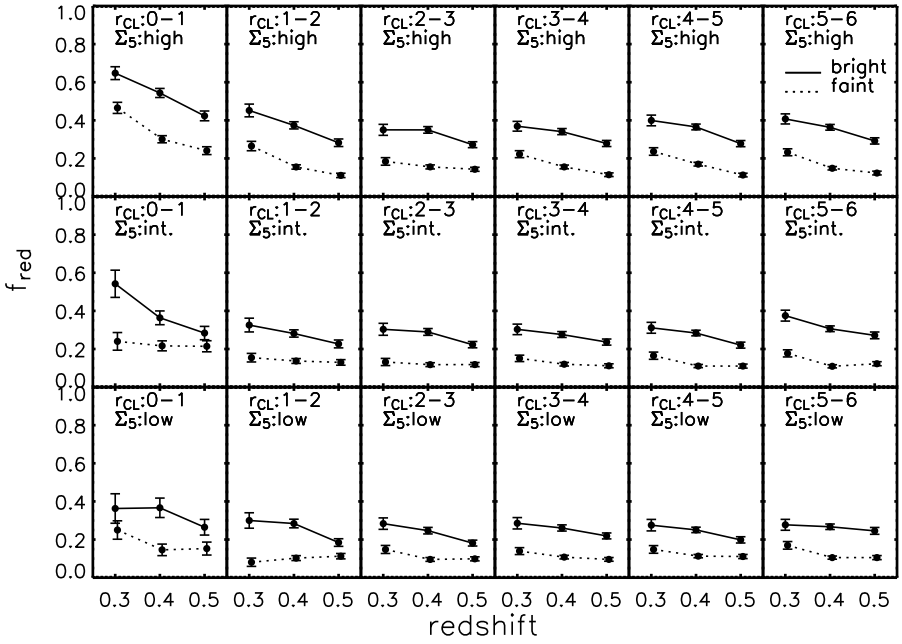

Figure 5.3: f_{red} as a function of redshift in a fixed environment as notated in each panel. The solid and dotted curves represent the bright ($M^{k,e}_{R_c} < M^*_{R_c} + 0.7$) and faint ($M^*_{R_c} + 0.7 \leq M^{k,e}_{R_c} < M^*_{R_c} + 1.5$) subsamples, respectively. Both the bright and faint subsamples exhibit decreasing f_{red} toward high redshift in a fixed environment.

depends on both redshift and local projected galaxy density. For a fixed Σ_5 bin, the increasing f_{red} toward the cluster *virial* region is more apparent at low redshift compared with high redshift. This redshift dependence is more significant in regions of high Σ_5, where f_{red} begins differing from the mean at $\sim 2-3R_{200}$ at $z \sim 0.30$, but only at $\sim 1R_{200}$ at $z \sim 0.50$.

We investigate more quantitatively the f_{red}-z trends as a function of cluster-centric radius in a fixed local galaxy density bin. To do this, we perform a linear three-point fit to each f_{red}-z trend in Fig. 5.3, and plot the slope (i.e., $\Delta f_{red}/\Delta z$) as a function of r_{CL} in different Σ_5 bins in Fig. 5.5. We omit the *intermediate* Σ_5 bin, because this *intermediate* Σ_5 bin may contain large mixing of galaxies from the other two Σ_5 bins due to fuzzy Σ_5 measurements.

In Fig. 5.5 we observe that the slopes of the f_{red}-z trends in a fixed Σ_5 bin become gentler as r_{CL} increases from the cluster *virial* region to the *outskirts*, implying that the Butcher-Oemler effect becomes weaker further out from the cluster center. In other words, the rate that galaxies truncate their star formation is faster within cluster *virial*

region. In high Σ_5 region, the rate in the cluster *virial* region is about twice as faster as that in the *outskirts* , but the rate are similar for the bright and faint subsamples. In *low* Σ_5 location, the bright subsample exhibits larger changes in red galaxies fractions with redshift than the faint subclass. Moreover, the changes in the f_{red}-z slopes is less apparent from the cluster *virial* region to the *outskirts* . That is, the cluster environmental influence in low Σ_5 regions is less effective in truncating star formation in infalling galaxies.

To examine more quantitatively the cluster environmental influence on galaxies in various local galaxy density regions and at different redshift intervals, we compute the 'excess' of f_{red} as the *difference* between the f_{red} at $r_{CL} < 1$ and the mean value at the *outskirts*($r_{CL} \geq 3$). We do not take the *ratio* of the f_{red} at $r_{CL} < 1$ to the mean f_{red} at the *outskirts* regions, because the differences in f_{red} directly correlate with changes in red galaxy numbers. The higher the number of galaxies which experience color transition, the stronger the cluster environmental influence. For two sets of galaxies, if the number of affected galaxies in these two sets is same, then the set with the smaller total galaxy counts will exhibit a larger fractional change in its f_{red}. On the other hand, their f_{red} may change by the same factor, but the actual numbers of galaxies undergoing the changes are different. We plot the excesses as a function of redshift in the *high* and *low* Σ_5 bins in Fig. 5.6 for both the bright and faint subsamples. In general the high Σ_5 regions have a higher excess in f_{red} in the *virial* region compared with the *outskirts* than the low Σ_5 locations. Interestingly, in the *high* Σ_5 bin, the 'excess' of f_{red} increases from $z \sim 0.50$ to $z \sim 0.30$ by a factor of ~ 1.8. In the *low* Σ_5 division, however, the 'excess' in f_{red} are small and comparable among different redshift intervals. The results, once again, show that the cluster environment, primarily in the *virial* region, has a relatively larger influence in regions of high local galaxy density and at lower redshift. Hence, the global cluster environment may accelerate the influence of local galaxy density on galaxy population.

5.5.2 Local Environmental Effect

To probe the effect due to different Σ_5, we re-plot Fig. 5.3 by plotting f_{red}-Σ_5 trends at each fixed r_{CL} and redshift. The results are presented in Fig. 5.7, where each row is for a fixed redshift and r_{CL} increases from the left-hand column of the panels to the right-hand one. The solid and dotted curves represent bright and faint luminosity subsamples, respectively. In general, both bright and faint luminosity subsamples exhibit increasing f_{red}-Σ_5 trends, indicating the impact of galaxy local environment parameterized by Σ_5.

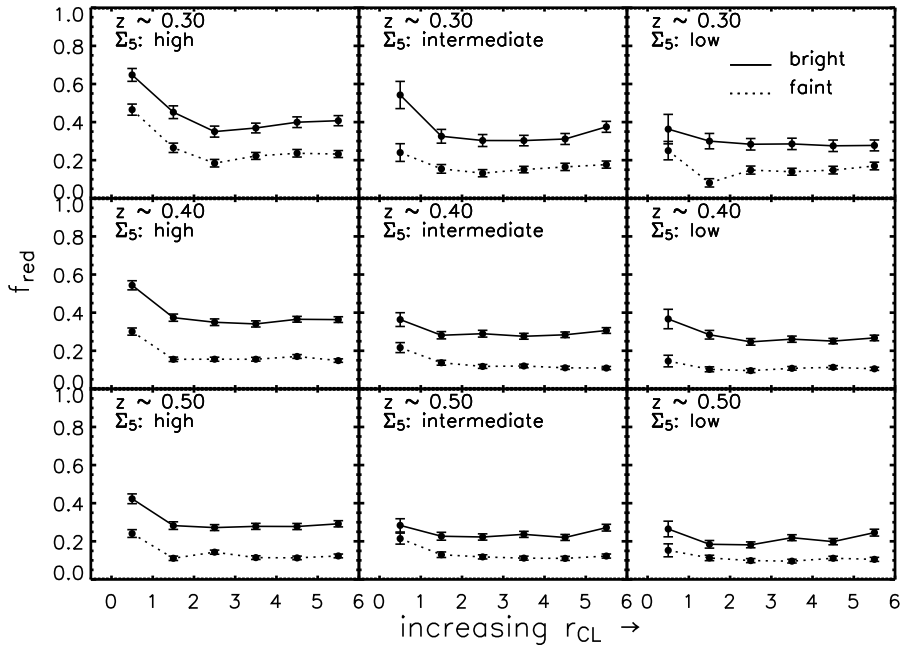

Figure 5.4: f_{red} as function of r_{CL} for bright (solid) and faint (dotted) subsamples with Σ_5 and redshift controlled. The apparent changes in f_{red} are primarily observed at the cluster *virial* region.

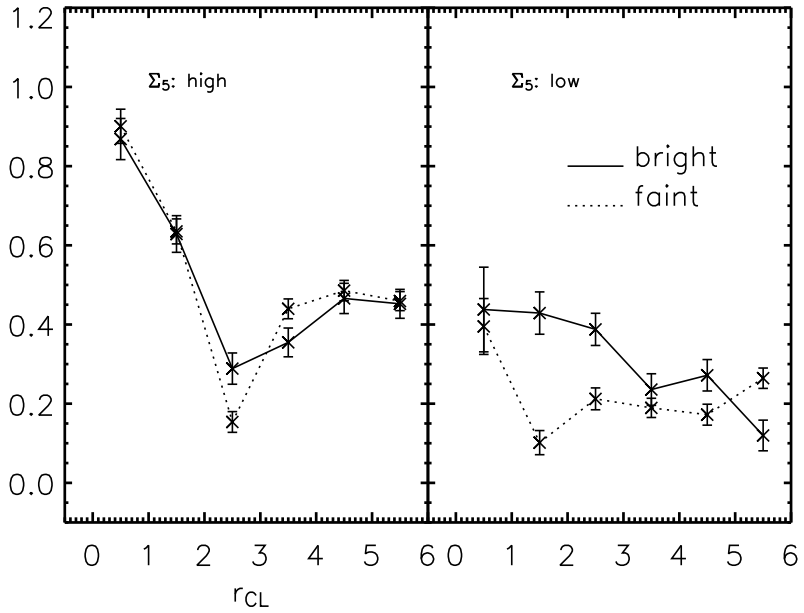

Figure 5.5: The slopes of the f_{red}-z trends in Fig. 5.3 as a function of r_{CL} in a fixed Σ_5 bin. The slopes increase significantly toward the cluster *virial* region.

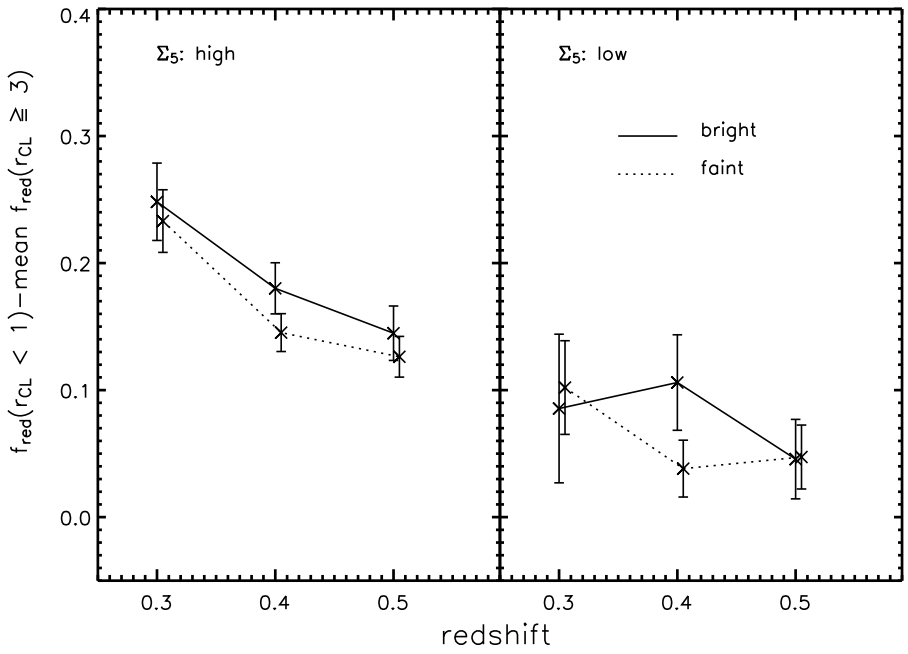

Figure 5.6: The 'excess' in f_{red} as a function of redshift in a fixed Σ_5 bin. The y-axis is the difference between the f_{red} within $1R_{200}$ (the *virial* region) and the mean value at larger r_{CL} (*outskirts*) based on Fig. 5.4. The solid and dotted curves represent bright and faint subsamples, respectively. The excess in f_{red} is larger in the high Σ_5 region than low Σ_5 location.

We note that the trends are all relatively weak except at the cluster *virial* region. To investigate more quantitatively the effect of Σ_5 on these two luminosity subsamples at different r_{CL}, we carry out a simple three-point linear fit to each f_{red}-Σ_5 trend in each panel in Fig. 5.7, and then plot the slopes as a function of r_{CL} at each redshift bin in Fig. 5.8. The larger value on the Y-axis in Fig. 5.8 means a steeper f_{red}-Σ_5 trend and more significant local environmental impact.

Viewing Fig. 5.8 as a whole, the f_{red}-Σ_5 slopes for both the bright and faint subsamples become relatively shallower (i.e., weak dependence of f_{red} on local galaxy density) at $r_{CL} \geq 2$ for all redshift bins. This result, again, indicates the cluster environment accelerates galaxy evolution in the *virial* regions. At $z \sim 0.40$ and $z \sim 0.50$, the bright galaxies exhibit steeper f_{red}-Σ_5 trends compared with the faint subsample at the cluster *outskirts*, implying a stronger dependence in the f_{red} on Σ_5 for the bright subclass. In tandem with the fact that bright galaxies possess larger f_{red}, the differences in the f_{red}-Σ_5 slopes between the bright and faint subsamples suggest that evolution starts in bright galaxies in high Σ_5 regions, and the cluster environment enhances such local environmen-

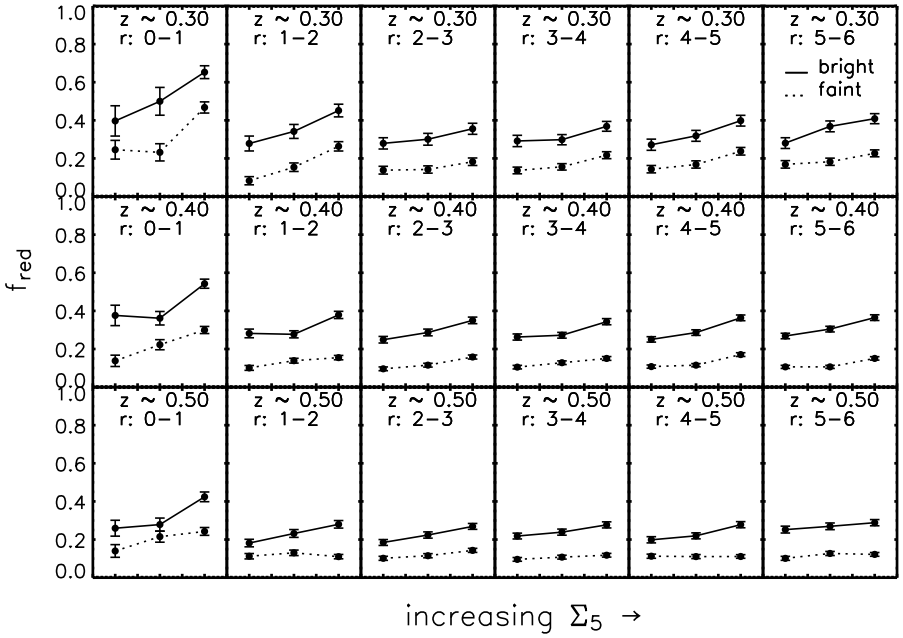

Figure 5.7: The f_{red} as a function of Σ_5 for bright (solid) and faint (dotted) subsamples with r_{CL} and redshift controlled. The f_{red} is larger when Σ_5 increases.

tal impact. However, at $z \sim 0.30$, the bright and faint subsamples exhibit similar slopes in the f_{red}-Σ_5 trends, implying the similar impact caused by the local environment.

In summary, galaxy evolution starts from bright galaxies at high redshift in larger galaxy density regions, then the evolution shifts to galaxies in the low galaxy density regions and of the fainter luminosity. At high redshift it is the bright galaxies that experience stronger local environmental impact, but the local environmental impact is similar on both the bright and faint galaxies at low redshift. The local environmental effect, however, has a dependence on cluster-centric radius. The effect is stronger at the cluster *virial* region, especially at low redshift, a reflection of the quickened galaxy evolution driven by the cluster environment.

5.6 Discussion

Galaxy properties are believed to be affected by their environment. With an aim to investigate environmental dependence of galaxy properties, we focus on the environmental influence on galaxies of different luminosities. Our results show that galaxies of similar luminosity possess larger f_{red} when they are located in high Σ_5 or cluster *virial* regions

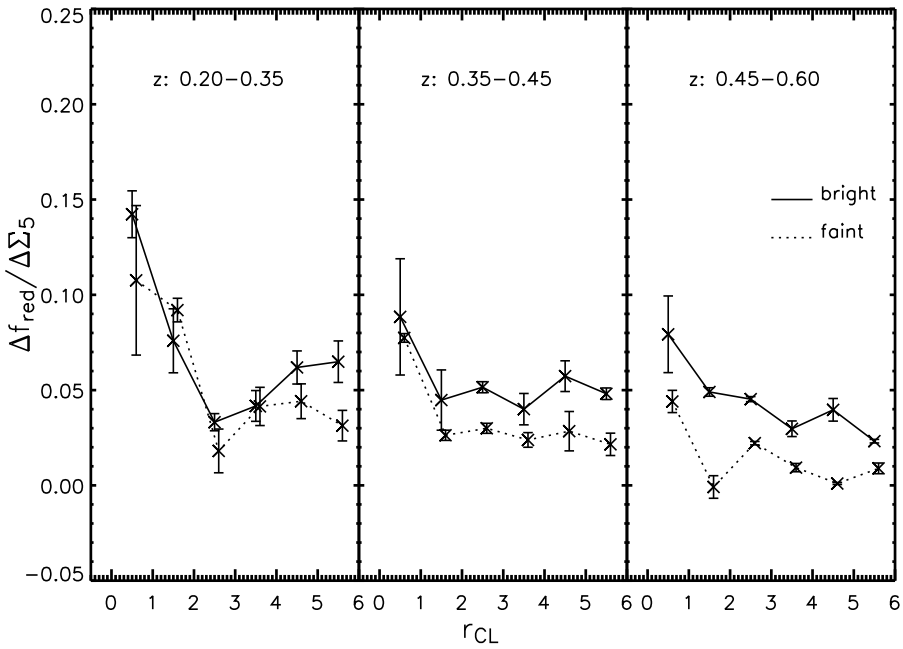

Figure 5.8: The slopes of the f_{red}-Σ_5 trends as a function of r_{CL} using a simple three-point linear fit based on Fig. 5.7. The solid and dotted curves represent the bright and faint luminosity subsamples. The slopes become gentler from the cluster *virial* region to the *outskirts*. The differences in the slopes between the bright and faint galaxies depend on redshift.

compared to those sited in low Σ_5 or cluster *outskirts* locations. The differences in f_{red} for galaxies of similar luminosities but in different environments are the consequences nurtured by the environment.

5.6.1 Dependence of f_{red} on Galaxy Luminosity

The result of Fig. 5.3 shows that bright galaxies have larger f_{red} than faint galaxies in all environments and at all redshift intervals. This strong dependence of f_{red} on galaxy luminosity has been known in the literature (e.g., Balogh et al. 2004; Kodama et al. 2004; De Lucia et al. 2006; Cucciati et al. 2006).

Because bright galaxies are more massive than faint ones in general, the larger f_{red} possessed by bright galaxies implies that star formation within bright galaxies has stopped at an earlier time than that in the faint ones. This is evidence for galaxy 'down-sizing' evolution in star formation (Cowie et al. 1996), as studies of cosmic star formation have suggested that the global star formation rate declines rapidly since $z \sim 2$ and the sites

of star formation shift to galaxies of smaller mass at lower redshift (Madau et al. 1996; Hopkins 2004; Borch et al. 2006; Bell et al. 2007; Bundy et al. 2006). We find that this down-sizing effect is observed in all environments, within cluster virialized region and in low projected galaxy density regions. However, the down-sizing effect, in terms of the differences in f_{red} between the bright and faint subsamples, are affected by environment. Fig. 5.5 shows that the bright and faint galaxies in high Σ_5 regions have similar slopes in the $f_{red} - z$ trends at all r_{CL}. In regions of low Σ_5, however, the bright galaxies exhibit steeper slopes in the $f_{red} - z$ trends than the faint subsample.

5.6.2 Global Cluster Environmental Influence

Galaxy clusters are observed to host more blue members at higher redshift, which is known as the Butcher-Oemler effect (Butcher & Oemler 1984). It has been suggested that the Butcher-Oemler effect is caused by cluster environment (e.g., Metevier et al. 2000). As galaxies evolve with time, the changes of population fractions in clusters at different redshifts should be compared with the field at the same epoch in order to investigate whether the Butcher-Oemler effect is driven by cluster environment. Using a sample of 65624 galaxies over 1×1 deg^2 area in the CFHT Legacy Survey Deep Fields, Nuijten et al. (2005) find that the fraction of red galaxies derived from galaxy color bimodality in the 'cluster-like' environment (regions of high overdensity in their work) changes 60% faster with redshift compared with the value in the field.

Our sample contains 60 optically selected clusters at $0.20 \leq z < 0.60$. Fig. 5.3 shows that the f_{red} increases with decreasing redshift (i.e., the Butcher-Oemler effect) for all environments, including regions of low galaxy density and at large cluster-centric radii. The effect of the cluster environmental influence, measured by the excess in f_{red} between the virialized region and the outskirts, is stronger in regions of high galaxy density, and also stronger at low redshift. If we consider the Butcher-Oemler effect as the additional evolution in clusters compared with the field, Fig. 5.6 shows that a strong Butcher-Oemler effect is observed within the cluster virialized region, where $\Delta f_{red}/\Delta z$ is about a factor of 2 larger than the outskirts. We note that the cluster environmental influence is primarily observed at $r_{CL} < 1.5$ (Fig. 5.4); there is no dependence in f_{red} on r_{CL} beyond $r_{CL} \sim 2$. The fact that cluster environmental influence is more apparent in high density regions indicates different mechanisms being active in clusters in driving galaxy evolution. In regions of high galaxy density, mechanisms such as galaxy harassment and tidal interactions are perhaps more effective, while ram-pressure is likely to be the

predominant mechanism in low galaxy density regions.

5.6.3 Effect of Local Galaxy Density

With the RCS sample, we are able to investigate the local environmental effect as a function of cluster-centric radii at a fixed redshift interval. From Fig. 5.7, the f_{red} is larger with larger Σ_5 at a fixed r_{CL}, as an illustration of the local environmental effect. This local environmental effect has been know for decades (e.g., Dressler 1980; Goto et al. 2003; Mateus et al. 2007; Cooper et al. 2007). The studies using SDSS data have also revealed the dependence of galaxy population fractions at $z \sim 0.05$ on their local galaxy environment for galaxies of fixed luminosity (e.g., Balogh et al. 2004; Baldry et al. 2006; Ball et al. 2006; Park et al. 2007). Our work, over the redshift range between 0.20 and 0.60, further reveals that this dependence of galaxy population fractions in local environment are observed at higher redshift. However, Fig. 5.8 reveals a relatively weak dependence of f_{red} on Σ_5. The strong dependence of f_{red} on Σ_5 is observed within the cluster virial radius. This result implies that the cluster environment accelerates galaxy evolution.

5.6.4 Dependence of Local Density Effect On Galaxy Luminosity

Fig. 5.8 shows that the local density effect on galaxies of different luminosities depends on redshift. At $z \sim 0.40$ and $z \sim 0.50$, the bright galaxies have a stronger dependence in f_{red} on Σ_5 than the faint subsample. At $z \sim 0.30$, such dependence are similar between the bright and faint galaxies.

We note that the studies done by Balogh et al. (2004) and Baldry et al. (2006) using the SDSS data at $z \sim 0.05$ show stronger local galaxy density impact on faint galaxies or galaxies of smaller stellar mass. This is an interesting comparison. The results indicate that the local environmental effect depends on galaxy mass (the down-sizing scenario). In other words, there is an interplay between local environmental effect and the down-sizing scenario.

Within regions of similar galaxy densities, the massive galaxies have more active star formation which started earlier than that in the less massive galaxies (galaxy down-sizing), and are expected to have their star formation completed first. Elbaz et al. (2007) find a reversal in star formation-density relation from that at lower redshift, showing

that star formation rates within individual galaxies *increase* with galaxy density and their stellar mass at $z \sim 1.0$. In other words, at $z \sim 1.0$ galaxies in high density sites form stars actively compared to those in low Σ_5 regions, and hence these galaxies are expected to complete their star formation and become red first. At $z \sim 0.50$ massive bright galaxies in denser sites may already have had their star formation quenched, while those in less dense locations are still undergoing active star formation. In contrast, the less massive faint galaxies are still forming stars and have not completed their evolution in all density regions. At $z \sim 0.05$, the massive bright galaxies in low Σ_5 regions also completed their star formation, and consequently possess large f_{red} and exhibit no dependence on Σ_5. However, Σ_5 starts to have an effect on the less massive faint galaxies; those in high Σ_5 regions stop forming stars and become red, while those in low density locations are still forming stars, and therefore they exhibit a strong dependence in their f_{red} on Σ_5. In other words, if regions of high Σ_5 host mechanisms of quenching star formation, this effect impacts on massive bright galaxies first then on less massive faint ones. The combination of the literature and our work reveals an interplay of intrinsic down-sizing effect and extrinsic local galaxy environmental effect operating on galaxy evolution simultaneously.

5.6.5 Scenario of Galaxy Evolution

Summing up all the results of Fig. 5.3 to Fig. 5.8, a simple scenario of galaxy evolution can be pictured as the follows. At high redshift, bright galaxies start to evolve within high galaxy density regions. These high galaxy density regions may be small or proto-clusters which eventually grow into larger ones at low redshift by either merging with each other or accreting galaxies from the field. Since these bright galaxies have started their evolution at high redshift, they may have consumed their gas and completed their star formation during the growth of the clusters. In contrast, faint galaxies start their evolution at later time and still form stars. As the faint galaxies are accreted into clusters, their star formation is truncated and this is reflected in their colors. The different starting times of star formation activity in bright and faint galaxies result in not only the down-sizing evolution but also different dependences in their red population fraction on distances from cluster centers.

5.7 Conclusions

We have classified our cluster galaxies into bright and faint luminosity subsamples, and discussed the dependence of their red galaxy fractions (f_{red}) on different environmental parameters. We observe that both galaxy down-sizing evolution (star formation stops earlier in bright galaxies than faint systems) and the Butcher-Oemler effect (smaller f_{red} at higher redshift) in all environments. The differences in f_{red} possessed by galaxies of different luminosities but located in the same environment illustrate the galaxy down-sizing evolutionary scenario which is the outcome of natural evolution.

Both bright and faint galaxies have their f_{red} decreased toward higher redshift. This Butcher-Oemler effect becomes weaker from the virialized regions of clusters to the outskirts in a fixed galaxy density bin (Σ_5), and is also stronger toward regions of high galaxy density at a fixed cluster-centric radius (r_{CL}).

By exploring f_{red} as a function of r_{CL} with Σ_5 controlled, we have shown that cluster environmental influence is primarily effective within the virial radius. The cluster environment has stronger impact on galaxies located in high galaxy density regions, and is more effective at low redshift; this may be an indication of the mechanism(s) that are important in affecting evolution of cluster galaxies.

At a fixed r_{CL}, we have shown that f_{red} is larger in high Σ_5 regions for each luminosity subsample. This local environmental effect is apparent within cluster virial radius and becomes relatively weak at cluster outskirts. In summary, galaxy properties are determined by their intrinsic properties, and their environment has an additional effects in accelerating their evolution.

References

Baldry, I. K., Balogh, M. L., Bower, R. G., Glazebrook, K., Nichol, R. C., Bamford, S. P., & Budavari, T. 2006, MNRAS, 373, 469

Ball, N. M., Loveday, J., Brunner, R. J., Baldry, I. K., & Brinkmann, J. 2006, MNRAS, 373, 845

Balogh, M. L., Baldry, I. K., Nichol, R., Miller, C., Bower, R., & Glazebrook, K. 2004, ApJ, 615, L101

Bell, E. F., Zheng, X. Z., Papovich, C., Borch, A., Wolf, C., & Meisenheimer, K. 2007, ArXiv e-prints, 704

Borch, A., Meisenheimer, K., Bell, E. F., Rix, H.-W., Wolf, C., Dye, S., Kleinheinrich, M., Kovacs, Z., & Wisotzki, L. 2006, A&A, 453, 869

Butcher, H. & Oemler, Jr., A. 1984, ApJ, 285, 426

Cooper, M. C., et al. 2007, MNRAS, 224

Cowie, L. L., Songaila, A., Hu, E. M., & Cohen, J. G. 1996, AJ, 112, 839

Cucciati, O., et al. 2006, ArXiv Astrophysics e-prints

De Lucia, G., Springel, V., White, S. D. M., Croton, D., & Kauffmann, G. 2006, MNRAS, 366, 499

Dressler, A. 1980, ApJS, 42, 565

Elbaz, D., et al. 2007, ArXiv Astrophysics e-prints

Gladders, M. D. & Yee, H. K. C. 2005, ApJS, 157, 1

Goto, T., Yamauchi, C., Fujita, Y., Okamura, S., Sekiguchi, M., Smail, I., Bernardi, M., & Gomez, P. L. 2003, MNRAS, 346, 601

Hopkins, A. M. 2004, ApJ, 615, 209

Hsieh, B. C., Yee, H. K. C., Lin, H., & Gladders, M. D. 2005, ApJS, 158, 161

Kodama, T. & Arimoto, N. 1997, A&A, 320, 41

Kodama, T., et al. 2004, MNRAS, 350, 1005

Landolt, A. U. 1992, AJ, 104, 340

Lin, H., Yee, H. K. C., Carlberg, R. G., Morris, S. L., Sawicki, M., Patton, D. R., Wirth, G., & Shepherd, C. W. 1999, ApJ, 518, 533

Madau, P., Ferguson, H. C., Dickinson, M. E., Giavalisco, M., Steidel, C. C., & Fruchter, A. 1996, MNRAS, 283, 1388

Mateus, A., Sodré, L., Cid Fernandes, R., & Stasińska, G. 2007, MNRAS, 374, 1457

Metevier, A. J., Romer, A. K., & Ulmer, M. P. 2000, AJ, 119, 1090

Nuijten, M. J. H. M., Simard, L., Gwyn, S., & Röttgering, H. J. A. 2005, ApJ, 626, L77

Park, C., Choi, Y.-Y., Vogeley, M. S., Gott, J. R. I., & Blanton, M. R. 2007, ApJ, 658, 898

Poggianti, B. M. 1997, A&AS, 122, 399

Yee, H. K. C. 1991, PASP, 103, 396

Yee, H. K. C. & Ellingson, E. 2003, ApJ, 585, 215

Yee, H. K. C., Ellingson, E., & Carlberg, R. G. 1996, ApJS, 102, 269

Yee, H. K. C. & López-Cruz, O. 1999, AJ, 117, 1985

Chapter 6

Galaxy Groups in the RCS Sample

6.1 Introduction

We have presented in Chapter 5 that galaxy properties are determined by their intrinsic luminosity, and their evolution is influenced by their environment. In Chapter 5 we focused on the environmental influence related to local projected galaxy density and cluster-centric radii from the perspective of individual cluster galaxies. However, the majority of galaxies reside in small aggregations: galaxy groups. Galaxy groups, where galaxies are bound by their mutual gravity, can also provide essential environmental impact on their members. Limited by the small-size CNOC1 sample, Chapter 4 gives some preliminary results of group environmental influence. With $\sim$ 90 galaxy groups in the same redshift space as the clusters, we have observed in Chapter 4 that galaxies in groups are redder on average than those not associated with groups, and galaxies within galaxy groups may still maintain their own properties when the whole groups are positioned in the cluster environment. As the goal of this thesis is to investigate the dependence of galaxy properties on various environments, we concentrate on the role of galaxy groups in affecting galaxy properties using the RCS sample in this chapter. We have presented the RCS data set and the photometric redshift sample in §5.2 and §5.3. The structure of this chapter is as follows. In § 6.2 we provide a review of the algorithm developed to identify galaxy groups using a photometric redshift sample. Section 6.3 describes the measurement of group richness. In § 6.4 we define the distinction between galaxy clusters and galaxy groups. We present the general properties of galaxy groups in § 6.5, and the properties for the infalling groups in § 6.6. We discuss the results in § 6.7. Finally we summarize the results in § 6.8. We adopt a flat cosmology with $\Omega_m = 0.30$, $\Omega_\Lambda = 0.70$, and $H_0 = 70$ km/s/Mpc.

6.2 Identifying Galaxy Groups

We intend to study photometric properties of galaxy groups in the RCS sample (see §5.3 in Chapter 5) over a redshift range of $0.2 \leq z < 0.6$. With photometric redshift measurements, the identification of galaxy groups is achieved using the *'probability Friends-of-Friends' (pFOF)* algorithm (see Chapter 2). Here we present a brief review of the group finding algorithm.

The pFOF algorithm adopts the standard friends-of-friends linking idea in 2D space, but uses the normalized total probability density of the photometric redshift measurement in the radial direction to determine membership. Therefore, the criteria in the algorithm to form a galaxy group are determined by two parameters: $D0_{xy}$ and $P_{ratio,crit}$. $D0_{xy}$ is the 2D comoving linking length, and is scaled to correct for the completeness weight w_i and sparse galaxy density at high redshift in a flux limited sample. $P_{ratio,crit}$ is a normalized total redshift probability density for all galaxies to reside in the same photometric redshift space. For a galaxy to become a member of a galaxy group, it must have its P_{ratio} greater than the $P_{ratio,crit}$ criterion. As a result, the uncertainties of a group redshift measurement will improve when there are more and more galaxies joining into the group.

This pFOF algorithm has been tested using a simulated catalog based on the Virgo Consortium Millennium Simulations (Springel et al. 2005). Different linking criteria in both $D0_{xy}$ and $P_{ratio,crit}$, as well as various sample depths, have been adopted to investigate the group-finding performance. In general, the recovery rate of mock groups increases when larger $D0_{xy}$ is used with a fixed $P_{ratio,crit}$, but the fractions of false detected groups become larger. With a fixed $D0_{xy}$, the recovery rate is better when smaller $P_{ratio,crit}$ is used but the false detection rate increases as well. As the best compromise between recovery and false detection rates, we adopt $D0_{xy} = 0.25$Mpc and $P_{ratio,crit} = 0.37$ as the linking criteria, where the recovery rate is greater than 80% for mock groups of halo mass $\geq 1.2 \times 10^{13} M_{\odot}$, and the false detection rate is $\sim 10\%$ for pFOF groups of ~ 8 net members. We note that the recovery rate and false detection rate are estimated using a sample of $M^*_{R_c} + 2$ depth. For a flux-limited sample, the redshift at which the sample is complete decreases if deeper sample depth is desired. As one of the main goals of the thesis is to investigate environmental influence over a large range of redshift, we limit the RCS sample to be $M^*_{R_c} + 1.5$ (Chapter 5), and have 60 RCS clusters in total spanning from z=0.20 to z=0.60 (51 in total if the depth is chosen to be $M^*_{R_c} + 2$). With the $M^*_{R_c} + 1.5$ sample depth, we re-compute the group richness N_{gal} using linked galaxies brighter than $M^*_{R_c} + 1.5$, and expressed as η_{grp}. The mock tests show a $\sim 10\%$ false

detection rate at $\eta_{grp} \geq 8.87$ and 4% of the groups containing members from multiple mock groups.

6.3 Group Richness

Galaxy groups are sites where galaxies aggregate. Galaxy groups of larger number of members have deeper gravitational potential. Therefore, to investigate the influence caused by galaxy groups, the group richness should be considered.

The group richness can be indicated by the number of galaxies linked in a group. We use η_{gz} to denote the total number of galaxies linked together into a group, and use η_{grp} to express the net total member count in a group after correcting for the estimated contaminating fore- and background galaxies.

In Chapter 3 we also presented the B_{gc} parameter to indicate the net excess galaxy counts within a given aperture. The B_{gc} of the RCS clusters is computed using a $0.50\mathrm{Mpc}h_{50}^{-1}$ radius. Considering that galaxy groups are poorer systems compared with galaxy clusters, we choose a radius of $0.25\ \mathrm{Mpc}h_{50}^{-1}$ to compute the B_{gc} of each galaxy group. We find that the B_{gc} computed using a radius of 0.5Mpc are $\sim 65\%$ of that calculated using a 0.25Mpc radius, indicating a steeper slope of the galaxy correlation function than the canonical $\gamma = 1.8$.

It is interesting to examine whether a correlation exists between η_{grp} and B_{gc}. In Fig. 4.3 of Chapter 4 we have presented such a comparison for the CNOC1 main groups. We overplot the B_{gc} values of the selected RCS groups ($\eta_{grp} \geq 8.87$) in the same figure and present in Fig. 6.1. The CNOC1 clusters, whose pFOF group richness has been re-calculated using galaxies brighter than $M^*_{R_c} + 1.5$, are plotted as solid circles with error bars in both η_{grp} and B_{gc}. The dashed and dotted curves are the fitting results using the CNOC1 clusters only. The values of the RCS groups are overlaid as dots, and those associated with the RCS clusters (see next section) are plotted as crosses. In Fig. 6.1 the RCS groups and clusters populate a lower η_{grp} and B_{gc} region compared with the CNOC1 clusters, reflecting that the RCS groups and clusters are less massive and dynamically younger than the massive and well virialized CNOC1 clusters.

6.4 RCS Cluster Main Groups

Our interest lies in galaxy properties in different environments including galaxy clusters. Generally speaking, galaxy clusters can be considered as rich galaxy groups. As our

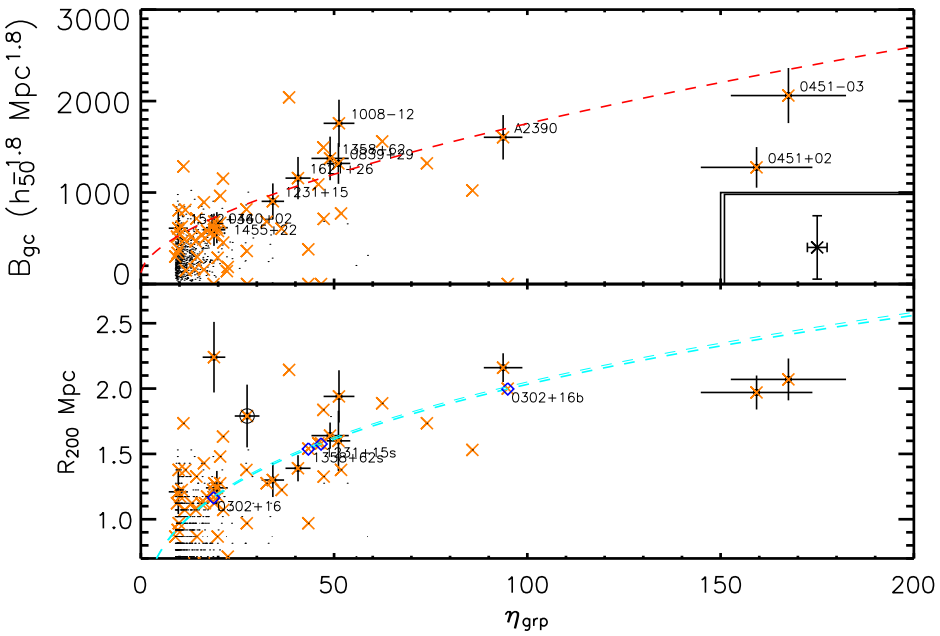

Figure 6.1: *Top:* The relation between group B_{gc} and η_{grp} with CNOC1 clusters overlaid as solid dots with error bars in B_{gc} and η_{grp}. The RCS groups are plotted as dots, and the cluster main groups ($B_{gc,rs} \geq 600$) are shown as crosses. The dashed curves are the power-law fitting results using the CNOC1 clusters only. The typical error bars in B_{gc} and η_{grp} for the RCS groups is shown in the inserted box. *Bottom:* The relation between η_{grp} and virial radii R_{200} with the same meanings of symbols in the *Top* panel. The dashed curve is the power-law fitting result using the CNOC1 clusters only.

sample is from the RCS follow-up observations, we adopt the cluster catalogs identified using the red-sequence cluster finding method by Gladders & Yee (2005). We select clusters from the catalogs of $B_{gc,rs} \geq 400$, $\Delta B_{gc,rs}/B_{gc,rs} < 1$, $\sigma_{rs} \geq 3.3$, and $0.2 \leq z < z_{cut,CL}$. The $z_{cut,CL}$ is the redshift limit determined in each pointing based on the redshift that the sample is to the depth of $M^*_{R_c} + 1.5$. We have 123 clusters of $B_{gc,rs} \geq 400$ in total in our sample. We match our galaxy groups to the RCS clusters and treat the matched galaxy groups as the main cluster galaxy aggregations. A successfully matched pFOF group should span the RCS cluster center. If there are more than one pFOF groups spanning the same RCS cluster center, we define the matched pFOF group as the closest group to the RCS cluster redshift.

We show the comparison between the photometric redshift of the RCS clusters and those of the matched pFOF groups in Fig. 6.2. All the RCS clusters of $B_{gc,rs} \geq 400$ are

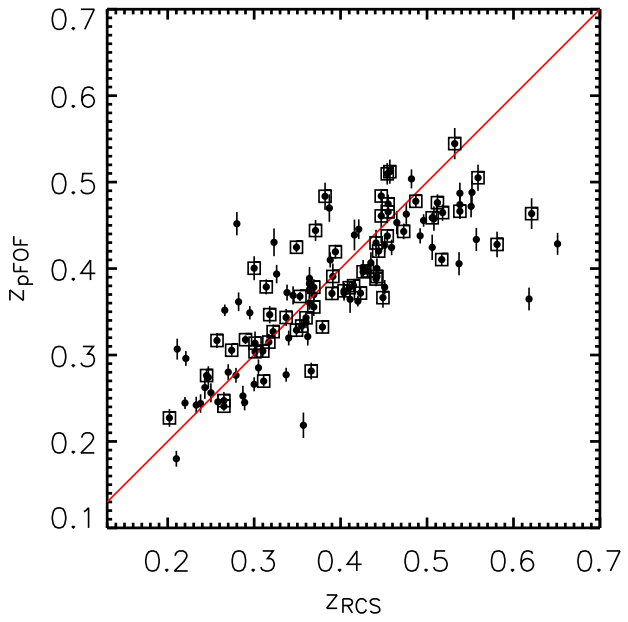

Figure 6.2: The comparison for the RCS cluster main groups ($B_{gc,rs} \geq 400$) in redshift estimated from the red-sequence method and the pFOF algorithm. The open squares mark the clusters of $B_{gc,rs} \geq 600$. The r.m.s. dispersion is ~ 0.054 and ~ 0.049 for the cluster main groups of $B_{gc,rs} \geq 400$ and $B_{gc,rs} \geq 600$.

presented (123 in total), and those of $B_{gc,rs} \geq 600$ (60 in total) are marked by squares. The overall r.m.s. dispersion between the RCS and pFOF redshift are $\sim$0.054 and $\sim$ 0.049 for the RCS clusters of $B_{gc,rs} \geq 400$ and $B_{gc,rs} \geq 600$, respectively. This r.m.s. dispersion is expected, because both the redshift uncertainties relative to spectroscopic redshift in the RCS cluster and pFOF groups are ~ 0.04. In practice, we choose those of $B_{gc,rs} \geq 600$ from the RCS cluster sample as the true 'clusters' in our scientific analyses. This $B_{gc,rs} = 600$ cutoff ($\sim 1.4 \times 10^{14} M_{\odot}$) is about halfway between the Abell richness classes 0 and 1.

To investigate cluster environmental influence, we identify galaxies and groups in the same redshift space as the clusters using an idea similar to the group finding procedure. Since we have matched the clusters and the pFOF groups, we assign the group redshift probability density as the cluster redshift space. These pFOF groups, as the main galaxy aggregations of the RCS clusters, are referred to as the 'cluster main groups'. The 'cluster galaxies' or 'cluster groups' are therefore defined as galaxies or groups having their P_{ratio} to the cluster redshift probability densities satisfying the $P_{ratio,crit}$ criterion.

6.5 General Properties of Galaxy Groups

The RCS clusters are defined using the red-sequence feature in galaxy colors, while the pFOF groups are identified based on galaxy spatial distributions using photometric redshift. As the red sequence is the final destination to where galaxies move on a color-magnitude diagram, it is interesting to compare the properties between general galaxy groups and the cluster main groups. In this section we probe general properties of galaxy groups, and compare with those of the cluster main groups wherever applicable.

6.5.1 The Group Sample

We select our group sample as the pFOF groups of $\eta_{grp} \geq 8.87$. For such a richness cutoff, the tests using the mock catalogs indicate that $\sim 10\%$ of these groups may be false detections. We have 1157 galaxy groups in total in the sample. We present the redshift distribution of our group sample in Fig. 6.3. To control the time axis, the groups are divided into three redshift bins: $0.20 \leq z < 0.35$, $0.35 \leq z < 0.45$, and $0.45 \leq z < 0.60$. We use $z \sim 0.30$, $z \sim 0.40$, and $z \sim 0.50$ to designate these three redshift divisions in the discussion. There are 256, 476, and 425 groups in each redshift bin. We also present their richness distribution in Fig. 6.4, where the distribution of the cluster main groups are over plotted as the hatched histograms enlarged by a factor of 10. The median B_{gc} value of the group sample is ~ 250 in all the three redshift bins. The median B_{gc} for the cluster main groups is ~ 540, larger than that of the group sample by a factor of ~ 2.

As presented in Fig. 4.7 in Chapter 4, the f_{red} calculated using the members in the cluster main groups tend to have larger values than those using the cluster galaxies within $1R_{200}$. Considering that the pFOF algorithm may identify only the main galaxy aggregations within the halo ($< r_{pFOF} > \sim 0.56R_{200}$, where r_{pFOF} is the radius of the circular area equivalent to the group area), we compare the f_{red} of each galaxy group computed using the linked galaxies and using all galaxies in the group redshift space but within $1R_{200}$. We use $f_{red}(G_{linked})$ and $f_{red}(< 1R_{200})$ to denote the f_{red} calculated in these two ways, respectively. We find a correlation between $f_{red}(G_{linked})$ and $f_{red}(< 1R_{200})$, with $f_{red}(< 1R_{200})$ being $\sim 74\%$ of the $f_{red}(G_{linked})$. Therefore, if the f_{red} of galaxy groups correlate with any environmental parameter, the trend should be similar using either $f_{red}(G_{linked})$ or $f_{red}(< 1R_{200})$. We choose $f_{red}(G_{linked})$ to conduct the scientific analyses. We discuss discrepancies in using $f_{red}(G_{linked})$ and $f_{red}(< 1R_{200})$ where relevant.

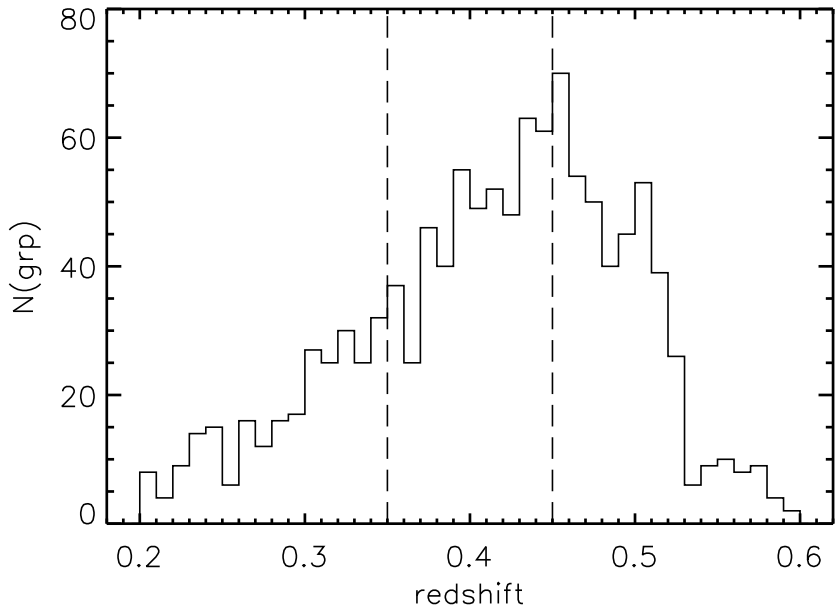

Figure 6.3: The redshift distribution of the group sample using a 0.01 bin size. The vertical dashed lines are the divisions of the redshift subsamples. We have 256, 476, and 425 galaxy groups in each redshift bin. Note that the number of groups drops at $z \geq 0.45$. This is due to the different z_{cut} in different RCS pointings.

6.5.2 Dependence of f_{red} On Group Richness

Hierarchically, a halo grows in mass through merging a few smaller ones. Assuming that galaxy groups rich in their member counts tend to be associated with more massive haloes, we may expect to observe different properties among galaxy groups of various richnesses. In § 6.3 we have adopted the B_{gc} parameter to quantify group richness. To probe this issue of group richness (or, equivalently, halo mass), we investigate f_{red} for galaxy groups at different redshifts and for varying richnesses, and present the results in Fig. 6.5 and Fig. 6.6. Each cross in Fig. 6.5 represents a galaxy group, and the symbol size decreases toward high redshift. The cluster main groups are marked by open diamonds. For each redshift bin, the averaged f_{red} for the galaxy groups (with the cluster main groups excluded) as a function of B_{gc} is presented as the solid ($z \sim 0.30$), dotted ($z \sim 0.40$), and dashed ($z \sim 0.50$) curves. The error bars of the averaged f_{red} is estimated via the bootstrapping method for 100 realizations. Although the mean f_{red} at $z \sim 0.50$ is not a strong function on B_{gc}, the mean f_{red} of groups increases toward larger B_{gc} at $z \sim 0.30$ and $z \sim 0.40$. Fig. 6.6 is the complementary plot of Fig. 6.5,

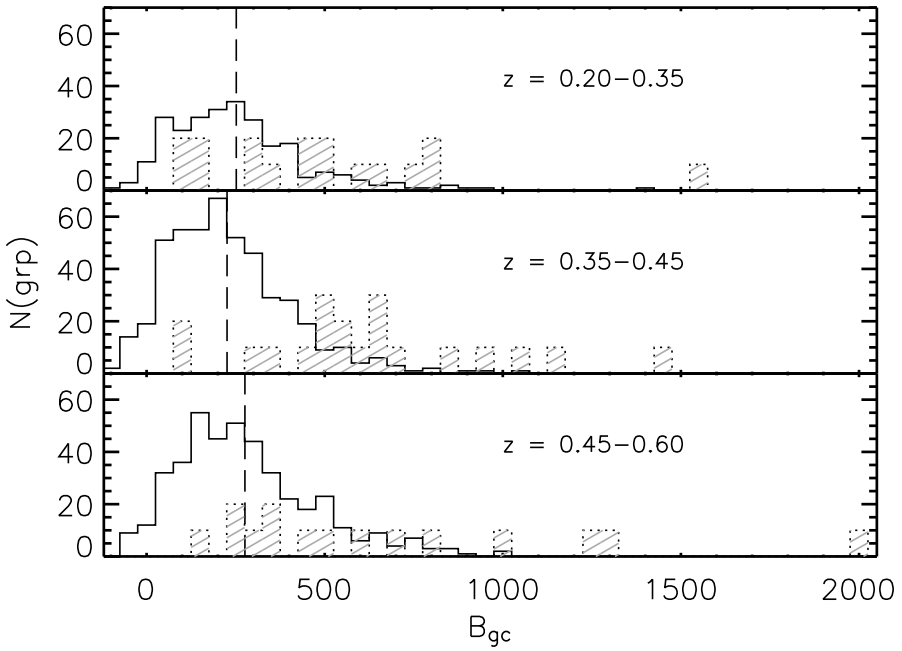

Figure 6.4: The B_{gc} distributions of the group sample using a bin size of 50 $Mpc^{1.8}h_{50}^{-1.8}$. The vertical dashed lines are the median B_{gc} values in each redshift bin. The distributions of the cluster main groups are enlarged by a factor of 10 and presented as the hatched histograms.

plotting the f_{red} as a function of redshift for galaxy groups of similar B_{gc} values. Groups of all B_{gc} richness have similar f_{red} at $z \sim 0.50$. At lower redshift, groups of high B_{gc} have their f_{red} increased by a larger amount than the poor ones, shown by the different slopes of the f_{red}-z trends in Fig. 6.6. The richest groups have their f_{red} increased by $\Delta f_{red} = 0.49$ from $z \sim 0.50$ to $z \sim 0.30$, while $\Delta f_{red} = 0.23$ for the poor groups over the same redshift intervals. These results (larger separation among different curves at the larger B_{gc} regime in Fig. 6.5 and the steeper f_{red}-z trend for the larger B_{gc} bin in Fig. 6.6) show that galaxy groups of high richness evolve faster than groups of low richness, indicating a down-sizing evolutionary scenario on the scale of galaxy groups. We refer to this down-sizing effect as 'group down-sizing', hereafter, to distinguish it from the 'galaxy down-sizing' that star formation takes place and also stops earlier in massive galaxies then shifts to less massive systems at later times.

Over-plotted as open squares in Fig. 6.6 is the f_{red}-z trend for the cluster main groups, which exhibits the largest f_{red} values. Note that we do not separate cluster main groups by their B_{gc} in Fig. 6.6, because the majority of them are of relatively large B_{gc}

compared with galaxy groups. The mean B_{gc} of the cluster main groups is larger than that of galaxy groups by a factor of ~ 2(Fig. 6.4). The cluster main groups possess larger f_{red} than the richest galaxy groups, especially at high redshift. Such differences in the f_{red} values between the cluster main groups and the richest galaxy groups either indicate that galaxy clusters possess some additional mechanisms in driving galaxies therein to evolve faster than galaxies in groups, or simply result from their different formation time, as a down-sizing scenario on the scale from galaxy clusters to groups. We note that the RCS clusters are selected using the red-sequence technique. This may lead to a selection bias against blue structures, and hence larger f_{red} in the cluster main groups. Moreover, there are about 10% of groups which are expected to be falsely detected, and the false detected groups tend to contain small f_{red}. Therefore, part of the large differences in f_{red} between the cluster main groups and the pFOF groups at $z \sim 0.50$ may be due to the combined results of the RCS selection effect together with the false detections in the pFOF groups.

6.5.3 Dependence of f_{red} On Group-Centric distances

Galaxy groups and clusters are formed when haloes merge. As a consequence of the hierarchical evolution, massive galaxies are expected to be located at the centers of their groups or clusters, with satellite galaxies in smaller haloes being accreted to the centers. Therefore, properties of galaxies within groups or clusters are expected to depend on their distance from the center. A number of studies have shown that low and non-star forming galaxies are located preferentially toward the center (e.g., Domínguez et al. 2002; Wilman et al. 2005). As presented in Fig. 6.5 and Fig. 6.6, the f_{red} of galaxy groups are affected by group richness. Probing galaxy properties at different group-centric radii within various types of groups may help unveil what possible mechanisms are active in galaxy groups in affecting star formation of galaxies therein. For the purpose of investigating the dependence on group-centric radii, we stack all group galaxies at similar redshifts and of similar group richness. The group-centric radii are scaled based on a dynamical radius of the group so that the investigation is not limited only either to the core of rich groups or outskirts of poor ones. The center of a pFOF group is determined based on the mean position of its members weighted by their luminosity and local galaxy density (see § 4.5.1 in Chapter 4). We scale the projected distance to the center by the virial radius R_{200} (the radius within which the density is 200 times the critical density). The R_{200} of each group is estimated from the correlation between cluster richness B_{gc} and R_{200} (Yee & Ellingson

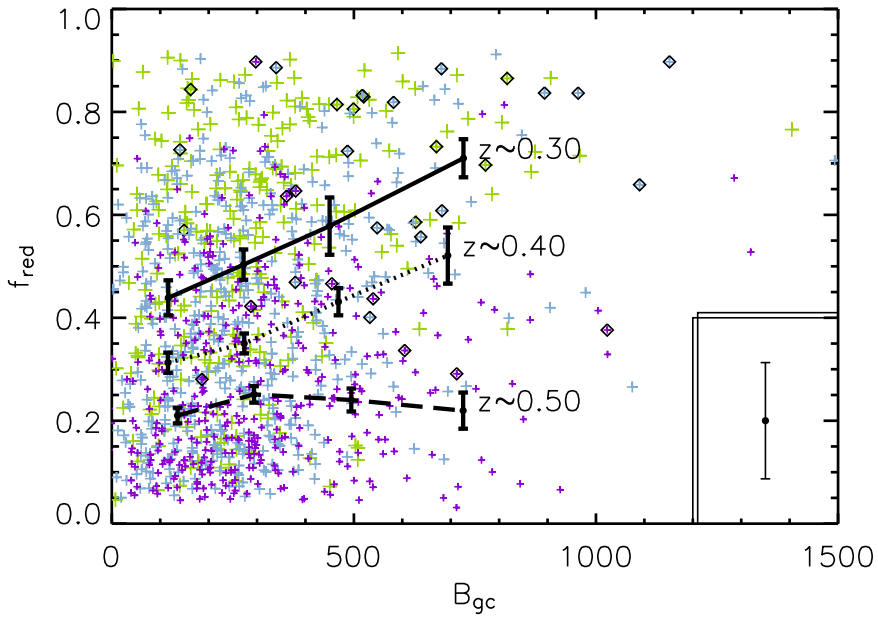

Figure 6.5: The f_{red} of each galaxy group as a function of group richness B_{gc}. Each cross presents a galaxy group with smaller symbol size for groups at higher redshift. The cluster main groups are marked by open diamonds. The solid, dotted, and dashed curves are the average f_{red} for galaxy groups, with the cluster main groups excluded, at $0.20 \leq z < 0.35$, $0.35 \leq z < 0.45$, and $0.45 \leq z < 0.60$, respectively. The uncertainties in the averaged f_{red} are estimated using a bootstrapping method. The typical uncertainties of individual f_{red} measurements is shown in the inserted box. The f_{red} is a weak function of B_{gc} at $z \sim 0.50$ but galaxy groups of larger B_{gc} possess larger f_{red} at $z \sim 0.30$.

2003). We present the estimated R_{200} for the RCS groups as a function of group richness η_{grp} in Fig. 6.1 as well. We use r_{grp} to denote the group-centric radii in units of R_{200}. In the following subsections, we present the radial dependence of f_{red} of the group sample with different parameters controlled.

Rich and Poor Galaxy Groups

To quantify the color trend as a function of group-centric radius, we compute f_{red} at each r_{grp} for rich and poor groups at three redshift bins and present the results in Fig. 6.7. The rich and poor groups are separated at $B_{gc} = 300$. The f_{red} as a function of r_{grp} for galaxies in the cluster main groups are presented in Fig. 6.7 as well. Galaxies in these three subsamples (cluster, rich, and poor groups) at all redshift bins exhibit declining

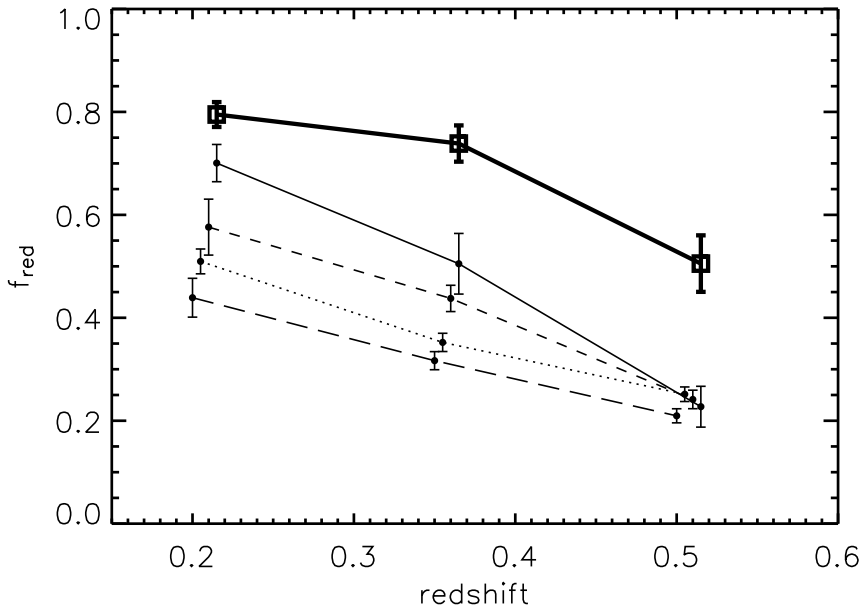

Figure 6.6: The average f_{red} as a function of group redshift, where the uncertainties in the averaged f_{red} are estimated using the bootstrapping method. The long dashed, dotted, short dashed, and solid curves are for galaxy groups of $0 \leq B_{gc} < 200$, $200 \leq B_{gc} < 400$, $400 \leq B_{gc} < 600$, and $600 \leq B_{gc} < 3000$, respectively. The f_{red}-z trend for the cluster main groups is plotted as thick solid curve with open squares. Galaxy groups of higher richness have steeper f_{red}-z trend, indicating that rich galaxy groups evolve more quickly then the poor ones.

trends with increasing r_{grp}. Galaxies in the cluster main groups have the largest f_{red} compared with the rich and poor groups. At $z \sim 0.50$, differences in f_{red} among group subsamples are primarily observed within $r_{grp} < 0.15$. From $z \sim 0.50$ to $z \sim 0.40$, the cluster main groups have their f_{red} increase significantly (by a factor of ~ 1.4) at all r_{grp}, but the changes in f_{red} for both the rich and poor groups occur mainly at $r_{grp} < 0.3$. At $z \sim 0.30$, the central regions up to $r_{grp} \sim 0.5$ of the cluster main groups are largely occupied by red populations with f_{red} approaching 1.0. At the same redshift, the f_{red} within $0.15 r_{grp}$ in the rich groups is as large as that in the core of the cluster main groups. The poor groups, however, still have small f_{red} in their core, but the f_{red} values at all r_{grp} are larger compared with the values at higher redshift. In other words, the differentiation between galaxy groups of different richness starts in the group central regions. That is, the cores of rich groups becomes redder at earlier time than the cores of poor groups.

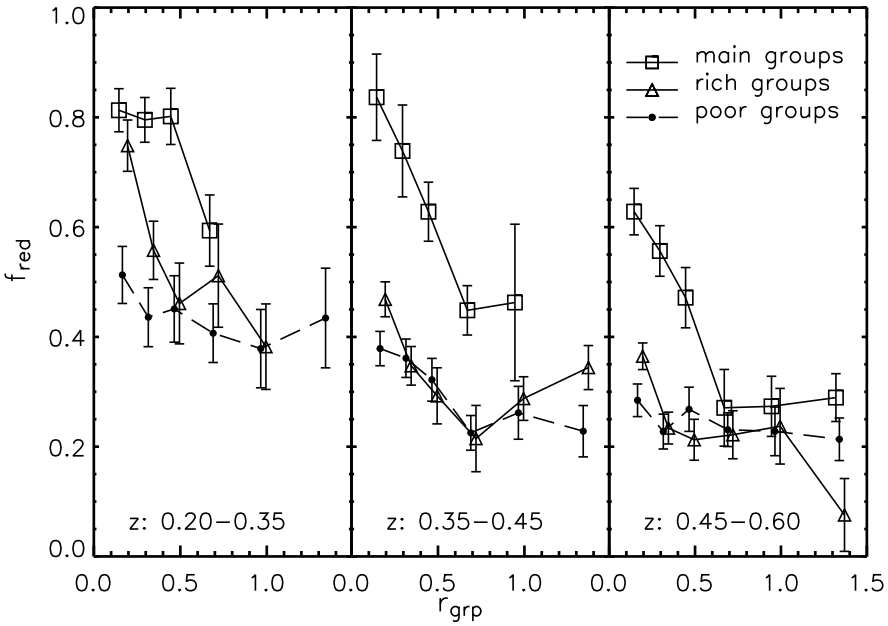

Figure 6.7: The f_{red} as a function of r_{grp} at a fixed redshift for the cluster main groups (open squares), rich (open triangle with solid curves) and poor (solid circles connected with dashed curves) groups. The differences among these three subsamples depend on redshift, and the changes in f_{red} start from group cores.

.

Luminosity of Group Galaxies

To probe how galaxy luminosity affects f_{red} within galaxy groups, we plot the f_{red}-r_{grp} trend by controlling the luminosity of group galaxies. The division of galaxy luminosity in $M^{k,e}_{R_c}$ is set at $M^*_{R_c} + 0.7$. We combine the subsamples of rich and poor groups for the purpose of better signal, but still exclude the subsample of the cluster main groups. The results are presented in Fig. 6.8. Bright group galaxies ($M^{k,e}_{R_c} < M^*_{R_c} + 0.7$) have their f_{red} increased from ~ 0.35 at $z \sim 0.50$ to ~ 0.50 at $z \sim 0.30$ on average. Moreover, the f_{red} for bright group galaxies at a fixed redshift decreases from the group center up to $r_{grp} \sim 0.5$ then remains similar at $r_{grp} > 0.5$. The declining f_{red}-r_{grp} trend is more apparent at $z \sim 0.30$ than that at $z \sim 0.50$. In contrast, group galaxies of faint luminosity have similar f_{red} ($f_{red} \sim 0.15$) at $z \sim 0.40$ and $z \sim 0.50$, and the f_{red} is not a strong function of r_{grp} at these two redshift bins. At $z \sim 0.30$, however, the faint group galaxies have their f_{red} increasing toward smaller r_{grp}, and the values of the f_{red} also become larger than those at higher redshift.

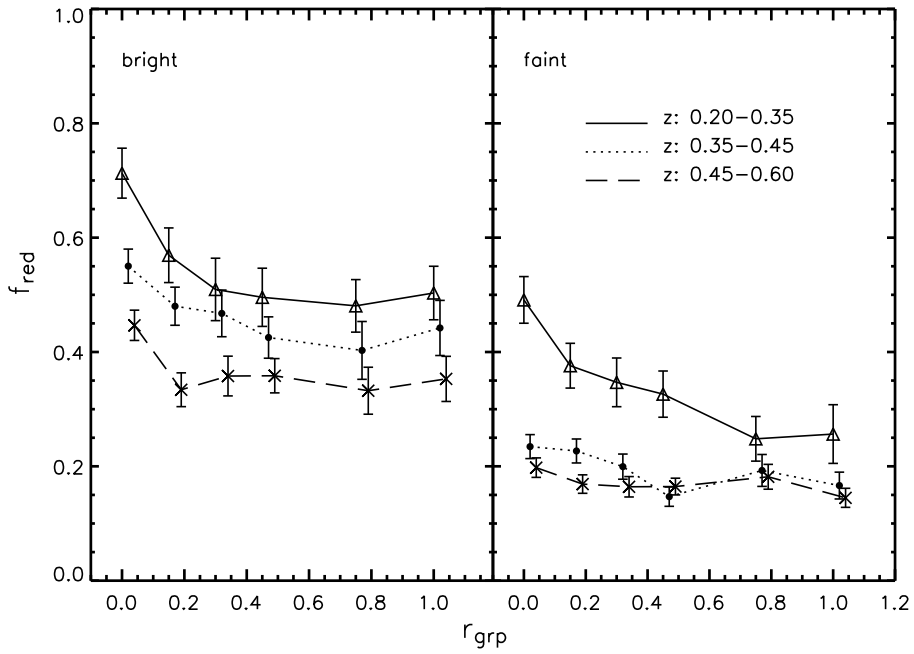

Figure 6.8: The f_{red} as a function of r_{grp} for bright and faint group galaxies of $M_{R_c}^{k,e}$ separated at $M_{R_c}^{*}+0.7$. The solid, dotted, and dashed curves represent $z \sim 0.30$, $z \sim 0.40$, and $z \sim 0.50$ redshift bin, respectively. The bright group galaxies exhibit smoothly declining f_{red} toward larger r_{grp} at all redshifts, and their f_{red} at all three redshift intervals are distinguishable.

Fig. 6.9 re-plots Fig. 6.8 showing the f_{red}-r_{grp} trends for the group galaxies of these two luminosity divisions at each redshift bin. The bright group galaxies have larger f_{red} than the faint subsample at each redshift bin. Furthermore, the most apparent changes across these three redshift bins are the largely increases in f_{red} in group cores. At $z \sim 0.50$, the differences in f_{red} between $r_{grp} \sim 1$ and group cores are ~ 0.10 and ~ 0.04 for the bright and faint group galaxies. At $z \sim 0.30$, however, the differences become as ~ 0.21 and ~ 0.24. The larger f_{red} toward group centers indicate that the star formation activities in group galaxies are quenched by the group environment. A possible quenching mechanism is the formation of AGN in the central galaxy of a sufficiently massive halo. The gradients between f_{red} and r_{grp} are larger at $z \sim 0.30$, further suggesting that the group environmental influence is more effective at lower redshift.

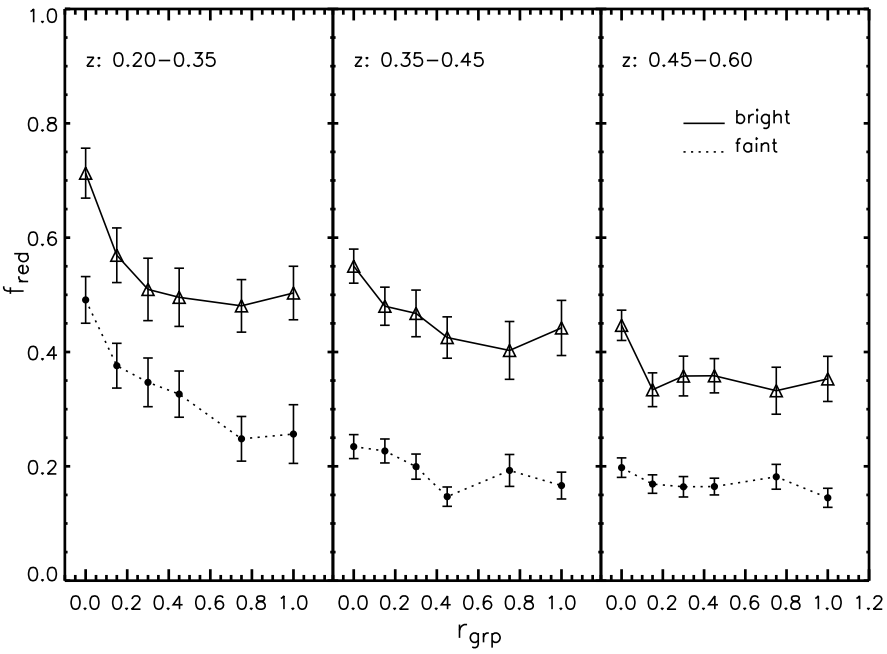

Figure 6.9: The f_{red} as a function of r_{grp} for group galaxies at a fixed redshift but of different luminosities. The solid and dotted curves represent the *bright* and *faint* subsamples. The bright group members have larger f_{red} than the faint galaxies in each redshift bin.

Local Galaxy Density of Group Galaxies

Galaxy groups are believed to be the sites where the transformation from star-forming galaxies to passive ones takes place (see § 1.3 in Chapter 1), because of their relative high galaxy density compared with the field. To probe the role of local projected galaxy density in galaxy groups, we compute Σ_5 (defined in §3.2 in Chapter 3) for each group member using galaxies in the same redshift space as the group, and corrected for background galaxy contamination. The Σ_5, as expected, increases toward group center. This is because infalling field galaxies continuously move toward the group center, and such accumulation of galaxies results in higher local galaxy density in group central regions. We accordingly control Σ_5 of group galaxies at each redshift bin and probe their f_{red} as a function of r_{grp}, and present the results in Fig. 6.10 for the combined subsamples of rich and poor groups. Interestingly, the differences in f_{red} due to different Σ_5 at each redshift bin are mainly observed at larger r_{grp}, and f_{red} is not a strong function of Σ_5 within $0.5r_{grp}$. At $z \sim 0.30$, Σ_5 has no observable effect on f_{red} even at the outer regions of the groups. In other words, the impact of local projected galaxy density, Σ_5, is mainly

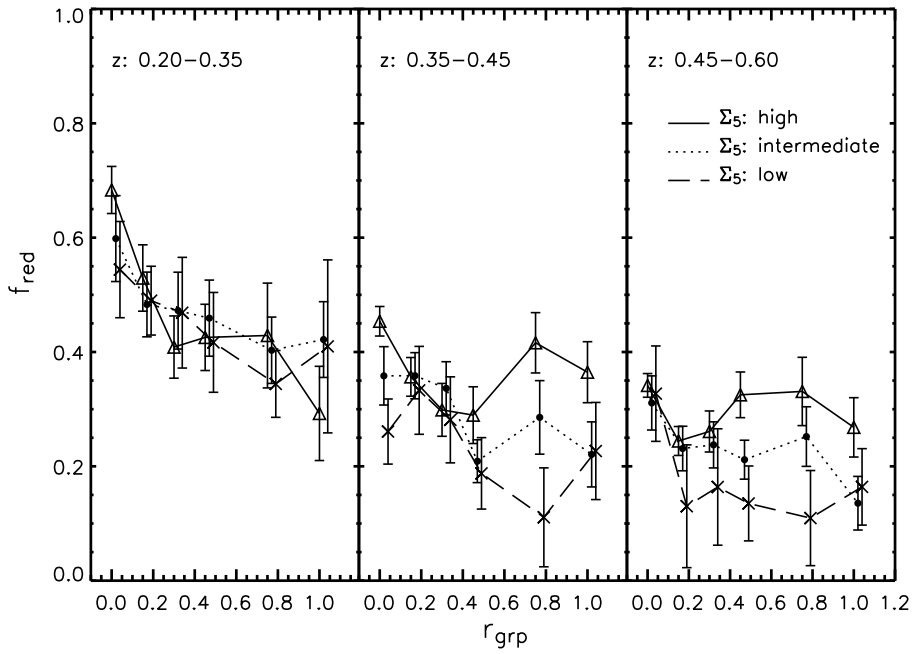

Figure 6.10: The f_{red} as a function of r_{grp} for group galaxies of different Σ_5 at a fixed redshift. The solid, dotted, and dashed curves represent the *high*, *intermediate* , and *low* Σ_5 bins, respectively. All three curves become indistinguishable toward the group center, indicating that the f_{red} is not a strong function of Σ_5 at small r_{grp}.

effective at large r_{grp} but not within group central regions. In Chapter 4 we found that group cluster galaxies have weak dependence on the local projected galaxy density for the CNOC1 sample. Although here we probe the properties of galaxy groups in general, the result of Fig. 6.10 supports the conclusion from the CNOC sample.

6.6 Infalling Galaxy Groups

Within the ΛCDM framework, galaxy clusters are expected to be continuously accreting new galaxies and groups from the outskirts. In § 6.5 we have observed that galaxy properties strongly depend on their group environment. Fujita (2004) suggested that infalling galaxy groups may have quenched their star formation before the whole system enters a galaxy cluster, a process referred to as 'pre-processing' within galaxy groups. As the global cluster environment has an impact on individual infalling galaxies (§ 5.5 in Chapter 5), we may expect such cluster environmental influence also works on galaxy groups. The results of Fig. 4.12 in Chapter 4 indicate that galaxies within galaxy groups

may still maintain their own properties even when the whole group is located within $1.5R_{200}$. Owing to the small size of the CNOC1 sample, we are interested in expanding the investigations of §4.7.3, and probing whether galaxy groups exhibit any correlation between their properties and the projected distances from the cluster center.

We study the properties of infalling galaxy groups from two approaches. The first one, used in the CNOC1 sample, is from the perspective of individual cluster galaxies by flagging them based on their group membership. The other one is to treat individual cluster groups, the galaxy groups in the same redshift space as the clusters, as whole systems and probe their properties at different cluster-centric radii.

6.6.1 Group and Non-Group Cluster Galaxies

For the first approach, we start with identifying the pFOF group membership for each cluster galaxy. Only the pFOF groups of $\eta_{grp} \geq 8.87$ are considered in the sample. However, with the use of photometric redshift, a cluster galaxy may belong to a pFOF group but the group redshift does not coincide with the cluster redshift, because the group redshift is confined by its members and has a more accurate estimation. We therefore define a group cluster galaxy as a cluster galaxy in a pFOF galaxy group with at least three of its members being classified as cluster galaxies. In other words, if there are at least three cluster galaxies within the same pFOF group, these cluster galaxies are flagged as 'group galaxies' even though their hosting pFOF group is not within the cluster redshift. We also define a 'non-group cluster galaxy' subsample as the cluster galaxies within the pFOF groups of $\eta_{grp} < 3$. The gap in η_{grp} is to reduce the ambiguity between group and non-group membership. Those cluster galaxies residing in the cluster main groups are flagged as the 'main-group cluster galaxies', and are excluded from the 'group cluster galaxies' subsample. Limiting up to 10 R_{200}, we have 20476, 109529, and 1592 galaxies in the categories of the group, non-group, and main-group cluster galaxies, respectively.

We conduct the analyses in a similar manner as § 4.7.3 in Chapter 4 and § 5.5 in Chapter 5. With the aim to explore the properties of cluster galaxies in various environments, we investigate f_{red} as a function of only one environmental variable each time with the others controlled. The cluster galaxies are split into two luminosity divisions: *bright:* $M^{k,e}_{R_c} < M^*_{R_c} + 0.7$ and *faint:* $M^*_{R_c} + 0.7 \leq M^{k,e}_{R_c} < M^*_{R_c} + 1.5$. To obtain a better signal-to-noise ratio, we also use the coarser r_{CL} bins as $0 \leq r_{CL} < 1.5$, $1.5 \leq r_{CL} < 4.0$, and $4.0 \leq r_{CL} < 7.0$. Note that the $0 \leq r_{CL} < 1.5$ and $1.5 \leq r_{CL} < 4.0$ bins correspond to

the *inner* and *outer* r_{CL} divisions in § 4.7.3 for the CNOC1 sample. The cluster galaxies are binned into the same three redshift intervals as § 5.5 as $0.20 \leq z < 0.35$ ($z \sim 0.30$), $0.35 \leq z < 0.45$ ($z \sim 0.40$), and $0.45 \leq z < 0.60$ ($z \sim 0.50$). The Σ_5 are divided into *low*, *intermediate*, and *high* regimes based on equal numbers of cluster galaxies in each Σ_5 bin at each cluster redshift interval.

As an example to illustrate the spatial locations of the group and non-group subsamples and their Σ_5 environment, we present a sky map of the cluster galaxies in Fig. 6.11 of the cluster RCS092835+3747.5 at $z_{pFOF} = 0.241 \pm 0.005$. The contours are based on the values of Σ_5 with the levels of one-third and two-third the total galaxy counts. The main-group cluster galaxies of the cluster are plotted as solid circles. The group cluster galaxies in the same pFOF groups are presented with the same symbol, with different symbols representing different pFOF groups. The non-group cluster galaxies are shown as open circles with the symbol size increasing toward high local galaxy density regions. Most of the group cluster galaxies populate the high Σ_5 regions. We shall clarify the characters for both group and non-group galaxies in a certain density region. The non-group cluster galaxies observed in high Σ_5 regions are most likely to be compact and poor galaxy aggregations, but they are not rich enough either to satisfy our selection in group richness or to be found by the pFOF algorithm (a minimum of five linked galaxies is required to be a pFOF group). Comparatively, group cluster galaxies observed in low Σ_5 regions are likely located in the 'suburbs' away from the group centers.

The f_{red} as a function of redshift in a fixed environment for the bright group and non-group subsamples are presented in Fig. 6.12, and those of faint luminosity are shown in Fig. 6.13. The group and non-group cluster galaxies are plotted as the solid and dashed curves, and main-group cluster galaxies are shown as the squares wherever their values are available. Note that Fig. 6.12 and Fig. 6.13 are similar to Fig. 4.11 in Chapter 4, but using the larger size RCS sample with galaxy luminosity controlled. For a fixed environment in Fig. 6.12 and Fig. 6.13, both the group and non-group galaxies possess smaller f_{red} at $z \sim 0.50$, but the group subsample has larger f_{red} than the non-group subclass at $z \sim 0.30$. The f_{red}-z trend in a fixed environment is steeper for the group galaxies than that of the non-group subsample. The steeper f_{red}-z trend exhibited by the group subsample relative to non-group subclass means that galaxy evolution is faster within galaxy groups, indicating some additional mechanisms active in galaxy groups to accelerate the galaxy evolution. The evolutionary stage of the galaxies in the galaxy groups, however, is still more advanced than those not associated with any galaxy groups or cluster main groups (i.e., the non-group galaxies).

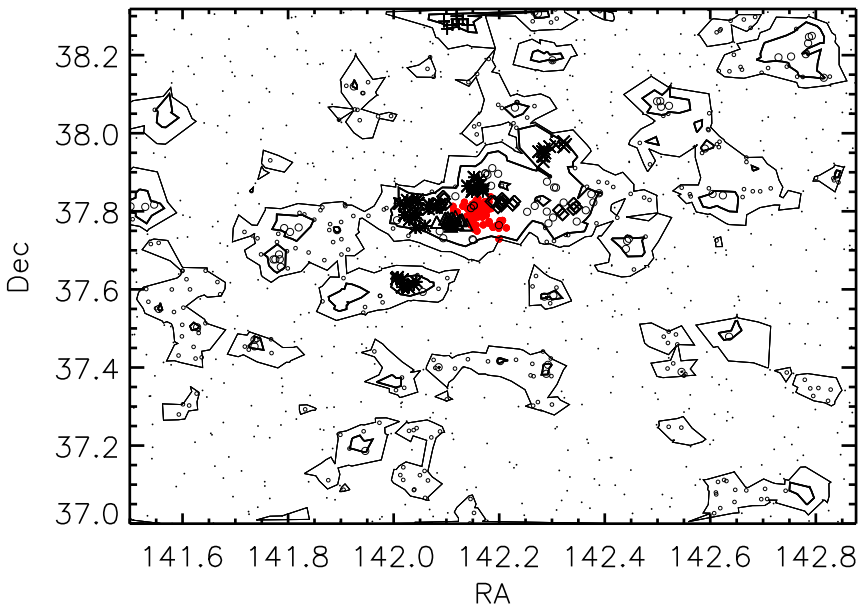

Figure 6.11: The sky map of RCS092835+3747.5 ($z_{pFOF} = 0.241 \pm 0.005$). The cluster galaxies in each pFOF group are plotted with the same symbol, while different symbols represent different pFOF groups. Those in the cluster main group are plotted as the solid circles. The dots and open circles represent the non-group cluster galaxies with symbol size increasing toward high Σ_5 regions. The contours are based on Σ_5 of the one-third and two-third cluster galaxy numbers. The group cluster galaxies populate in high Σ_5 regions. The non-group cluster galaxies in high Σ_5 locations are most likely to be compact or poor groups.

The fact that galaxy groups possess larger f_{red} is usually referred to as 'pre-processing'. However, galaxies in groups are of relatively larger galaxy density than that of the field. Therefore any difference in galaxy properties between group and field may be simply caused by the effect of local galaxy density. To differentiate the effects related to galaxy groups and local galaxy density, we re-plot Fig. 6.12 and Fig. 6.13 with both local galaxy density and redshift controlled in each panel. We present the results in Fig. 6.14 and Fig. 6.15. Instead of being limited to three r_{CL} divisions, we adopt a running-bin method in r_{CL}, where the r_{CL} shifts by 1.0 interval every step with a bin size of $\Delta r_{CL} = 2$. Note that the divisions in Σ_5 are the same for the group and non-group subsamples for direct comparison. In regions of high galaxy density, both bright and faint galaxies in groups exhibit larger f_{red} than that of the non-group galaxies at $z \sim 0.30$ and $z \sim 0.40$,

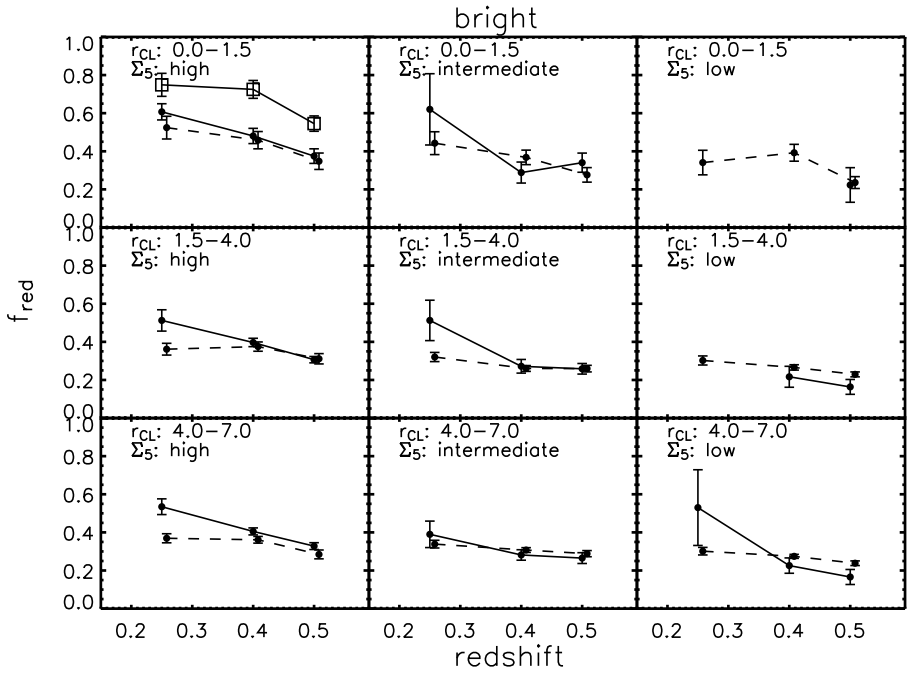

Figure 6.12: The f_{red}-z trends for the bright group (solid) and bright non-group (dashed) cluster galaxies in a fixed environment, where the main-group cluster galaxies are overlaid as the open squares. The group and non-group subsamples have similar f_{red} at $z \sim 0.50$ but the group subsample possesses larger f_{red} at $z \sim 0.25$.

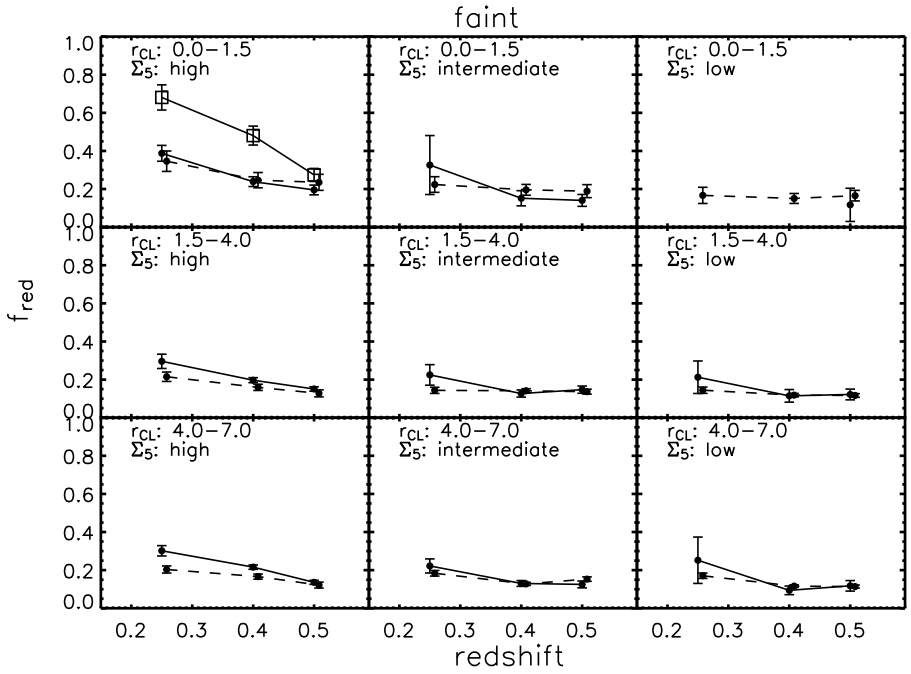

Figure 6.13: Same as Fig. 6.12 but for the faint ($M^*_{R_c} + 0.7 \leq M^{k,e}_{R_c} < M^*_{R_c} + 1.5$) subsamples.

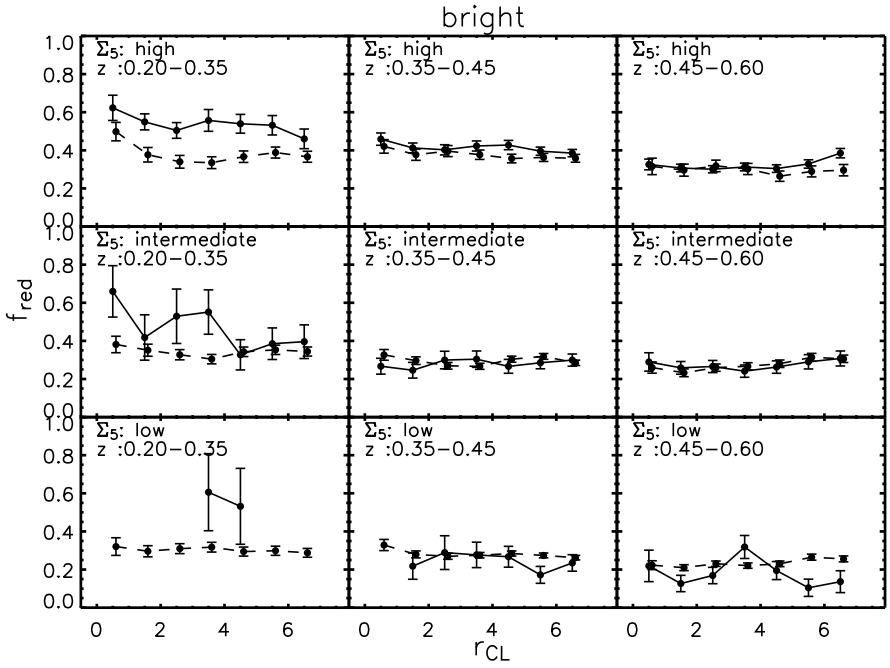

Figure 6.14: The f_{red} as a function of r_{CL} with Σ_5 controlled at a fixed redshift for the bright group (solid) and non-group (dashed) subsamples. The group and non-group subsamples exhibit weak dependence of f_{red} on r_{CL} and have their f_{red} differentiated at low redshift and in regions of high Σ_5.

although the group and non-group galaxies possess similar f_{red} values at $z \sim 0.50$. With the local galaxy density controlled, we still observe the differentiated f_{red}-z trends between the group and non-group galaxies. This result implies that the group membership plays a more important role than Σ_5. In intermediate and low galaxy density regions, the differences in f_{red} between the group and non-group galaxies are observed primarily at $z \sim 0.30$ but not at $z \sim 0.40$ or $z \sim 0.50$. Assuming that the regions of high Σ_5 are likely cores of galaxy groups, these results suggest that the cores of galaxy groups produce the largest influence on the galaxy population.

Fig. 6.14 and Fig. 6.15, moreover, show other interesting results. We note that the differences in f_{red} between the group and non-group galaxies do not have a strong dependence on r_{CL} for all Σ_5 and redshift divisions. In other words, it is the group environment that differentiates the f_{red} from the non-group galaxies (i.e., pre-processing), with or without effects from galaxy clusters.

In § 4.7.3 in Chapter 4 we found that the dependence in f_{red} on Σ_5 becomes weaker after flagging the cluster galaxies by their group membership. To investigate the local

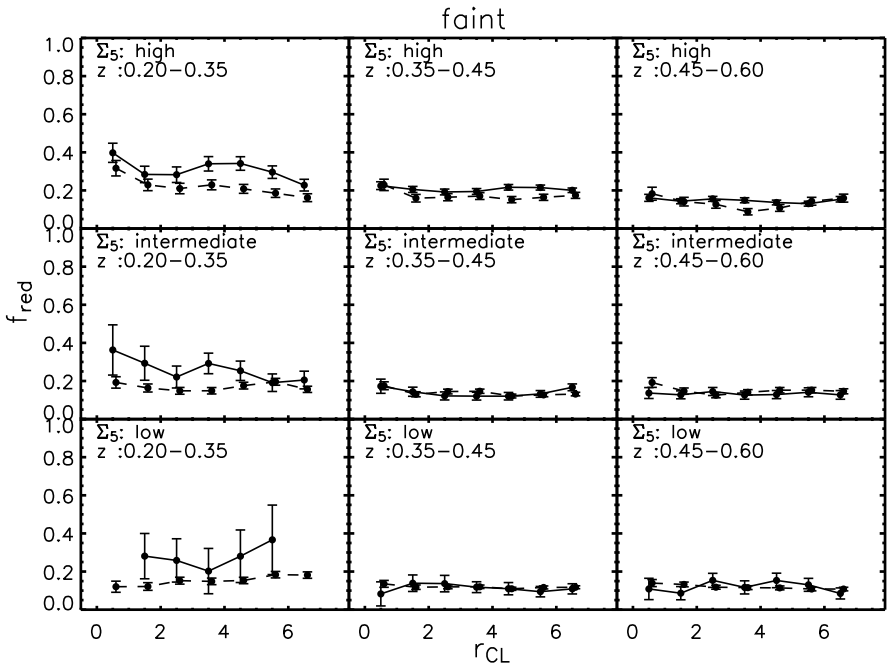

Figure 6.15: Same as Fig. 6.14 but for the faint ($M^*_{R_c} + 0.7 \leq M^{k,e}_{R_c} < M^*_{R_c} + 1.5$) subsamples.

environmental effect on the group and non-group cluster galaxies in the RCS sample, we explore the f_{red} as a function of Σ_5 ('f_{red}-Σ_5' trend) at a fixed r_{CL} and present the results in Fig. 6.16 where we merge the bright and faint subsamples for better signals. Generally speaking, the f_{red}-Σ_5 trends in Fig. 6.16 are still weak for the group (solid curves with triangles) and non-group (dashed curves with crosses) subsamples. The weak dependences on Σ_5 for the group and non-group subsamples in Fig. 6.16 reflect that the group membership of the cluster galaxies plays a more important role than Σ_5. The f_{red}-Σ_5 trends in Fig. 5.7, where the group and non-group subsamples are mixed together, can be considered as the trends of f_{red} as a function of group membership.

6.6.2 Individual Cluster groups

We have observed a weak dependence of f_{red} on r_{CL} using the subsamples of the group and non-group cluster galaxies in Fig. 6.14 and Fig. 6.15. The weak dependence of f_{red} on r_{CL} of the group subsample indicates that the effect of group environment on galaxy properties is not a strong function of how far away they are from galaxy clusters. Another approach to investigate the cluster environmental influence on galaxy groups is to probe the f_{red}-r_{CL} trends from the perspective of individual galaxy groups in the same redshift

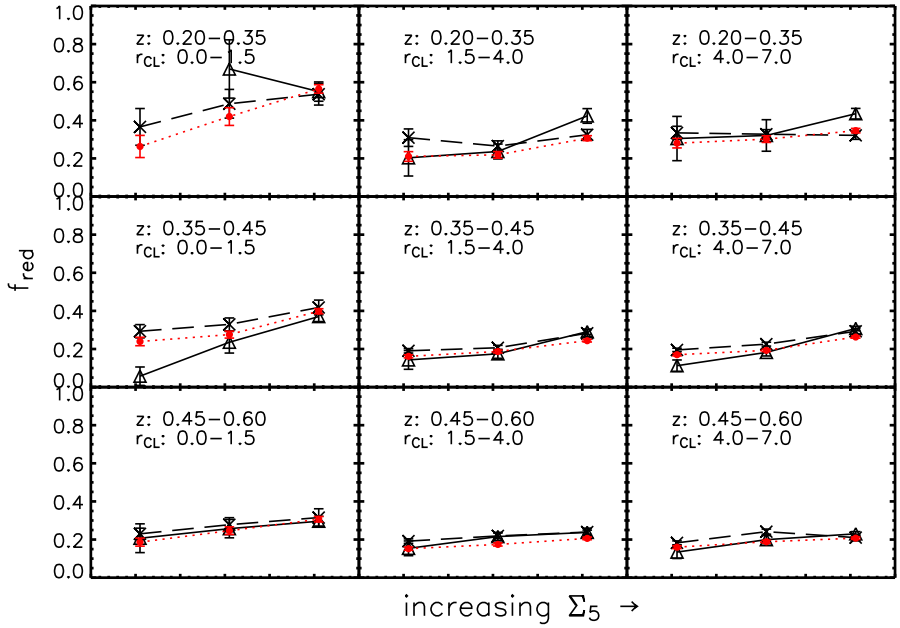

Figure 6.16: The f_{red}-Σ_5 trends for the group (solid curves with triangles) and non-group (dashed curves with crosses) RCS cluster galaxies at fixed r_{CL} and redshift. The results of using the sample of all cluster galaxies are shown as the dotted curves with solid circles. Bright and faint galaxies are combined for a better signal. The f_{red}-Σ_5 trends are weak for the group and non-group subsamples.

space as clusters.

Fig. 6.17 plots the average f_{red} for the cluster groups at each redshift using four bins as $0.0 < r_{CL} < 1.5$, $1.5 \leq r_{CL} < 4.0$, $4.0 \leq r_{CL} < 7.0$, and $7.0 \leq r_{CL} < 10$. The solid, dotted, and dashed curves represent the $z \sim 0.30$, $z \sim 0.40$, and $z \sim 0.50$ redshift bins, respectively. The averaged f_{red} in the cluster main groups at each redshift are plotted as the open square, triangle, solid circle. Cluster groups within $r_{CL} < 1.5$ may possess larger f_{red} compared with the values at the cluster outskirts. However, the differences in f_{red} for group at different r_{CL} may be significant at $z \sim 0.30$ but not at $z \sim 0.40$ or $z \sim 0.50$. In other words, the cluster environment has impact on infalling galaxy groups within $r_{CL} < 1.5$ and the influence is more apparent at low redshift.

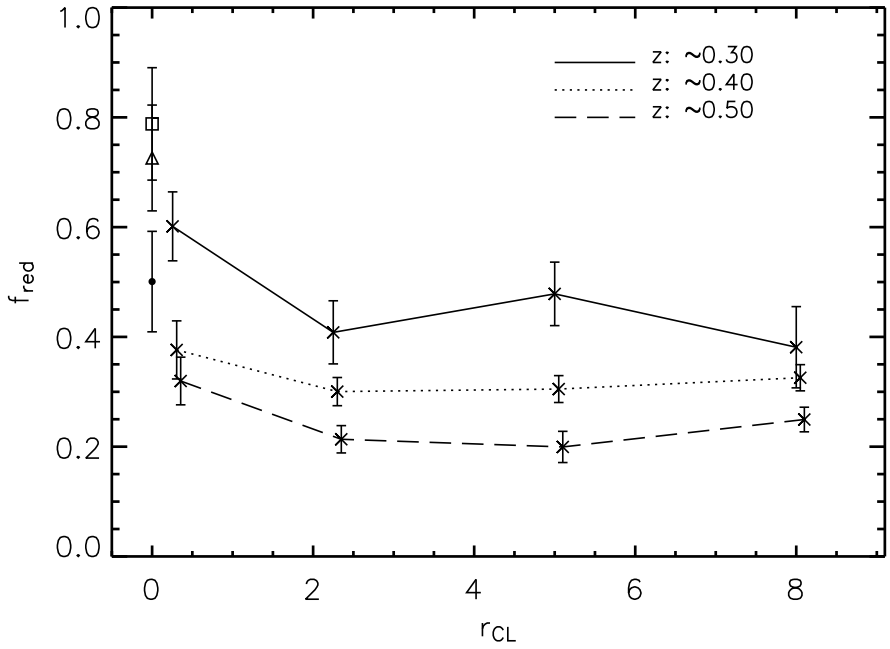

Figure 6.17: The averaged f_{red} as a function of r_{CL} for individual cluster groups at $z \sim 0.30$ (solid), $z \sim 0.40$ (dotted), and $z \sim 0.50$ (dashed). The values in the cluster main groups at each redshift are plotted as the open square, triangle, and solid circles. Galaxy groups at $r_{CL} < 1.5$ may have larger f_{red} compared with those at the outskirts, but the differences are more apparent at $z \sim 0.30$.

6.7 Discussion

It has been known for decades that galaxy properties correlate with their environments: galaxies in galaxy clusters are dominated by a red population, and field galaxies are characterized by a blue population. The morphology-density relation presented in Dressler (1980) has set the stage for many studies in the following decades to quantify this relationship better and to investigate the causes. With the halo model of galaxies and groups, Weinmann et al. (2006, hereafter W06) present that the morphology-density relation can be expressed in terms of halo mass instead of galaxy number density, because the projected galaxy number in a halo usually correlates with halo mass. Using a sample drawn from the SDSS, they show that the fraction of late type galaxies decreases and the fraction of early type galaxies increases with larger halo mass.

A standard picture of the halo model is that some galaxies are embedded in their own individual haloes independently, and some reside within a common halo shared with other galaxies in the form of galaxy groups. In the 'nature' evolutionary scenario, properties

of galaxies mainly depend on the formation history of their dark matter haloes. Galaxies within the haloes are continuously and slowly converting cold gas into stars and appear in blue colors with on-going star formation. However, galaxies can experience various interactions with their environments. Once a halo enters within the virial radius of a more massive one, such as when a single-galaxy halo enters a group halo, it is referred to as a satellite halo or sub-halo within the larger halo. As the satellite or sub-halo orbits within the more massive one, its mass is reduced and the diffuse outer parts can be stripped off by tidal effects and interactions with other substructures. Such reduction in the mass of the satellites can be significant compared with their original mass before falling into the larger halo. The core (i.e., central galaxy) of the infalling sub-halo, in contrast, can still survive due to it high density compared with the outer parts of the halo (e.g., Baugh 2006). In addition to the mass loss, the gas reservoir of the infalling galaxy will be deprived and eventually lead to a halt in its star formation when the galaxy depletes its cold gas. Therefore, such 'nurture' processes may also play an important role in setting the final properties of a galaxy. With the RCS sample, we are able to investigate how group environment nurtures galaxy properties therein.

6.7.1 Role of Group Richness

In § 6.5 we have presented that f_{red} is larger for galaxy groups of higher B_{gc} (richness) and these rich galaxy groups evolve faster along the time axis compared with those of low B_{gc}. The result indicates a dependence in f_{red} on group mass, as the 'group down-sizing effect'. The group down-sizing effect implies that galaxies in more massive (common) haloes are more advanced in their evolutionary stages; they are formed earlier and complete their evolution earlier. This mass dependence is in agreement with the literature, although most other works approach from the correlation functions of early- and late-type galaxies to constrain the fractions of galaxy types with various halo mass (e.g., Magliocchetti & Porciani 2003; van den Bosch et al. 2003; Collister & Lahav 2005).

In agreement with previous studies that galaxies in the centers of groups are most likely to be bright, red, and early-type galaxies (e.g., Brough et al. 2006; Jeltema et al. 2006), we observe larger f_{red} toward group centers. By controlling group richness, we find that the cluster main groups already show larger f_{red} than that possessed by the rich and poor groups at $z \sim 0.50$, and they also exhibit more apparent changes at all r_{grp} from $z \sim 0.50$ to $z \sim 0.30$. On the other hand, the differences in f_{red} between the rich and poor groups are primarily observed in the group central regions ($r_{grp} < 0.3$). Both these

two subsamples have stronger evolution in their core ($r_{grp} < 0.3$) with time. In the core regions, the rich galaxy groups have the f_{red} as large as that in the cluster main groups at $z \sim 0.30$. Consequently, the differentiated f_{red}-r_{grp} trends among the cluster, rich and poor groups occurring at different redshift illustrate the group down-sizing scenario, and this group down-sizing starts from the core regions.

6.7.2 Effect of Galaxy Luminosity

We explore the f_{red}-r_{grp} trends by controlling galaxy luminosity. From Fig. 6.9, we observe that bright galaxies possess larger f_{red} at a fixed redshift than that of the fainter galaxies. The time sequences of the different luminosity subsamples support the galaxy down-sizing evolution scenario: bright massive galaxies start their evolution earlier than faint less massive ones. At $r_{grp} \sim 1$ the differences in f_{red} between $z \sim 0.30$ and $z \sim 0.50$ are ~ 0.15 and ~ 0.08 for the bright and faint group galaxies, respectively. However, within group cores, both the bright and faint group galaxies have similar increases in their f_{red} ($\Delta f_{red} \sim 0.27$) over the same redshift intervals. Considering that the faint group members have similar f_{red} at $z \sim 0.40$ and $z \sim 0.50$, the results indicate that group environment has a larger impact on the faint galaxies and accelerates their evolution from $z \sim 0.40$ to $z \sim 0.30$.

We note that W06 find only a weak dependence of the galaxy type fractions with luminosity at a fixed halo mass. This discrepancy in the luminosity dependence may be a time effect, because our sample is at $0.20 \leq z < 0.60$ and W06's sample is at $z \sim 0.05$. Based on Fig. 6.9, we expect that the f_{red} of the faint luminosity subsample becomes larger at z=0 and may be comparable with that of the bright subsample. In other words, properties of group galaxies is not a strong function of their luminosity at z=0, but is at higher redshift. This may simply be a result of the galaxy down-sizing evolution effect. At z=0, many more fainter group galaxies may have already completed their star formation, resulting in a similar population fraction as the bright group galaxies. At higher redshift, the fainter group galaxies are still young, hence their f_{red} are smaller than the bright group members. This down-sizing effect in time is also observed in galaxy bi-modal color distributions in general in the studies done by Balogh et al. (2004) and Yee et al. (2005). The sample used by Balogh et al. (2004) is drawn from the SDSS at $z \sim 0.05$, and Yee et al. (2005) use the field RCS sample of the redshift spanning from 0.2 to 0.6. Instead of identifying group members, both Balogh et al. (2004) and Yee et al. (2005) study the population fractions as a function of local projected galaxy density in different

luminosity divisions. From Fig. 2 of Balogh et al. (2004) the fraction of red galaxies is indistinguishable in the high Σ_5 bin among different luminosity subsamples. Also in Fig. 2 of Yee et al. (2005), the fraction of red galaxies in the high Σ_5 division segregate among different luminosity subsamples despite the large error bars in their population fractions. These high Σ_5 sites are likely the locations of galaxy groups. Therefore, the different conclusions between W06 and our work about the dependence of f_{red} on luminosity of group galaxies is likely the result of the time sequence in galaxy evolution .

6.7.3 Effect of Local Projected Galaxy Density

The literature has shown that most galaxies in high density regions have early-type morphology or are red in color, whereas those in the field are the late-type blue galaxies, known as the morphology-density or color-density relation (e.g., Cassata et al. 2007; Cooper et al. 2007). From Fig. 5.7 we have observed an increasing trend of f_{red} with larger Σ_5 at fixed r_{CL} bins, as an illustration of the local environmental effect. However, in Fig. 6.16 where the r_{CL} and Σ_5 environmental parameters are investigated from the perspectives of group and non-group cluster galaxies, we observe that both group and non-group subsamples exhibit a weaker dependence on Σ_5. The discrepancy in concluding the effect of the local environment parameterized by Σ_5 between Fig. 5.7 and Fig. 6.16 results primarily from using different samples. Fig. 5.7 uses the whole sample of cluster galaxies, while Fig. 6.16 presents the results using the subsamples divided into the cluster-main, group-, and non-group cluster galaxies. Because the sample used in Fig. 5.7 contains galaxies residing in cluster or group aggregations, the high Σ_5 regions are usually the sites where these cluster or group galaxies are. In estimating f_{red} in different Σ_5 regions, these cluster or group galaxies boost the f_{red} in the high Σ_5 division, and hence results in an increasing f_{red}-Σ_5 trend. By flagging these galaxies in the clusters or groups, the study of the f_{red}-Σ_5 trends is therefore a truer investigation of the Σ_5 effect. In other words, without further identifying the membership of cluster or group galaxies, the large f_{red} in high Σ_5 regions is predominantly caused by the environmental influence within galaxy clusters or groups.

The concept of a 'critical density' above which star formation activities are reduced (e.g., Kodama et al. 2001; Gómez et al. 2003) has been used to illustrate the role of local galaxy density. The regions of the critical density likely correspond to substructures or groups. Bundy et al. (2006) find that the local environmental effect is important only when the local galaxy density is significantly greater than the field density. We find that

group membership plays a more important role than local galaxy density in affecting galaxy properties.

In Fig. 6.10 we observe that the group galaxies of different Σ_5 only exhibit differentiated f_{red} at large group-centric radii but not within the group core. The results of Fig. 6.10 imply that the properties of group galaxies are mainly determined by their locations relative to the group centers. As long as galaxies are within a galaxy group, their 'local' environment as measured by local galaxy density is overwhelmed by their group environment of being in a common more massive halo. Note that the Σ_5 divisions in Fig. 6.10 and Fig. 6.16 cannot be compared directly, because the divisions in Fig. 6.16 are determined based on the whole sample of the cluster galaxies at a redshift interval, but only the sample of group galaxies are used in Fig. 6.10.

We note that the changes in the f_{red}-Σ_5 trends between using the whole sample and controlling for group membership are more apparent in the CNOC1 sample (Fig. 4.13) than the RCS sample. This may be due to their different dynamical states. The CNOC1 clusters are X-ray selected and likely more virialized systems than the RCS clusters (The B_{gc} of the CNOC1 clusters is $\sim$ 30% larger than the RCS clusters, on average; Fig. 6.1). In other words, the CNOC1 clusters are sited in more evolved structures. Galaxy groups infalling to the CNOC1 clusters are therefore likely to be in denser and larger-scale structures compared with those infalling to the RCS clusters. Our studies in probing local environmental effects parameterized by Σ_5 reveal the importance of group membership. The commonly accepted color-density relation can be considered as equivalent to a correlation of galaxy color as a function of group membership.

6.7.4 Group Membership of Cluster Galaxies

The differences in galaxy evolution driven by galaxy groups compared with galaxies not in galaxy groups are observed in Fig. 6.12 and Fig. 6.13. Both the group and non-group cluster galaxies exhibit similar f_{red} at $z \sim 0.50$, but the group subsample shows larger f_{red} than the non-group subsample at lower redshift. The results of Fig. 6.12 and Fig. 6.13 also imply that the Butcher-Oemler effect is applicable to galaxy groups. The differentiated f_{red} between the group and non-group subsamples toward lower redshift strongly demonstrates that galaxy groups possess additional mechanisms, such as mergers, AGN feedback, and strangulation, in driving galaxy evolution over that of the field. It is known that galaxies within galaxy groups have properties different from those in the field (e.g., Gerke et al. 2007; Jeltema et al. 2007). One may naturally

argue that the differences between the group and non-group galaxies primarily result from the effect of their local galaxy density. However, since we have compared the differences between these two subsamples in a fixed environment, including controlling Σ_5 and cluster-centric radius, our results hence reveal the importance of group membership. Such more advanced galaxy evolution stage within galaxy groups is generally referred to as the results of pre-processing. This pre-processing term was originally proposed to explain the conflict between the theoretical prediction and the observations about star formation deficit in disk galaxies which directly fall into the main cluster. More precisely, the term pre-processing refers to galaxy groups in the cluster space. However, we observe a very weak dependence of f_{red} on cluster-centric radius (r_{CL}) beyond $\sim 1R_{200}$ using the subsample of the group cluster galaxies in Fig. 6.14 and Fig. 6.15. Since f_{red} is larger in the group subsample compared with the non-group subclass, the very weak dependence of f_{red} on r_{CL} of the group subsample indicates that the star formation within galaxy groups is generally decreased compared with the non-group galaxies no matter how far away they are from a galaxy cluster. In other words, galaxy groups do 'process' galaxies therein with or without the presence of a galaxy cluster. That is, cluster potential does not cause pre-processing. The 'pre-processing' is *just* a 'property' of galaxy groups.

6.8 Conclusion

The RCS sample has allowed us to achieve the goal of investigating galaxy properties within galaxy groups. We have probed the f_{red} within galaxy groups of different richness. We have also explored properties of group galaxies as a function of their group-centric radii with either their luminosity or local projected galaxy density controlled. To study various environmental influences on galaxies, as the main goal of this thesis, we have probed f_{red} in environments associated with galaxy clusters, groups, and local projected galaxy density. We summarize the main results of this chapter as follows.

• Galaxy groups exhibit the Butcher-Oemler effect (Fig. 6.6). A 'group down-sizing effect' is observed on the scale from galaxy clusters to poor groups. Galaxy Groups of high richness have their f_{red} increased faster along the time axis than that exhibited by poor galaxy groups. The f_{red} possessed by galaxy groups, however, are still smaller than that of the clusters at all redshift.

• Galaxies within galaxy groups exhibit a galaxy down-sizing effect on galaxy scale (Fig. 6.8). The bright group members possess larger f_{red} than the faint members. The f_{red} possessed by the bright group members is not a strong function of redshift, but the

faint group galaxies exhibit apparent increases in their f_{red} from $z \sim 0.50$ to $z \sim 0.30$, indicating that they are evolving at a higher rate, whereas bright galaxies have mostly completed their evolution.

• After distinguishing group membership, both group and non-group galaxies exhibit weak dependence on their local projected galaxy density. As long as galaxies are within a galaxy group, the properties of these galaxies are mainly affected by their group environment. The common accepted color-density relation can be interpreted as a relation between color and group membership.

• Galaxy groups process galaxies therein (Fig. 6.14 and Fig. 6.15). Galaxies in groups exhibit larger f_{red} compared with those classified as non-group galaxies after local galaxy density is controlled. The differences in f_{red} between the group and non-group subsamples are primarily observed in group cores. This 'pre-processing' appears to be independent of the cluster environment in which the galaxies reside.

References

Balogh, M. L., Baldry, I. K., Nichol, R., Miller, C., Bower, R., & Glazebrook, K. 2004, ApJ, 615, L101

Baugh, C. M. 2006, Reports of Progress in Physics, 69, 3101

Berlind, A. A. & Weinberg, D. H. 2002, ApJ, 575, 587

Bower, R. G., Benson, A. J., Malbon, R., Helly, J. C., Frenk, C. S., Baugh, C. M., Cole, S., & Lacey, C. G. 2006, MNRAS, 370, 645

Brough, S., Forbes, D. A., Kilborn, V. A., & Couch, W. 2006, MNRAS, 370, 1223

Bundy, K., et al. 2006, ApJ, 651, 120

Cassata, P., et al. 2007, ArXiv Astrophysics e-prints

Collister, A. A. & Lahav, O. 2005, MNRAS, 361, 415

Cooper, M. C., et al. 2007, MNRAS, 224

Cooray, A. & Sheth, R. 2002, Phys. Rep., 372, 1

Croton, D. J., et al. 2006, MNRAS, 365, 11

Domínguez, M. J., Zandivarez, A. A., Martínez, H. J., Merchán, M. E., Muriel, H., & Lambas, D. G. 2002, MNRAS, 335, 825

Dressler, A. 1980, ApJS, 42, 565

Fujita, Y. 2004, PASJ, 56, 29

Gerke, B. F., et al. 2007, MNRAS, 222

Gladders, M. D. & Yee, H. K. C. 2005, ApJS, 157, 1

Gómez, P. L., et al. 2003, ApJ, 584, 210

Jeltema, T. E., Mulchaey, J. S., Lubin, L. M., & Fassnacht, C. D. 2007, ApJ, 658, 865

Jeltema, T. E., Mulchaey, J. S., Lubin, L. M., Rosati, P., & Böhringer, H. 2006, ApJ, 649, 649

Kodama, T., Smail, I., Nakata, F., Okamura, S., & Bower, R. G. 2001, ApJ, 562, L9

Magliocchetti, M. & Porciani, C. 2003, MNRAS, 346, 186

Marinoni, C. & Hudson, M. J. 2002, ApJ, 569, 101

Mo, H. J., Yang, X., van den Bosch, F. C., & Jing, Y. P. 2004, MNRAS, 349, 205

Peacock, J. A. & Smith, R. E. 2000, MNRAS, 318, 1144

Springel et al. 2005, Nature, 435, 629

Tinker, J. L., Weinberg, D. H., Zheng, Z., & Zehavi, I. 2005, ApJ, 631, 41

Vale, A. & Ostriker, J. P. 2004, MNRAS, 353, 189

van den Bosch, F. C., Yang, X., & Mo, H. J. 2003, MNRAS, 340, 771

Weinmann, S. M., van den Bosch, F. C., Yang, X., & Mo, H. J. 2006, MNRAS, 366, 2

Wilman, D. J., Balogh, M. L., Bower, R. G., Mulchaey, J. S., Oemler, A., Carlberg, R. G., Morris, S. L., & Whitaker, R. J. 2005, MNRAS, 358, 71

Yang, X., Mo, H. J., & van den Bosch, F. C. 2003, MNRAS, 339, 1057

Yee, H. K. C. & Ellingson, E. 2003, ApJ, 585, 215

Yee, H. K. C., Hsieh, B. C., Lin, H., & Gladders, M. D. 2005, ApJ, 629, L77

Yee, H. K. C. & López-Cruz, O. 1999, AJ, 117, 1985

Chapter 7

Conclusions

7.1 Summary

Galaxy properties strongly correlate with their environment. The environment includes from the local regime, such as individual galaxies' surrounding density, to the global domain, characterized by the large dark matter haloes of galaxy clusters and groups. Several environmental influences may have effect in a region at the same time. The main goal of this thesis is to investigate which environmental impact is more dominant in places where both local and global environmental influences are effective.

7.1.1 Group Finding Using Photometric Redshift Data

In this thesis we have focused on galaxy photometric properties in various environments using photometric redshift samples. For the purpose of studying environment within galaxy groups, we have developed an algorithm to identify galaxy groups in photometric redshift space in Chapter 2. This algorithm adopts the linking idea of the standard friends-of-friends algorithm, and uses the group redshift as a conditional probability density to determine group membership of the linked galaxies. The innovative characteristic of our group-finding algorithm is the improvement of redshift estimation via the constraints given by the transversely connected galaxies in a group, because all galaxies in the same group should have the same redshift. We have presented a detailed description of the algorithm underlying idea and structures in Chapter 2. The algorithm has been tested by applying it to the Virgo Consortium Millennium Simulation mock catalogs. We have conducted various tests on the pFOF algorithm performances, including the use of different linking criteria and samples of different photometric redshift properties. The

comparisons show excellent performance of our algorithm. The pFOF algorithm is able to recover more than 80% of mock groups of halo mass greater than $1.2 \times 10^{13} M_{\odot}$, and have a 100% recovery rate for mock groups of halo mass at least $3.4 \times 10^{13} M_{\odot}$. The false detection rate is less than 30% for the pFOF groups of at least 6 net members, and drops to 10% when the pFOF groups contains at least 8 net members. We also apply the pFOF algorithm to the real observed CNOC2 sample. The application to the CNOC2 group catalog gives results which are consistent with the mock tests.

7.1.2 Environmental Parameters

Chapter 3 describes the environmental parameters and the computation of population fraction which are used in our studies. With an attempt to study galaxy photometric properties in different environments, we demarcate the environmental effects into the local and global regimes. The local environmental effect is parameterized by the projected galaxy density calculated using the 5^{th}-nearest-neighbor method. The global environmental influence is inspected using the cluster-centric radii in units of the cluster virial radius. We compute the fractions of red galaxies using a statistical inference for a better estimation, because the number of galaxies within a fixed environment or a galaxy group is not large for most cases and the background contamination have an important role in affecting the estimation of the true galaxy fractions. All our computations using photometric redshifts, such local galaxy density, include background contamination corrected.

7.1.3 The CNOC1 Cluster Sample

In Chapter 4 we applied the pFOF algorithm to the CNOC1 sample, which contains 16 clusters at $0.17 < z < 0.55$. We investigate the dependence of red galaxy fractions on environment. The strategy is to study red galaxy fraction as a function of only one environmental variable with others controlled. Within a fixed environment, the red galaxy fraction decreases when redshift increases. This Butcher-Oemler effect is observed within all local projected galaxy density bins and at cluster-centric radii out to ~ 4 virial radii. We have observed that galaxy evolution is quickened by the local environment at a fixed cluster-centric radii. At a similar projected distance to cluster centers, galaxies located in regions of high local projected galaxy density have their red galaxy fractions increasing faster with decreasing redshift, compared to those residing in low projected galaxy density regions. We have also observed that global cluster environment accelerates

galaxy evolution. At a fixed redshift interval, the trend of red galaxy fractions with fixed local projected galaxy density increases faster for galaxies at small cluster-centric radii than those at large radii.

By flagging cluster galaxies into group and non-group subsamples, the group galaxies exhibit larger red galaxy fractions than the non-group galaxies within the environment of similar local galaxy density and at the same cluster-centric radius. Meanwhile, the red galaxy fraction for the group galaxies also decreases toward higher redshift, and the changes are larger compared with non-group galaxies. This implies that the Butcher-Oemler effect is applicable to galaxy groups. We find that the differences among clusters, groups, and non-group galaxies depend on local galaxy density and redshift. At $0.40 \leq z < 0.55$, the group and non-group galaxies have similar fractions of red galaxies, but the clusters are already distinguishable from the galaxy groups. The group galaxies start to have their red galaxy fraction differentiated from that of the non-group galaxies at lower redshift, and at $z < 0.3$ their fractions of red galaxies are similar to that of the clusters. We observe that the cluster environmental influence is relatively stronger on non-group galaxies. For the infalling galaxy groups, we find that galaxies within group cores still maintain their own properties as they fall into the clusters.

7.1.4 The RCS Cluster Sample

Chapter 5 focuses on environmental influence on individual cluster galaxies of different luminosities at $0.20 \leq z < 0.60$ using the RCS sample. The RCS sample, covering $\sim$40 deg^2, provides a much larger sample than the CNOC1 sample and enables the global environmental parameter to extend to larger distances. We note that this is an optically selected cluster sample, as opposed to the X-ray selected CNOC1 clusters. We observe both down-sizing star formation in galaxies and the Butcher-Oemler effect in all environments in the RCS sample. Within a fixed environment, bright galaxies possess larger red galaxy fractions than faint galaxies, illustrating the down-sizing effect in star formation. The gradients between red galaxy fractions and redshift (the Butcher-Oemler effect) are steeper within cluster core than the outskirts, indicating the accelerated evolution driven by cluster environment within the virial radius. At $z \sim 0.50$, bright galaxies show a stronger dependence of red galaxy fractions on local galaxy density than that of faint galaxies. At $z \sim 0.30$, both the bright and faint galaxies exhibit similar dependence in red galaxy fractions on local galaxy density. All the dependences of red galaxy fractions on local galaxy density are relatively shallow beyond the cluster virial radius. The global

cluster environmental influence predominates within ~ 1.5 virial radii.

In Chapter 6 we addressed the role of galaxy groups in the RCS sample. We observe that galaxies within groups of higher richness are faster in their evolutionary speed than those in groups of lower richness, which can be interpreted as 'group down-sizing' evolution. Rich galaxy groups have their red galaxy fractions increased more rapidly compared with the poor groups. We find that the group membership substantially determines galaxy properties. Galaxy groups process galaxies therein, and such processing is independent of their locations relative to the cluster centers. Within a fixed environment where both local galaxy density and cluster-centric radius are controlled, galaxies within groups possess larger red galaxy fractions than individual galaxies not associated with galaxy groups. We also find that both group and non-group galaxies have weak dependence of their red galaxy fractions on local galaxy density. Therefore we conclude that group membership is a dominant factor in determining galaxy evolution, more important than the effects of both local galaxy density and global cluster environment.

7.1.5 Galaxy Evolution and Environment

In summary, our work reveals that the observed properties of galaxy population are the combination of natural galaxy characteristics and nurtured environmental influence. The differentiated red galaxy fractions possessed by galaxies of different luminosities in a fixed environment are related to natural galaxy evolution, and is usually referred to as galaxy down-sizing in star formation. Galaxies of similar luminosity but residing in different environments also exhibit differentiated red galaxy fractions, reflecting the results nurtured by environment. The Butcher-Oemler effect for the bright and faint galaxies is similar in regions of high galaxy density, but star formation is truncated more rapidly in bright galaxies than the faint ones in low galaxy density regions. Both the bright and faint galaxies exhibit weak dependence in red galaxy fractions on local galaxy density beyond cluster core. The cluster influence is effective within ~ 1.5 virial radii. We find that the excess in red galaxy fractions for galaxies in the high galaxy density regions in the cluster core is higher than that for galaxies in low galaxy density regions. This could be an indication that mechanisms such as harassment and tidal interactions are operating in high galaxy density regions in addition to ram-pressure stripping, while ram-pressure stripping is the main mechanism in regions of local galaxy density. For environment of similar local galaxy density and at a fixed cluster-centric radius, galaxies within groups have their star formation truncated rapidly compared with galaxies not

in groups. This fact of larger red galaxy fractions in groups (which is evidence for 'pre-processing') is primarily related to group environment, and is independent from influence of cluster environment. The group influence depends on group richness (mass). Galaxies in groups of high richness (massive haloes) evolve faster than those in poor groups (less massive haloes), which can be interpreted as the 'group down-sizing' effect; fractions of red galaxies within rich galaxy groups increase more rapidly toward lower redshift compared with poor groups. The pre-processing together with group down-sizing illustrate the substantial role of group environment in galaxy evolution.

7.2 Prospective Analyses and Projects

A number of prospective analyses and projects can be conducted and developed based on this thesis. We provide some outlines as follows.

• Dependence of Galaxy Color and Morphology on Group Membership in SDSS

Most studies on the topic of environmental influence on galaxy groups are conducted using the data from the Sloan Digital Sky Survey (SDSS; York et al. 2000). The SDSS has made available large amounts of spectroscopic and photometric data of galaxies at $z \sim 0$. Examples include galaxy bimodal color distributions as functions of their magnitude and local environment (e.g., Balogh et al. 2004; Baldry et al. 2006; Park et al. 2007) and properties of galaxies within galaxy groups (e.g., Mandelbaum et al. 2006; Martínez et al. 2006; Berlind et al. 2006). The most interesting work relevant to this thesis is the concept of critical galaxy density in galaxy colors (Gómez et al. 2003). The local projected galaxy density calculated based on the n^{th}-nearest-neighbor method is the most commonly used proxy for galaxy local environment. In Chapter 5 we observe that individual galaxies have their red galaxy strongly dependent on their local environment especially within cluster central regions. The results of local environmental effect agree with the literature. However, after we separate the galaxies based on their group membership into group and non-group subsamples, both these two subsamples exhibit only weak dependence on local galaxy density. Therefore we conclude that the correlation between galaxy properties and local environment is actually a correlation with group membership. With this argument, we may expect to also discover a weak dependence of galaxy properties on the local projected galaxy density in the SDSS sample after controlling for the group membership of galaxies. This will help us understand better about how galaxy groups affect their member galaxies from $z \sim 0$ to $z \sim 0.6$.

• The RCS-IMACS Spectroscopic Data

The RCS-IMACS observations are the spectroscopic follow-up observations using the images of the RCS-CTIO sample (Chapter 5) using the IMACS spectrograph on the Magellan 6.5m Baade Telescope. Combined with the data in-hand from CFHT MOS, Magellan LDSS3, and Gemini GMOS, about 20,000 spectra sampling well into the cluster infall regions will be available. Added with more spectroscopic redshift into the training set, the photometric redshift measurements will be improved. More important, the spectroscopic redshift will allow us to confirm some of the pFOF group membership, and perhaps provide some dynamical information. Furthermore, although not every galaxy in the identified pFOF groups will have spectroscopic information, the IMACS spectroscopic data are still large enough to allow us to study star formation history both in group and non-group galaxies in more details, using features such as equivalent width of emission or absorption lines.

• RCS Spitzer Follow-up

The RCS core sample has multi-faceted follow-up observations, including optical B and V photometry using CTIO, HST SNAP program, and spectroscopic observations using IMACS on Magellan and GMOS on Gemini. A set of 36 clusters in the RCS core sample has been observed using IRAC $3.6\mu m$ and $4.5\mu m$ channels (program ID#20754). These clusters are selected to be at $z = 0.5 \sim 1.1$ with richness $B_{gc} = 500 \sim 1,500$ (equivalent to Abell richness 0 to 3). The targets have been observed, and can be accessed from collaborators. The data has a depth of $M^* + 2$ at $z \sim 1$ for images observed in $3.6\mu m$. Each cluster has a field-of-view of $\sim 15' \times 15'$, which corresponds to physical scales from 6 to 8 Mpc (about $2 \sim 3R_{200}$) depending on cluster redshift. Fifteen of the RCS-IRAC clusters are chosen from the RCS-CTIO dataset in this thesis. The catalogs of photometric redshift and galaxy groups are already available. The future follow-up observations will target on galaxy groups in the same redshift as the clusters but located beyond the cluster central regions to $4\sim 6R_{200}$. This project will provide rest K-band colors for cluster and group galaxies at high redshift, and allow us to create a stellar-mass limited galaxy sample all the way out to the infall regions.

• The RCS2 Survey

The RCS2 is a imaging survey in $g'r'z'$ for ~1,000 deg^2 with also substantial i' band coverage. With large sky coverage and multi-passband photometry, we can apply the photometric redshift technique (with new training sets) and group-finding algorithm to the RCS2 sample, and conduct the analyses in a similar manner as this thesis. The contents in § 6.5 show interesting results, but the error bars are still substantial. The large-size RCS2 sample will greatly improve the measurements in population fractions for

both group and non-group subsamples. A significant portion of the data has the seeing of $\sim 0.65''$. This good seeing quality will enable us to measure galaxy morphology at low redshift, and hence investigate environmental influence using galaxy morphology in additional to color measurements.

Meanwhile, ~ 400 deg^2 RCS2 field in the Southern sky are being used for the WiggleZ project (Glazebrook et al. 2007). The WiggleZ project is a spectroscopic survey with the goal to achieve the detection of features of Baryonic Acoustic Oscillations at high redshift using emission line galaxies. The survey uses the AAOmega spectrograph at AAT in the wavelength of 3700-8750Å at a resolution of 5Å FWHM. Although the WiggleZ project is not developed specific to study environmental influence, some of the spectroscopic targets will coincide with pFOF groups from the RCS2 sample. This will give us opportunities to do spectroscopic studies in the subject of environmental influence, and to construct future spectroscopic follow-up observations to get more spectra for other members in the same pFOF groups.

Another interesting project related to this thesis is to study the correlation between AGNs and their environment. The identification of AGNs can be achieved using the RCS2 multi-passband photometry in combination with GALEX data (from the WiggleZ project). The fractions of AGNs in different environments within the RCS clusters, pFOF groups, and the field will give insights into the nature and nurture scenarios of galaxy evolution.

References

Baldry, I. K., Balogh, M. L., Bower, R. G., Glazebrook, K., Nichol, R. C., Bamford, S. P., & Budavari, T. 2006, MNRAS, 373, 469

Balogh, M. L., Baldry, I. K., Nichol, R., Miller, C., Bower, R., & Glazebrook, K. 2004, ApJ, 615, L101

Berlind, A. A., Kazin, E., Blanton, M. R., Pueblas, S., Scoccimarro, R., & Hogg, D. W. 2006, ArXiv Astrophysics e-prints

Glazebrook, K., et al. 2007, ArXiv Astrophysics e-prints

Gómez, P. L., et al. 2003, ApJ, 584, 210

Mandelbaum, R., Seljak, U., Cool, R. J., Blanton, M., Hirata, C. M., & Brinkmann, J. 2006, MNRAS, 372, 758

Martínez, H. J., O'Mill, A. L., & Lambas, D. G. 2006, MNRAS, 372, 253

Park, C., Choi, Y.-Y., Vogeley, M. S., Gott, J. R. I., & Blanton, M. R. 2007, ApJ, 658, 898

Springel et al. 2005, Nature, 435, 629

York, D. G., et al. 2000, AJ, 120, 1579